Electronic Properties and Measurement Techniques of 2D Heterostructures

Eric Lester

A dissertation

submitted in partial fulfillment of the

requirements for the degree of

Doctor of Philosophy

University of Washington

2026

Reading Committee:

David H. Cobden, Chair

Matthew Yankowitz

Anton Andreev

Program Authorized to Offer Degree:

Physics

University of Washington

Abstract

Electronic Properties and Measurement Techniques of 2D Heterostructures

Eric Lester

Chair of the Supervisory Committee:

David H. Cobden

Department of Physics

For the last fifty years, two-dimensional (2D) systems have stood out as model platforms for exploring electronic phenomena. Reduced dimensionality, electrostatic tunability, and enhanced electron-electron interactions enable effects not seen in bulk 3D conductors. Following the isolation of graphene, research on van der Waals (vdW) materials has exploded, revealing a vast landscape of correlated and topological physics. The ability to stack dissimilar materials into heterostructures has enabled control of the carrier density and displacement field of 2D samples while also opening the door for less conventional measurements. The limitless combinations and permutations of 2D heterostructures make for a rich and rewarding field of study. This thesis investigates the niche of 2D semimetals, specifically the electronic transport properties of the hybrid semimetal graphene-WTe_2. While graphene hosts massless Dirac fermions that have high mobility and weak intrinsic interactions, WTe_2 is dominated by correlated physics. This includes

a putative excitonic insulator ground state, a likely unconventional superconducting state, and topological phenomena like the quantum spin Hall effect. By combining these complementary materials, we discover details of interlayer coupling in 2D semimetals as well as measurement and analysis techniques for other 2D heterostructures.

I will begin this thesis by presenting historical context for the study of 2D systems, including techniques for the fabrication and measurement of 2D vdW heterostructures. I will then introduce both graphene and WTe_2. Through careful analysis of the transport properties of the resulting hybrid, I will recover parameters of physical interest for both constituent materials. I will also present a sensing technique utilizing a remote graphene sensor to probe the chemical potential of the hybrid, shedding further light on its character. It will be shown that the properties of the hybrid can be largely understood from those of the individual monolayers with modifications due to interlayer tunneling and electron-electron interactions. Next, I will present my studies of the 2D dielectrics hexagonal boron nitride (BN) and Bi_2SeO_5. This work will show a hitherto unreported inverted temperature dependence in the breakdown of BN as well as the potential uses of Bi_2SeO_5 in 2D devices. Finally, I will discuss the problem of sample rotation and how it can be used to further characterize the electronic properties of matter. I will present my work towards the development of an in-situ two-axis rotator for use in a dilution refrigerator, including some preliminary testing results.

TABLE OF CONTENTS

LIST OF FIGURES

ACKNOWLEDGEMENTS

First and foremost, I want to express my sincerest gratitude to my advisor, Prof. David Cobden. My first time speaking with Dave, he politely informed me that I had misspelled his name on my application to the University of Washington. Nevertheless, he graciously offered me a spot in his lab and has been an excellent advisor and mentor ever since. Dave is a remarkable scientist with a zeal for experiment and an undying commitment to honesty and integrity in both his work and interpersonal relationships. He has been extremely supportive, accommodating, and understanding when I have needed it most while still pushing me to be the best researcher and scientist I can be. The care and consideration he puts into his work are readily apparent, though always understated. His offbeat humor and wit are also a joy, and it has been a privilege to be a part of his lab family.

Next, I would like to thank my lab peers for their instruction, hard work, and close friendship in the daily grind of research. This includes senior lab members who graciously spent time and effort to train me in physics theory and the experimental methods of transport. In particular, I want to thank Paul Nguyen and Elliott Runburg for their instruction and friendship over the years. I would also like to thank the next generations of graduate students, particularly Gianluca Delgado, Ruhee Nirodi, and Baker Hase. It's been wonderful working, chatting, teaching, learning, and spending time with them, and I am excited to see what they are able to accomplish. Finally, I would like to give a special thanks to the undergraduate and master's students who I've had the privilege of working with and mentoring over the years. These include Chelsey Erway, Matt Adams, Viru Sharma, Shreya Pekety, Andrew Barkley, Emily Toph, Jarod Scribner, and several others. These friendships have made my graduate school tenure more fulfilling and rewarding than I could have expected.

I would like to give special thanks to Ken Adams and Chun-chih Tseng as well. Ken was the most overqualified master's student I ever met, a guru of hardware and software alike. His ability and desire to work autonomously on the two-axis rotator and data analysis were remarkable and can hardly be understated. Chun-chih was a Ph.D. student in Prof. Matthew Yankowitz's lab whom I worked closely with to study the graphene-WTe_2 system, the main subject of this thesis. He was a kind and insightful collaborator, eager to help in every step of the process. This thesis would not be what it is without them, and I hope that it honors their hard work and contributions.

Of course, I have others to thank outside of the Cobden lab as well. The 2D materials community at UW and my broader cohort are exceptional, full of brilliant minds and kind hearts. Unfortunately, there are too many individuals to list here, so I will instead offer blanket thanks to the patient and tireless crystal growers in Prof. Jiun-Haw Chu's lab and the assiduous and dedicated lab members of Profs. Xiaodong Xu, Matthew Yankowitz, and Arthur Barnard. Their insights, friendship, and commiseration have been a pleasure, and I wish all of them the very best at UW and beyond. Special thanks are due to the members of my committee: Profs. Matthew Yankowitz, Anton Andreev, Boris Blinov, and Juan Carlos Idrobo. I have only good things to say about them, and I am proud to be a UW alum because of them. I would also like to thank the friends I've met along the way including (but in no way limited to) Sam Borden, Ellis Thompson, and Jac Barlow.

Finally, I would like to thank my community outside of UW. This includes teachers who inspired me like Liz Woolard, Henry Rich, and David Ennis; great friends like Myles Jardine and Matthew Dozer; but the most special thanks of all goes to Alexa Lansberry. Alexa moved cross-country with me to Seattle, and the years we spent together were some of the most important and impactful of my life. She was an indispensable source of warmth, joy, and support throughout my program, and I wish her nothing but the absolute best.

DEDICATION

To my grandmother, Alice Lester

Chapter 1. Introduction to 2D Transport

The canonical introductory problem for quantum mechanics concerns a particle in a box. By trapping a particle in space, the Schrödinger equation forces discrete solutions, quantizing the allowed energies of the particle. This problem has remained an important pedagogical tool used to segue into more sophisticated models of the atom. Ultimately, the study of atomically thin systems would lead to the advent of truly two-dimensional (2D) electron systems, realizing this and many other quantum mechanical models. Following the successful mechanical exfoliation of graphene in 2004, 2D materials research has exploded with transport remaining a key characterization method. In this chapter, we will introduce this rich and active field of study.

1.1 Physics in 2D

It may seem reductive to consider a "two-dimensional" system in a three-dimensional world. After all, even a single sheet of atoms has a finite thickness. However, let us quantitatively consider an electron trapped in a very thin sheet that extends 5 μm in both *x* and *y* but only 0.5 nm in *z*. Solving the Schrödinger equation for a particle in a 3D box with dimensions L_x, L_y, and L_z gives the following discrete energy levels: [1]

$$E(n_x, n_y, n_z) = \frac{\pi^2 \hbar^2}{2m}\left(\frac{n_x^2}{L_x^2} + \frac{n_y^2}{L_y^2} + \frac{n_z^2}{L_z^2}\right)$$

The ground state energy for $n_x = n_y = n_z = 1$ is 1.50 eV. Exciting the electron in either *x* or *y* ($n_x = 2, n_y = n_z = 1$) only raises the energy by 45 neV, a 0.000003% increase. However, the first excited state in *z* ($n_x = n_y = 1, n_z = 2$) has an energy of 6.02 eV, four times higher than the ground state energy! Reaching this energy by exciting only in *x* and *y* requires $n_x = n_y = 12{,}248$. In other words, the electron is completely trapped in its ground state in the *z* direction. As such, it

is entirely reasonable to call this system two-dimensional. While this is an exceptionally crude model for an actual solid, real material systems can exhibit truly 2D physics as we will now see.

1.1.1 *The 2D Electron Gas and Strongly Correlated Systems*

Some of the earliest 2D systems were studied in the late 1970s via the physisorption (weakly perturbing physical adsorption) of gases onto flat substrates like cleaved graphite. Adsorption isotherms showed regions of saturation punctuated by abrupt steps, from which it was inferred that gas molecules were forming sheets on the substrate one atomic layer at a time. [2]

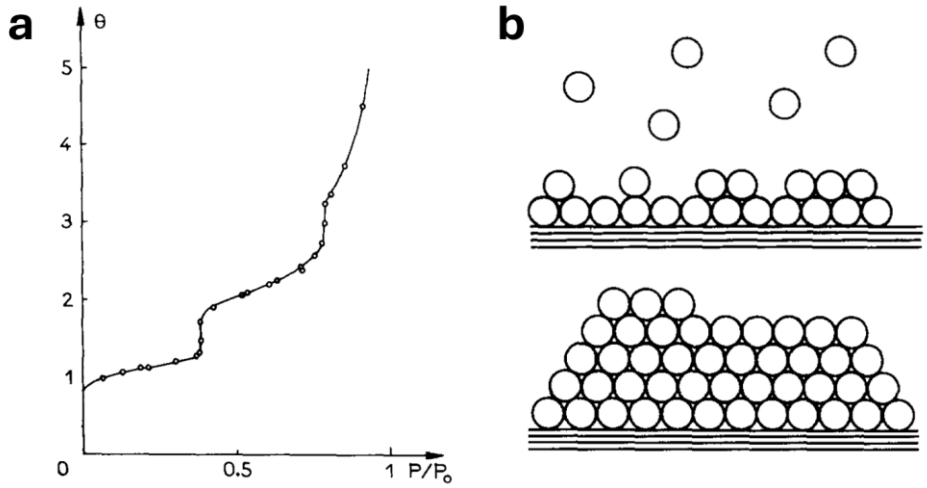

Figure 1.1: Reproduced sections of Figs. 7 and 10 from [3] showing physisorption isotherms of krypton on graphite at $T = 77$ K. (a) Surface coverage θ is plotted vs. pressure. (b) Layers of gas molecules forming sheets, transitioning from a 3D gas to a 2D condensed phase.

Concurrently, developments in microelectronics would go on to produce another 2D system: the 2D electron gas (2DEG). The metal-oxide-semiconductor field effect transistor (MOSFET) revolutionized technology as the core element at the heart of every microprocessor, and it is also an early realization of a 2D electron system. As the name implies, a MOSFET contains a stack of a metal, oxide, and semiconductor with the metal functioning as a "gate." By applying a voltage to it, the gate generates a displacement field that penetrates the insulating oxide, bending the bands

of the semiconductor in order to satisfy the electrostatic boundary conditions at the oxide-semiconductor interface. A full treatment of band theory is outside the scope of this thesis, but it is worth emphasizing the core principle: in a periodic lattice, discrete atomic energy levels broaden into continuous energy bands. Gaps between bands represent forbidden states, with partially filled bands being conducting and fully filled bands being insulating. The energy of the highest occupied state is dubbed the Fermi energy, equivalent to the chemical potential in the zero temperature limit. In a MOSFET, the electrostatic energy from the gate bends the bands of the semiconductor, forming an inversion layer. If the inversion is sufficiently strong, the conduction band of the semiconductor may dip below the Fermi energy, partially filling the conduction band and creating a conductive 2DEG at the oxide-semiconductor interface. [4]

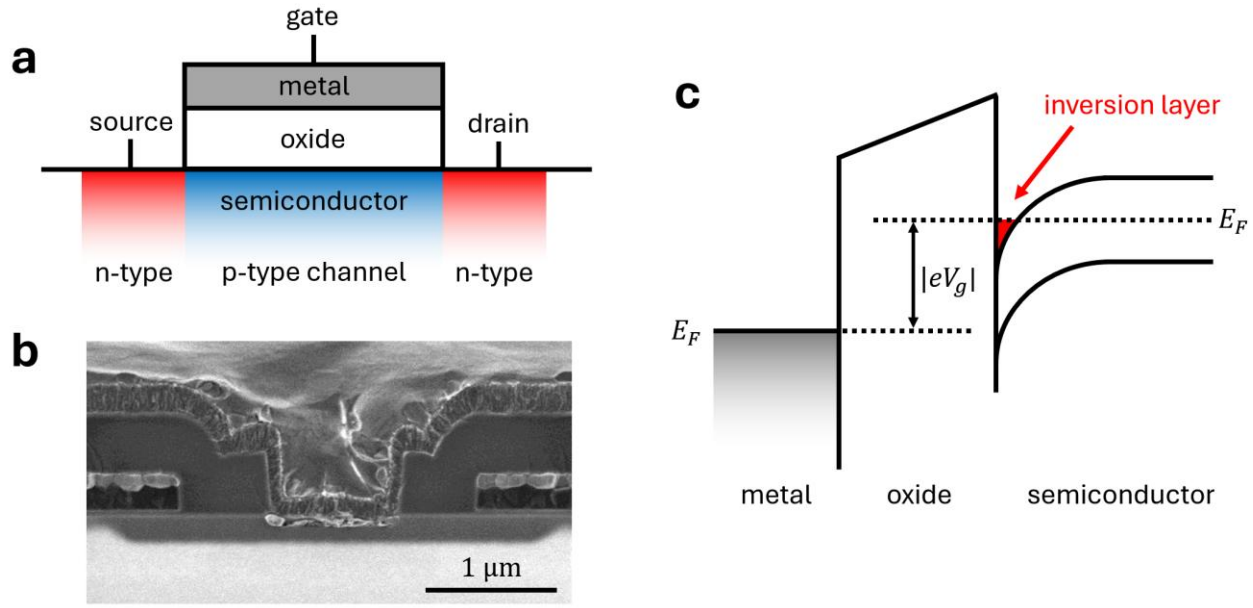

Figure 1.2: The MOSFET and band inversion. (a) Side view schematic of a MOSFET. When a gate voltage V_g is applied, band bending forms a narrow inversion layer at the oxide-semiconductor interface allowing current to flow from source to drain. (b) Scanning electron microscopy (SEM) image of a 4H-SiC MOSFET with a channel width of 0.5 µm, reproduced from [5]. (c) Band alignment diagram (electron energy vs. position) showing band bending and the formation of a 2DEG in the inversion layer.

Other layered heterostructures can also host 2DEGs, the most studied being GaAs quantum wells. Using molecular beam epitaxy (MBE), it is possible to grow atomically flat layers of the narrow bandgap semiconductor GaAs between thicker regions of a wider bandgap semiconductor like $Al_xGa_{1-x}As$. Electrons become trapped in the potential well of the GaAs layer, resembling the thin sheet example that introduced this chapter. After decades of refinement, epitaxial quantum wells became the gold standard for clean, high-mobility, strongly confined 2DEGs. [6]

This realization of the 2DEG led to a proliferation of experimental tests of earlier theoretical predictions. Electrostatic screening is weaker in 2D than 3D (the 2D density of states is independent of energy, so screening does not increase with carrier density like it does in 3D [4]), allowing for greater tunability of the 2DEG than is possible in 3D conductors. Additionally, interactions between carriers are substantially more impactful in 2D than 3D, i.e. the ratio of interaction energy to kinetic energy is larger for 2D systems. [4] The 2DEG made strongly correlated electron systems more accessible than ever before. For example, in 1934, Wigner predicted that if interactions sufficiently dominated kinetic energy, electrons would form "close-packed lattice configurations," [7] a state later known as a Wigner crystal. By applying a strong magnetic field to a 2DEG, kinetic energy is quenched as electrons fill Landau levels—quantized energy levels of 2D charges undergoing cyclotron motion from an out of plane magnetic field. The resulting Wigner crystal ground state was first realized in GaAs quantum wells. [8] Landau levels themselves were first posited in 1930. [9] Fifty years later, von Klitzing would demonstrate the integer quantum Hall effect in a MOSFET 2DEG, [10] an achievement that would win the 1985 Nobel prize. GaAs 2DEGs would then realize the fractional quantum Hall effect in 1987, [11] dramatically kickstarting topological [12] and composite fermion theories, [13] winning the 1998 Nobel prize and solidifying the 2DEG as the key platform for strongly correlated physics.

1.1.2 *Van der Waals Materials*

Until now, we have focused on 2D electron systems created at interfaces between solid and gas, oxide and semiconductor, or narrow and wide bandgap semiconductors. However, naturally occurring materials which possess a 2D crystal structure exist and are called layered or van der Waals (vdW) materials. These materials form crystalline planar layers which are held together out of plane only by the vdW force. [14][15] This simple fact has dramatic, far-reaching consequences. Consider graphite, the best known vdW material. In graphite, carbon sheets are held together in plane by sp^2 bonds, but these sheets are coupled to each other by the much weaker vdW force. As a result, it is remarkably easy to separate these layers, making graphite soft with high lubricity. It is even possible to isolate an individual sheet of carbon atoms through mechanical exfoliation (repeatedly peeling the crystal apart), a single-atom thick monolayer known as graphene. [16] Compare this to another carbon allotrope, diamond, in which each carbon atom forms sp^3 bonds with its neighbors creating a distinctly 3D lattice that is extremely hard and electrically insulating.

While graphite is a conductor, vdW materials come in all types. vdW semiconductors (WSe_2, MoS_2), metals (graphite, $TaSe_2$), superconductors ($NbSe_2$, 1T′-$MoTe_2$), insulators (BN, Bi_2SeO_5), magnets (CrI_3, CrSBr), semimetals (graphene, $ZrTe_5$), topological insulators (WTe_2, Bi_2Te_3), and more are all abundant, [15][17] many of which have been characterized all the way down to the monolayer limit. One remarkable thing about vdW materials is that the vdW force is chemistry agnostic, so it is possible to stack different materials on top of each other. These materials can have radically different properties, opening the way for the design of complex devices. For example, stacking graphite (metal) on BN (insulator) on WSe_2 (semiconductor) can form a MOSFET that is only a few atoms thick. Heterostructures created with vdW materials can realize nearly all of the same physics observed in GaAs 2DEGs while also greatly expanding

measurement geometries. For instance, in quantum well 2DEGs, the existence of a Wigner crystal had to be inferred as the well is buried within a solid. With vdW materials, the 2D system can be probed directly with a technique like scanning tunneling microscopy (STM). Multiple recent STM works have demonstrated Wigner crystallization in 2D devices, [18][19][20] directly imaging lattices of electrons and holes as Wigner predicted nearly a century ago.

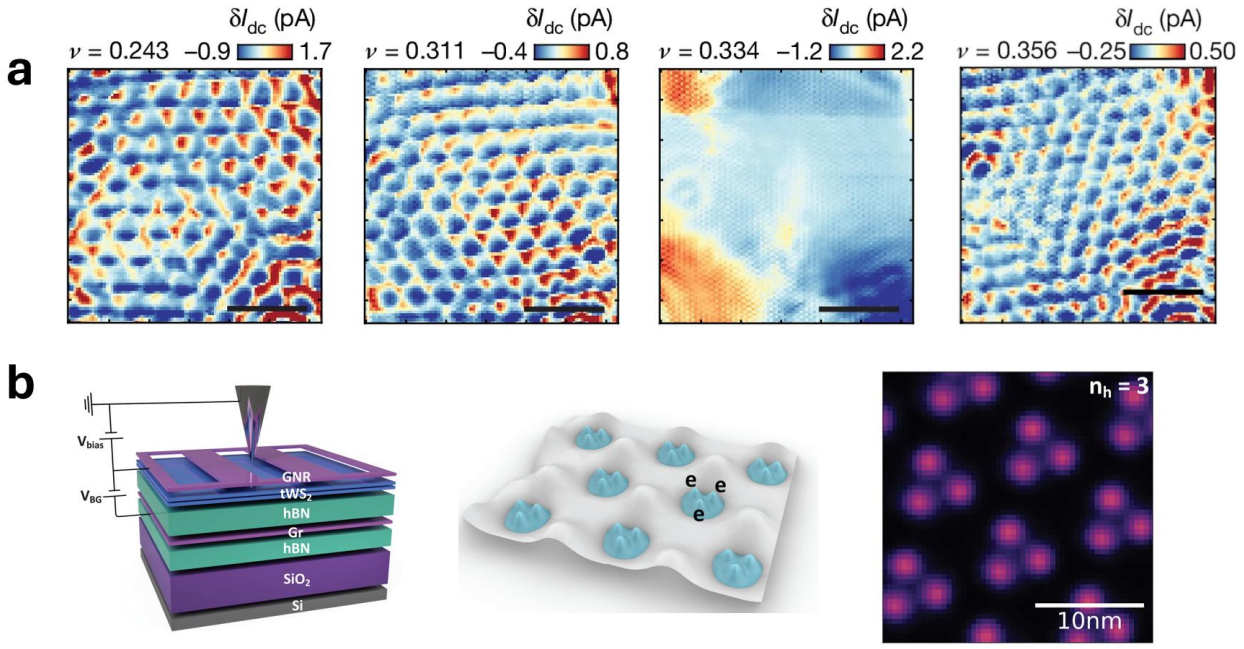

Figure 1.3: Two 2024 publications demonstrating Wigner crystallization in different vdW systems. (a) Reproduced section of Fig. 2 from [19] showing STM tunneling current modulations in bilayer graphene at various filling factors ν. At $\nu = 1/3$, the electrons form a correlated quantum liquid in a fractional quantum Hall state, melting the crystal. ($B = 13.95$ T, electron temperature $T = 210$ mK, scale bar is 100 nm) (b) Reproduced sections of Figs. 1 and 2 from [20]. The first panel shows a schematic for the device, using a graphene nanoribbon (GNR) to contact the twisted bilayer WS_2 sample. Charge carriers trapped in the resulting moiré potential wells repel each other, forming the repeating triangular pattern seen via STM in the final panel. ($T = 5.4$ K)

As these works demonstrate, combining vdW materials can create ideal 2D systems for measuring previously inaccessible physics. The permutations of heterostructures are nearly endless. Inert materials can be used to encapsulate air-sensitive materials for measurement.

Conductive materials can be used as contacts or dopants for semiconductors. Semimetals can be used for remote sensing or screening. Materials can be twisted, creating moiré superlattices that would never naturally occur. As described by Feynman in a prescient 1959 speech, "What could we do with layered structures with just the right layers? […] when we have some control of the arrangement of things on a small scale, we will get an enormously greater range of possible properties that substances can have and of different things that we can do." [21]

1.2 2D TRANSPORT

In physics, "transport" refers to the general process of something being moved through space or time. For our purposes, we will take "transport" to mean "electronic transport," the movement of charge carriers in a material. A typical transport measurement subjects a 2D sample to a small near-DC current or voltage bias. The resulting voltage drop or current across the sample is measured, from which the conductance and resistance are calculated. By adjusting the external conditions (temperature, displacement field, magnetic field), we can track changes in the response and infer underlying physical mechanisms for our data. While transport is simple to describe, it is often complex to execute and interpret, so we will spend some time discussing these key details.

1.2.1 *Device Design and Fabrication*

Fabricating 2D devices is a challenging and involved process, the many nuances of which lie outside the scope of this work. In broad terms, the fabrication process begins by exfoliating 2D materials for the device. Bulk crystals are stuck to a tape that is repeatedly folded over onto itself to cleave the crystal apart, covering the tape. That tape is then copied to other tapes which are applied to Si wafers with an SiO_2 oxide grown on top. The wafers are then heated and cooled, and the tapes are slowly peeled off, transferring 2D material onto the SiO_2. The oxide enhances optical

contrast, giving the deposited flakes of material distinguishable colors when searching with a microscope. [16] Once suitable flakes (correct size, shape, flatness, thickness, etc.) have been identified, they can be stacked via a dry transfer technique. In this process, a polycarbonate (PC) film is stretched over a PDMS polymer to create a "stamp." By heating the substrate, the PC film softens and can be used to pick up a flake of 2D material, holding it on the stamp. [22][23] From here, other flakes can be picked up using the same procedure, forming a stack of flakes held together by the vdW force. By further heating the stamp, the stack and film can be released onto a new substrate. The film is then chemically dissolved, leaving behind only the 2D heterostructure.

Exact details depend on the design and purpose of the device being fabricated, but the general layout of 2D transport devices is fairly universal. Since 2D materials have such low screening, an out of plane displacement field can meaningfully shift the Fermi energy. As such, most 2D devices utilize electrostatic gating, placing the sample between two metallic gates that can generate a large displacement field. These gates are kept isolated from the sample via insulating spacers, making the device resemble a parallel plate capacitor filled with a dielectric and the sample in the middle. A typical 2D transport device is structured in the following way: a bottom gate (BN on top of graphite) is prepared, and platinum contacts are evaporated onto it. The platinum connects to thicker gold contacts which extend hundreds of microns away from the device to large pads for wirebonding, bridging electrical contact from the 2D material up to the macroscopic scale. The contacts are patterned into shapes conducive to transport measurements, such as a Hall bar or van der Pauw geometry. [24][25] The contacts are then annealed and mechanically cleaned via atomic force microscopy (AFM) to remove any debris or residue. Finally, the sample material is exfoliated in air or an argon glovebox. The top gate and sample are picked up with a stamp, aligned to the bottom gate, and melted down, completing the device.

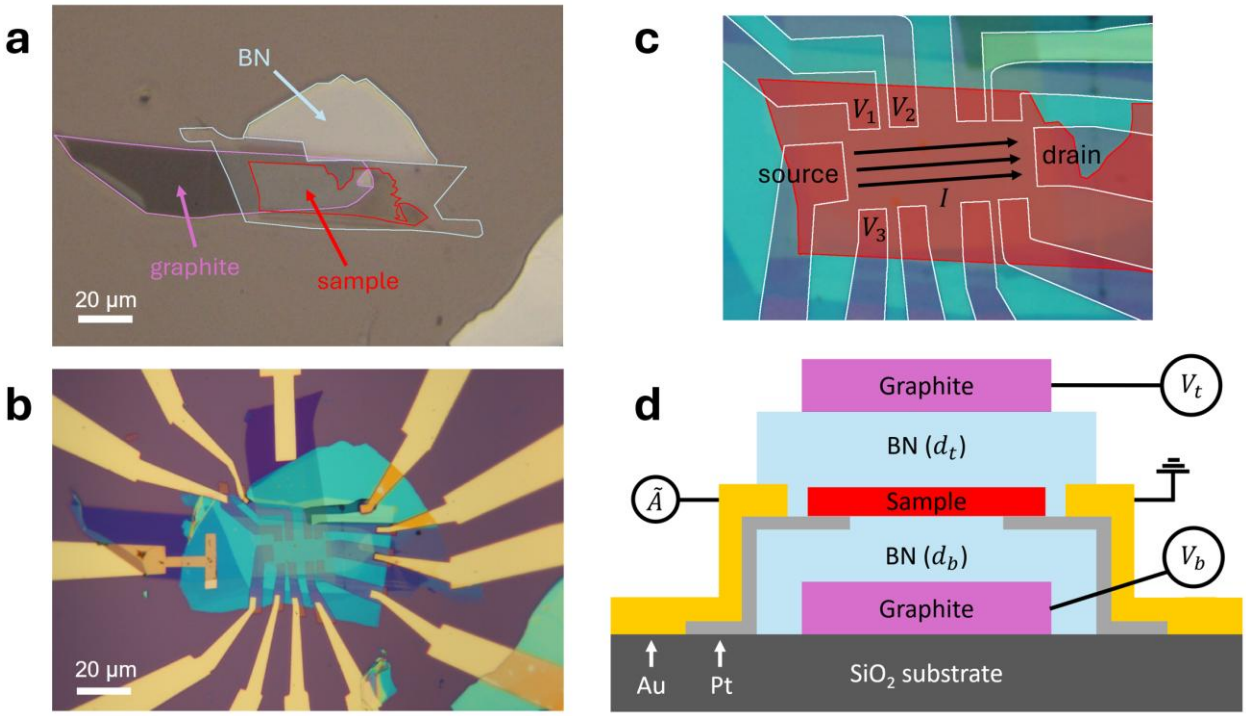

Figure 1.4: A typical 2D transport device. (a) The top gate (graphite and BN) with the sample to be measured (bilayer 1T′-$MoTe_2$) on a stamp, looking down through the stack. (b) Optical micrograph of the completed device. Top and bottom gate graphite flakes can be seen on the left and top of the image respectively. Gold contacts extend far beyond the field of view. (c) Closeup of the central region of the device with the sample and Pt contacts outlined. Current I is passed from source to drain (black arrows) while voltages are measured. Longitudinal and transverse resistances can be obtained via $R_{xx} = \frac{V_1 - V_2}{I}$ and $R_{xy} = \frac{V_1 - V_3}{I}$. (d) Side view schematic of the device. Applying gate voltages V_t or V_b creates an out of plane displacement field through the BN that shifts the Fermi energy of the sample. Thicknesses are not to scale.

1.2.2 *Interpreting Transport Measurements*

Let us focus on interpreting transport measurements for a simple, well-understood 2D system: bilayer graphene. The knowledge gained will be critical later when interpreting the physics of more complex systems in Section 2.3. We have already described how electrostatic gating can tune the Fermi energy of a 2D material, exposing physics away from neutrality. The exact combination of gate voltages is important, as the gates may either change the carrier density, apply an out of plane

displacement field, or some combination of the two. The carrier density and displacement field of a sample like the one shown in Figure 1.4 are given by the following: [25]

$$n = \frac{\varepsilon_0 \varepsilon_{BN}}{e}\left(\frac{V_b}{d_b} + \frac{V_t}{d_t}\right) \qquad D = \frac{\varepsilon_0 \varepsilon_{BN}}{2}\left(\frac{V_t}{d_t} - \frac{V_b}{d_b}\right)$$

We assume the same relative dielectric constant ε_{BN} for both gates. We see that it is possible to change the doping of the sample without applying a displacement field and vice versa. These effects can be easily observed in bilayer graphene. In the ground state, bilayer graphene has parabolic bands that touch at the Fermi energy, but displacement field breaks the layer inversion symmetry, lifting the degeneracy at the K and K' points and opening a bandgap whose size increases with field. [26][27] Therefore, increasing displacement field while keeping doping unchanged should result in an increasingly insulating feature in our transport measurements. If we instead keep the displacement field zero and change the doping, we should see conduction on both the electron and hole sides. Indeed, this is what we see in the 2D gate map in Figure 1.5. In this measurement, we measure the resistance of the sample while changing gate voltages. By normalizing the gate voltages by their BN thicknesses, we can compare the fields generated by each gate. A line with slope -1 on this plot represents a contour of constant density (gate voltages are proportionally equal and opposite) while a line with slope $+1$ represents a contour of constant displacement field (gate voltages are proportionally equal). Along the $n = 0$ contour, we see an insulating feature that broadens away from the origin (i.e. with increasing displacement field), qualitatively matching the theory prediction. This measurement is representative of the interpretation of transport data, with more complex systems requiring more advanced techniques and care. Extracting quantitative physical parameters (intrinsic doping, mobility, gap size, etc.) or exploring systems with little to no theoretical modeling requires additional measurements and subsequent analysis. This will be the case for the graphene-WTe_2 hybrid presented in Chapter 2.

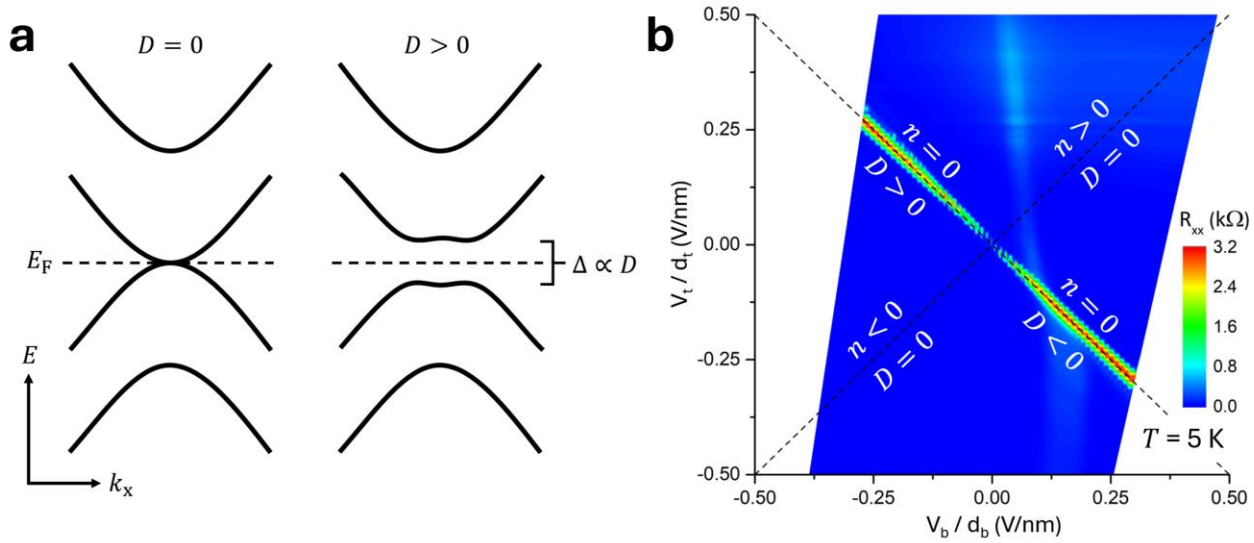

Figure 1.5: Band structure [26] and transport data for bilayer graphene. (a) Band diagram at K and K' points for bilayer graphene. Parabolic bands touch at the Fermi energy, but applying a displacement field opens a gap Δ that scales in size with the field strength. (b) Longitudinal resistance of bilayer graphene. Four quadrants are identified depending on their combination of carrier density n and displacement field D. The resistive feature aligns with the line of zero carrier density and varying displacement field, broadening away from the origin as the gap increases.

1.3 Summary and Outline

We have seen the flexibility and utility of vdW materials and 2D systems more broadly. Their unique combination of low screening, strong correlations, and ease of stacking has made them a playground for various exotic condensed matter phenomena. Within the breadth of the landscape of 2D materials, this thesis will be focusing on the topic of 2D semimetals, particularly the hybrid semimetal formed by the combination of monolayer tungsten ditelluride (WTe_2) and monolayer graphene. In Chapter 2, I will introduce both of these materials and discuss the resulting transport phenomena when combined. I will offer interpretations of this system as a hybrid of its constituent materials with some modifications. I will also extract various parameters for this system including intrinsic charge transfer, interlayer charge separation, and the WTe_2 density of states. Additional compressibility measurements using a remote graphene sensor will be used to quantify the WTe_2

gap. These measurements and analysis constitute the majority of this thesis. In Chapter 3, I will discuss research concerning the relatively understudied niche of 2D dielectrics, presenting a hitherto unreported inverted temperature dependence in hexagonal boron nitride (BN). I will also present measurements of the novel vdW insulator Bi_2SeO_5, a material with a high dielectric constant that may increase the range of accessible dopings for 2D devices. Finally, Chapter 4 will discuss the development of a two-axis rotator for turning samples within a magnetic field below 1 K, a difficult engineering problem that would greatly benefit future transport studies. While this project is still in development, it is nearly complete, and I will show preliminary results affirming the functionality of the system.

Chapter 2. Graphene-WTe_2: Hybrid Semimetal

In many ways, graphene and WTe_2 are foils of each other. Monolayer graphene is a gapless, centrosymmetric semimetal with weak spin-orbit coupling. It hosts massless Dirac fermions near the Fermi energy, resulting in exceptionally high mobility and weak intrinsic electron interactions. [29][30] On the other hand, monolayer WTe_2 lacks inversion symmetry, has strong spin-orbit coupling, and hosts a range of strongly correlated physics. This includes a putative excitonic insulator ground state; [31][32] a gate-induced, likely unconventional superconducting state; [33][34][35][36][37] and topological phenomena like the quantum spin Hall effect. [38][39][40][41] This chapter will discuss the hybrid semimetal formed by combining monolayer graphene with monolayer WTe_2, characterizing it through transport measurements. We find that the resulting system can be largely understood from the properties of the constituent materials with modifications due to spontaneous charge transfer and electron-electron interactions.

2.1 2D Semimetals

Semimetals, materials with a very small bandgap or band overlap, are relatively rare in nature. Only two semimetals have been extensively studied in the monolayer limit, graphene and WTe_2. The weak screening and small carrier populations of 2D semimetals open the door for strongly correlated physics, and the few 2D semimetals that have been studied have proven to be extremely rich systems hosting exotic phenomena. [42] In order to interpret the combined graphene-WTe_2 system, it is important that we first characterize each material individually. We will place an emphasis on monolayer WTe_2, as its behavior is more complicated than graphene, less understood, and also more likely to be the source of any correlated physics in the hybrid.

2.1.1 *Monolayer Graphene*

Monolayer graphene is the most famous and best studied 2D material. It is formed of a honeycomb lattice of carbon atoms, i.e. two interpenetrating triangular sublattices. Its Fermi energy coincides with the Dirac point, the intersection of the valence and conduction bands. Electrons near the Fermi energy in graphene have a linear dispersion and behave like massless fermions modeled by the Dirac equation. [28][29][30] The Dirac point is protected by symmetries of the lattice including inversion and time reversal symmetries, making graphene a gapless semimetal. Much more can and has been said about graphene, but for our purposes, we will focus on its behavior near the Dirac point and in a strong magnetic field.

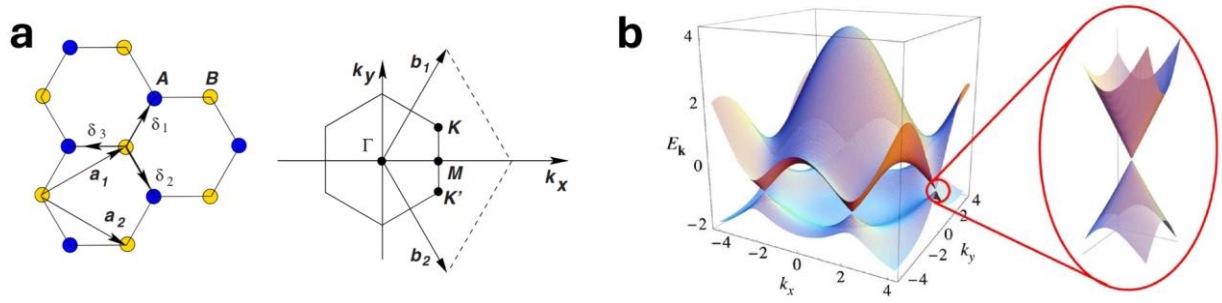

Figure 2.1: Lattice and band structure of monolayer graphene, reproduced from Figs. 2 and 3 of [29]. (a) Honeycomb lattice (left) and the Brillouin zone (right). Blue and yellow atoms mark the A and B sublattices. The K and K' points form two distinct valleys connected by time reversal symmetry. Combined with spin, this gives low-energy states fourfold degeneracy. (b) Electronic dispersion in graphene showing the Dirac cones. The valence and conduction bands have linear dispersions and meet at Dirac points located on the K and K' points of the Brillouin zone.

The conical band structure of graphene results in a low density of states near the Dirac point, meaning that even small amounts of doping can drastically shift the Fermi energy. This low density of states has a pronounced impact when combining graphene with other materials. Since charge carriers redistribute between the materials to align their chemical potentials, charge more

readily accumulates in the material with a higher density of states, making it more difficult to electrostatically dope the graphene. To be quantitative, the Fermi energy and density of states of pure graphene can be expressed in terms of carrier density n via

$$E_{\mathrm{F}}(n) = \hbar v_F \sqrt{\pi |n|}\,\mathrm{sgn}(n) \qquad D(E) = \frac{2|E|}{\pi(\hbar v_F)^2} \rightarrow D(n) = \frac{2\sqrt{|n|}}{\sqrt{\pi}\,\hbar v_F}$$

Here, $v_F \approx 10^6$ m/s is the Fermi velocity. [29] Consider a doping of 10^{12} cm^{-2}, a value easily achievable with electrostatic gating. The resulting density of states is 1.71×10^{10} cm^{-2} meV^{-1}, over twenty times lower than the reported density of states for the conduction band of monolayer WTe_2, 3.7×10^{11} cm^{-2} meV^{-1}. [31] This large discrepancy suggests that it will be difficult to tune the density of graphene when in contact with compressible WTe_2 even in the absence of screening.

The high mobility and low defect density of graphene make it a model system for 2D physics. We have already introduced the concept of Landau quantization in Section 1.1.1. When a 2DEG is placed in a sufficiently strong out of plane magnetic field, the resulting cyclotron orbits become quantized into discrete Landau levels, [9] with the same result holding true for Bloch electrons in a periodic potential like a crystal. [4] For the case of massless Dirac fermions in graphene, energy scales as the square root of magnetic field, $E(N) = \mathrm{sgn}(N)\sqrt{2e\hbar v_F^2 |N| B}$ where $N = 0, \pm 1, \pm 2$ ... is the index of the Landau level. [43] As the magnetic field or carrier density is varied, the Fermi energy moves between these discrete Landau levels. When the Fermi energy lies in the gap between Landau levels, bulk states are localized and transport only occurs through chiral edge states. Since backscattering is impossible, this results in the quantum Hall effect: longitudinal resistance vanishes ($R_{xx} = 0$) and the transverse resistance becomes quantized ($R_{xy} = \frac{1}{\nu}\frac{h}{e^2}$ for filling factor ν). [4] Graphene hosts both integer and fractional quantum Hall effects in sufficiently high fields and low temperatures. [44][45] Given the robustness of the Landau quantization in graphene, it should be easily resolvable in transport, even when in contact with WTe_2.

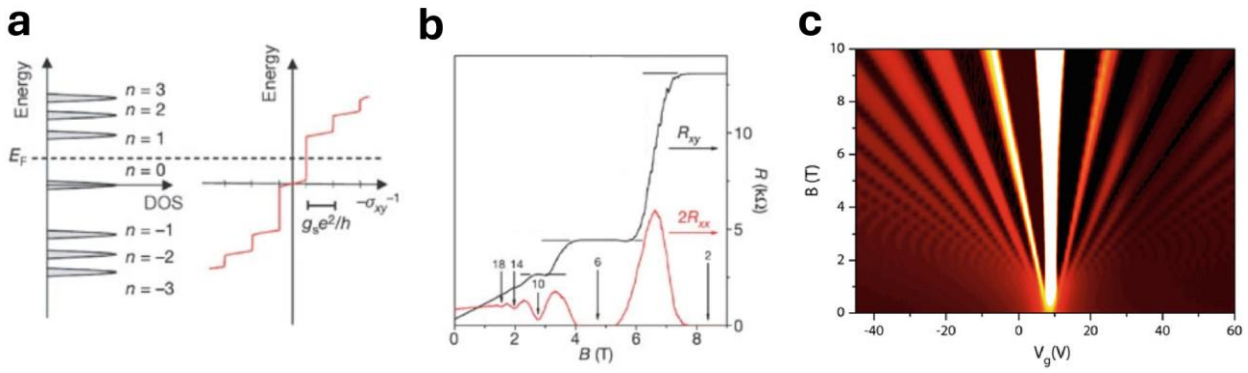

Figure 2.2: Schematics and transport data showing Landau quantization and the integer quantum Hall effect in monolayer graphene, reproduced from [44] and [46]. (a) Graphene Landau level density of states and corresponding quantum Hall conductance σ_{xy} as a function of energy. (b) Transverse resistance R_{xy} (black) and longitudinal resistance R_{xx} (red) at $T = 30$ mK. Vertical arrows indicate the filling factor ν. (c) Landau fan diagram (see Section 2.3.3) for a CVD-grown monolayer graphene device. R_{xx} is shown on the color scale; brighter is more resistive. ($T = 250$ mK) Discrete Landau levels emerge and spread with magnetic field. The horizontal axis shows silicon gate voltage. The fan's rightward shift from zero indicates intrinsic p-doping in the graphene since a positive gate voltage is needed to reach neutrality.

2.1.2 *Monolayer WTe_2*

Transition metal dichalcogenides (TMDs) are often the subject of study in the field of 2D transport, particularly in the monolayer limit. The most widely studied TMDs (MoS_2, WS_2, WSe_2, etc.) have a hexagonal 2H crystal structure and a semiconducting band alignment. In contrast, WTe_2 is a type-II Weyl semimetal in the bulk [47][48] that realizes a uniquely low symmetry 1T′ phase in the monolayer. In fact, it is the only TMD monolayer to have the 1T′ phase as its thermodynamic ground state. [40][49] This structure includes intrinsic band inversion—an inversion of valence and conduction bands—that heralds topological phases, as it is impossible to remove without closing a gap. As a result, monolayer WTe_2 was predicted to host the quantum spin Hall (QSH) effect in 2014, [49] a prediction that would be experimentally confirmed over the ensuing five

years. [39][40][41] Beyond the QSH state, monolayer WTe_2 can also be made to superconduct when gated. [33][34] Improved crystal quality has decreased the threshold doping for the onset of superconductivity to only 10^{12} cm^{-2}, [37] a remarkably dilute density.

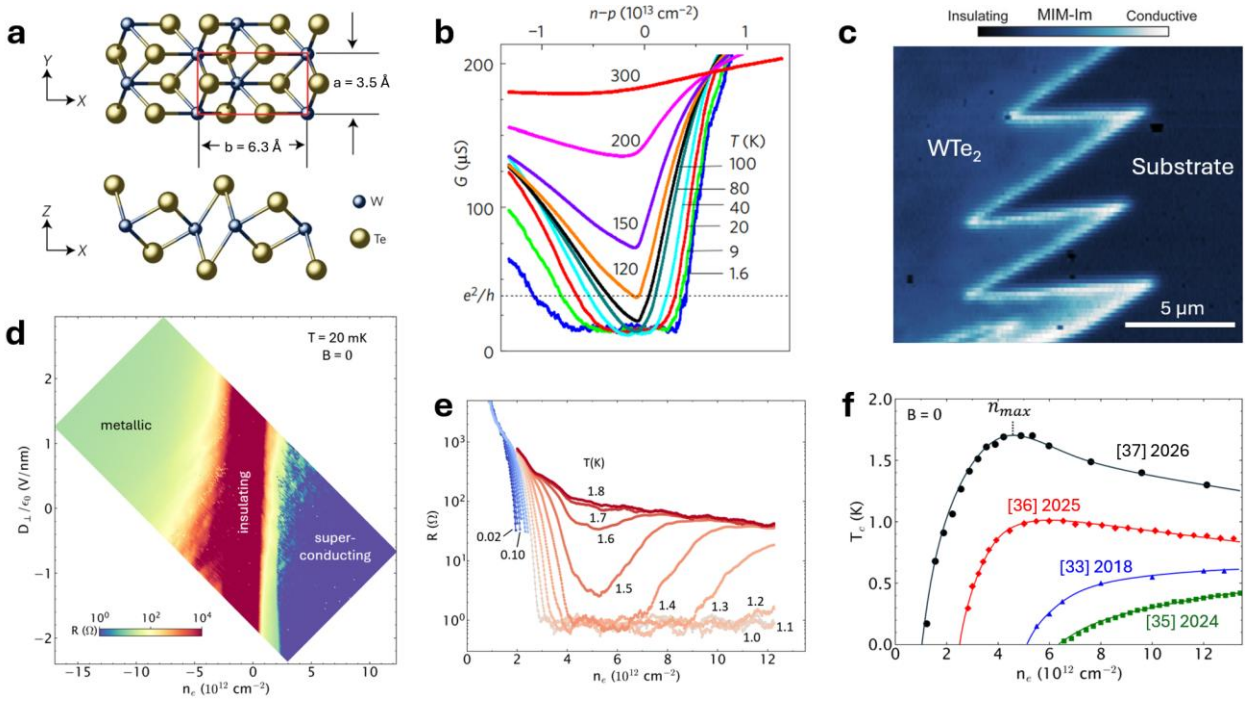

Figure 2.3: Quantum spin Hall effect and superconductivity in monolayer WTe_2. (a) Structural diagram of monolayer WTe_2, adapted from Fig. 1 of [40]. The 1T′ phase is orthorhombic and non-centrosymmetric. (b) Two-terminal conductance G as a function of temperature from Fig. 1 of [39]. An insulating feature emerges near charge neutrality upon cooling, broadening into a flat plateau that is skewed towards the p-doped side. (c) Microwave impedance matching (MIM) image showing a conducting QSH edge in monolayer WTe_2 from Fig. 1 of [41]. (d) Transport phase diagram showing superconductivity on the electron side at $T = 20$ mK. (e) Traces of resistance vs. temperature showing an onset of superconductivity below 1.7 K. (f) Superconducting phase diagrams demonstrating improvements in WTe_2 crystal quality. References and publication years are shown for each curve. For the most recent device, the critical temperature T_c reaches a maximum of ~1.7 K, and the minimum required doping is just above 10^{12} cm^{-2}. [37]

The insulating state below ~100 K in monolayer WTe_2 is believed to be excitonic in origin. An exciton is a bound state of an electron and hole that has a finite lifetime, typically the result of

a valence band electron being excited to the conduction band. However, in materials with an indirect band overlap such as WTe_2, electron and hole pockets coexist at the Fermi energy and can form excitons in equilibrium. Multiple transport studies support the formation of equilibrium excitons in monolayer WTe_2, leading to the claim that it is an excitonic insulator. [31][32] An excitonic insulator is a phase where excitons condense, opening a gap in a similar mechanism to BCS superconductivity. [50] In WTe_2, there are both electron and hole pockets at E_F with electrons at the ±Λ points and holes at Γ. As such, any spontaneously formed excitons would have a finite center of mass momentum equal to the Γ-Λ wavevector. Condensing these excitons breaks translational symmetry and should create periodic charge fluctuations in the form of a charge density wave (CDW) with wavevector $|q| \approx \frac{1}{6}\frac{2\pi}{a}$. [51] However, there has been no definitive evidence for the existence of a CDW. [31][32][52] Regardless, certain transport phenomena in monolayer WTe_2 require correlations to explain and are consistent with the formation of excitons in equilibrium. A striking example can be found in Sun *et al* in which a sharp vee appears in the conductance at a remarkably high temperature of 100 K, [31] reproduced in Figure 2.5.

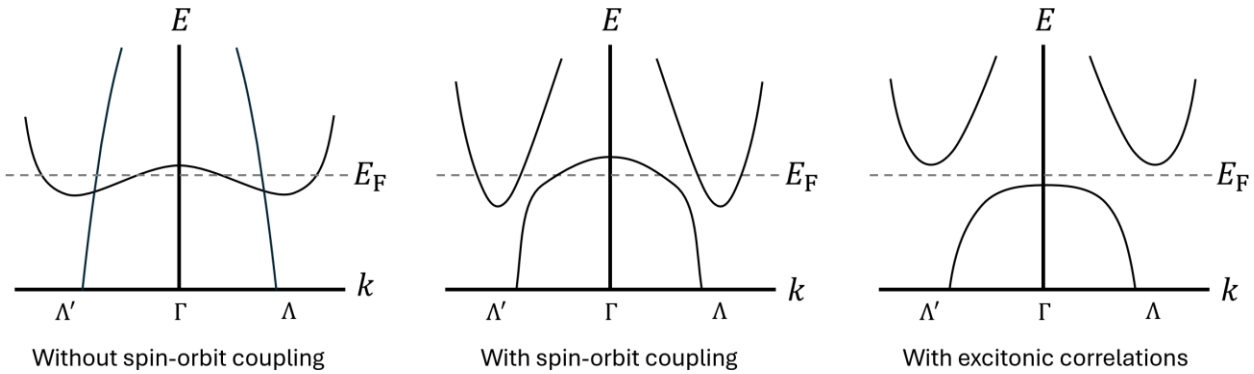

Figure 2.4: Band diagram for monolayer WTe_2. Without accounting for spin-orbit coupling, there is band inversion. Accounting for spin-orbit coupling creates two electron pockets at Λ and Λ′ and a hole pocket at Γ at the Fermi energy. These can pair up to form excitons, opening a gap. This figure is schematic only, as the detailed structure predicted by density functional theory (DFT) varies, with particular ambiguity surrounding the exact shape of the valence band edge.

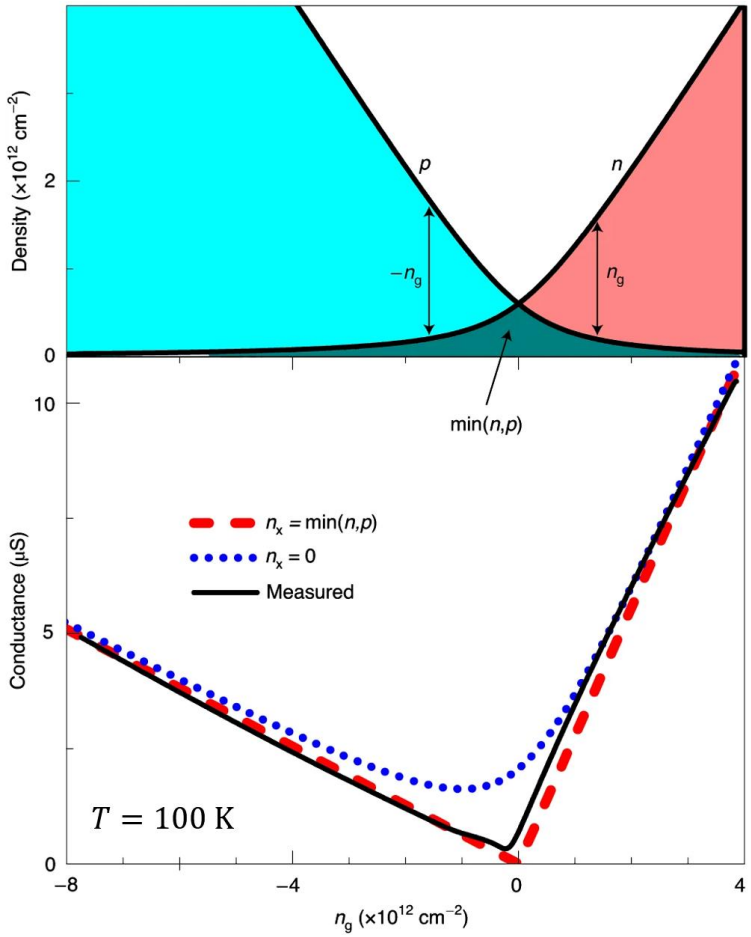

Figure 2.5: Conductance of monolayer WTe_2 reproduced from Fig. 4 of [31]. The total electron (n) and hole (p) densities in the top panel are calculated assuming constant densities of states for the valence and conduction bands. The sharpness of the vee at $T = 100$ K is remarkable and indicative of correlated physics. The dotted blue curve shows the expected thermal broadening in the single particle picture and is irreconcilable with the data. The red dashed curve assumes maximal pairing of electrons and holes into charge neutral excitons. While this model accurately reproduces the measured curve at 100 K, discrepancies emerge at higher temperatures. [31]

While transport is an excellent tool for characterizing materials, it offers little direct insight into their underlying band structure. Thankfully, other techniques help in this regard, the gold standard of which is angle-resolved photoemission spectroscopy (ARPES). This technique illuminates a sample with an x-ray light source (typically generated from a synchrotron) then measures the angles and momenta of photoemitted electrons in order to get a momentum-resolved

picture of the underlying band structure. [53] Multiple ARPES studies of monolayer WTe_2 have been reported in the literature, [40][54][55] but their findings are not always straightforward. For instance, Ref. [40] measures epitaxially-grown WTe_2 on a graphene substrate, and Ref. [54] uses graphene for encapsulation, potentially complicating matters. Both of these sources see the Fermi energy in the conduction band, suggesting intrinsic n-type doping of the WTe_2. In contrast, Ref. [55] uses an exfoliated WTe_2 monolayer encapsulated with BN and sees the Fermi energy pinned to the top of the valence band. Ref. [54] argues "the slight n-type doping of our WTe_2 sample is not dominated by charge transfer from graphene," but as we will in Section 2.3, this is likely untrue as contacting graphene intrinsically n-dopes WTe_2. Furthermore, the epitaxially-grown WTe_2 of Ref. [40] has domains smaller than the ARPES beam spot, meaning that multiple domains are sampled and averaged together into a single signal. It is noteworthy that the spectra do not significantly differ beyond intrinsic doping and the exact shape of the valence band, suggesting that graphene does not substantially affect the band structure of WTe_2.

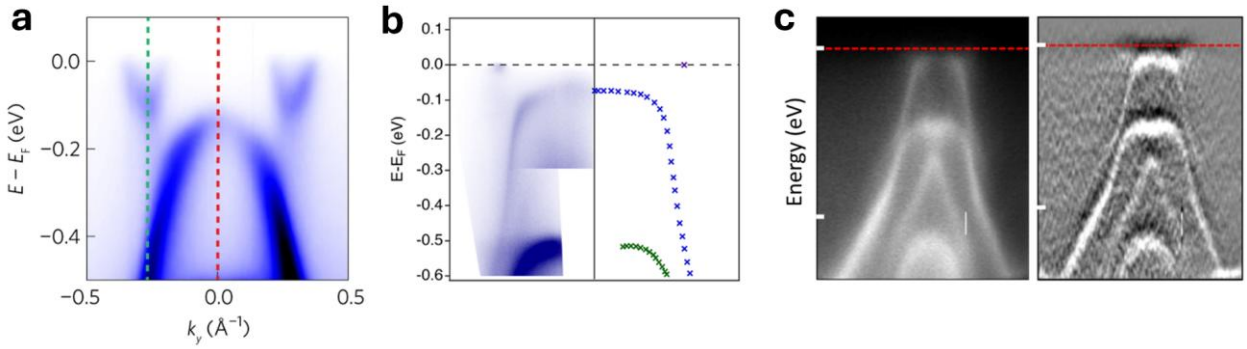

Figure 2.6: ARPES spectra of monolayer WTe_2 from various sources. (a) Section of Fig. 3 from [40]. It is difficult to resolve the gap, and substantial doping is present as the Fermi energy is well into the conduction band. ($T = 60$ K) (b) Section of Fig. 4 of [54]. The WTe_2 is slightly n-doped and the valence band edge is very flat. (T estimated between 30 and 40 K) (c) Section of Fig. 5.8 of [55]. The raw spectrum (left) and its second derivative (right) are shown. This sample appears undoped, as the Fermi energy is pinned at the valence band edge. ($T = 67$ K)

Beyond ARPES, scanning tunneling microscopy can also shed light on the underlying electronic structure of 2D materials. In STM, an atomically sharp tip is brought close to a sample's surface. By applying a voltage bias between the tip and sample, electrons can tunnel between them. The differential tunneling conductance $\frac{dI}{dV}$ is directly proportional to the local density of states (LDOS). Changing the tip-sample bias shifts the energy window of states that the tip samples, allowing for mapping of gaps, resonances, and other features. [56][57] Additionally, STM can indirectly infer band structure. When electrons elastically scatter from impurities or defects in a lattice, they conserve energy but change momentum. If a scattering event mixes two states with different wavevectors $\vec{k}_1$ and $\vec{k}_2$, then an interference pattern with wavevector $\vec{q} = \vec{k}_2 - \vec{k}_1$ appears in the norm of the quasiparticle wavefunction. The result is a modulation to the LDOS similar to Friedel oscillations with wavelength $\lambda = 2\pi/|\vec{q}|$. [57] Measuring these oscillations near a defect is known as quasiparticle interference (QPI), and while its resolution is far below that of ARPES, it provides another method for assessing the band structure of 2D materials like WTe_2. Tunneling and QPI measurements for epitaxially-grown WTe_2 are shown below.

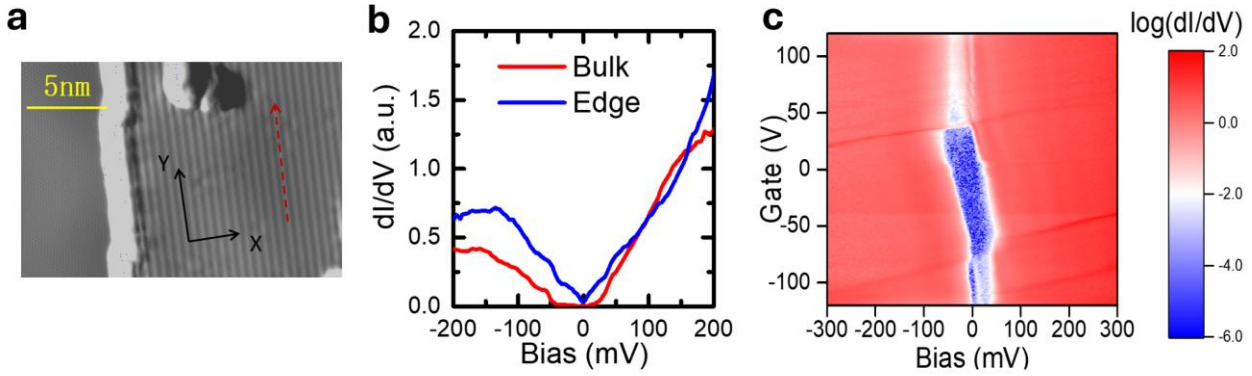

Figure 2.7: STM tunneling spectra for epitaxially-grown monolayer WTe_2 on graphene taken from [52]. (a) Topography of a WTe_2 monolayer with tungsten chains visible. (b) Tunneling spectra with a gap of ~60 meV visible in the bulk. (c) Tunneling current as a function of bias and gate. Conduction onsets more abruptly and at a lower doping on the electron side than the hole side, similar to the behavior observed in transport (c.f. Figure 2.3b).

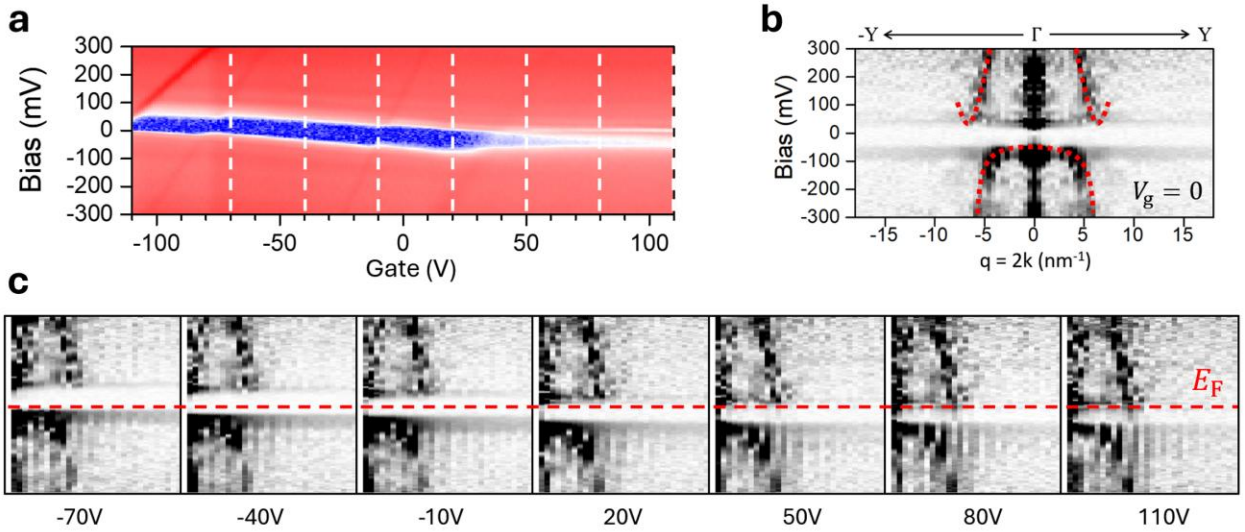

Figure 2.8: Quasiparticle interference (QPI) for epitaxially-grown monolayer WTe_2 on graphene adapted from [52]. (a) Reproduced plot of $\frac{dI}{dV}$ from Figure 2.7. White dashed lines indicate the gate voltages for which QPI spectra are calculated. (b) QPI-determined band structure at zero gate. A ~60 meV gap is clearly present, and the general band shape can be resolved, resembling ARPES spectra and theory calculations. (c) WTe_2 band structure with Γ on the far left of each panel. The Fermi energy E_F crosses the gap which begins to close above 50 V.

2.2 Hybrid Devices

Building a "hybrid" device of dissimilar materials presents some concrete logistical challenges. However, the use of graphene opens the door for fabrication techniques not possible with pure WTe_2. In this section, I will discuss the design and fabrication of hybrid graphene-WTe_2 devices, including the development of a self-aligned oxidation technique that may be applicable to the fabrication of other air-sensitive hybrid systems.

2.2.1 *Building a Hybrid Material*

A hybrid material, by definition, must be constructed from constituent materials. While it is fairly simple to stack 2D materials on top of each other, this does not necessarily make an ideal hybrid system. For example, consider the fact that we do not have control over the shape of exfoliated

flakes. It is therefore impossible to align flakes such that there are no regions of a single material and only the hybrid. As a consequence, any transport signal will measure not only the hybrid but also the pure graphene, WTe_2, or both. It is not feasible to cleanly separate these signals, so the resulting measurement will not accurately reflect the intrinsic properties of the hybrid.

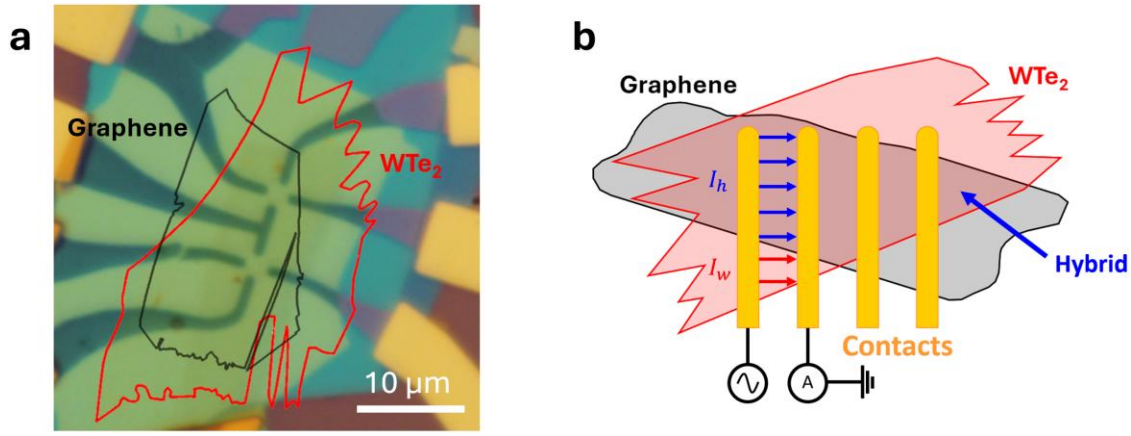

Figure 2.9: A hybrid device demonstrating the problem of parallel conduction. (a) Optical micrograph of the first graphene-WTe_2 hybrid device with flakes outlined. Only the region of overlap is the hybrid material. (b) Schematic showing parallel conduction in such a device. While most current flows through the hybrid, some also flows through pure WTe_2.

Therefore, we will need a processing step that shapes the flakes, removes any regions of pure materials and leaves behind only the hybrid. Fortunately, graphene in particular is well suited for various forms of patterning as it is mechanically strong and chemically inert. [58] Among the various shaping techniques used for making graphene transport devices, the most prominent is the use of 1D edge contacts. For this process, a heterostructure is first assembled without contacts. Then, AFM is used to identify a flat, clean region of the stack and a suitable transport geometry is sketched. Next, the stack is coated in PMMA, a resist that can be developed by dosing with electrons. The highly focused electron beam of a scanning electron microscope (SEM) can then selectively develop some regions of this PMMA which are then dissolved away. The remaining PMMA serves as a mask, protecting part of the stack from an oxygen plasma or reactive ion etch

(RIE) that eats through any exposed material. Finally, the remaining PMMA is dissolved and metallic contacts are evaporated, completing contact to the 1D edge of the graphene flake. [59] This is the standard fabrication process for modern graphene devices.

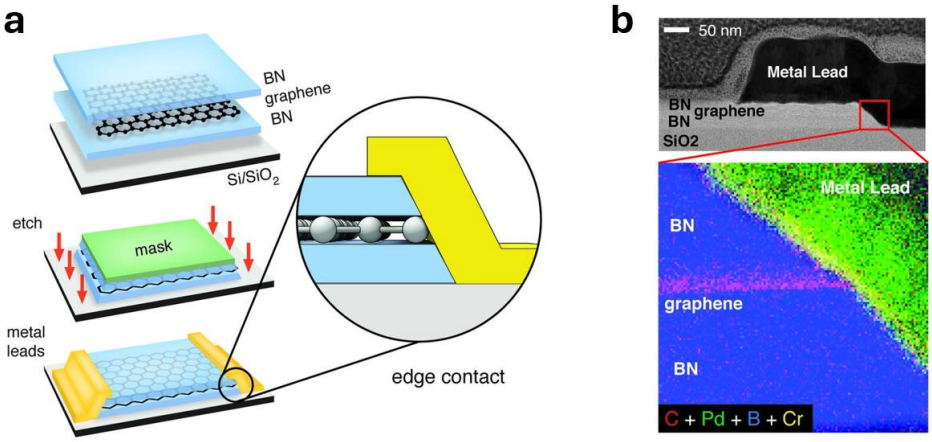

Figure 2.10: Reproduced Fig. 1 of [59] demonstrating the edge contact method for graphene. (a) Schematic of the fabrication process. Additional steps are required to etch and contact gates. (b) Side view of the edge contact, including a false-color electron energy loss spectroscopy (EELS) map showing the different materials at the interface between the graphene edge and the contact.

The main difficulty of fabricating graphene-WTe_2 hybrid devices lies in the WTe_2 itself, as it is extremely air-sensitive. Even inside a glovebox with ~1 ppm O_2, exfoliated WTe_2 monolayers can only survive for a few hours before degrading. This presents a problem for 1D edge contacts, as the edge of the material (where the contact occurs) must be exposed to both air and reactive etchants in the fabrication process. Luckily, WTe_2 is self-passivating, meaning that a partially exposed flake will not degrade in the covered region. [41] While oxidation makes pure WTe_2 etched devices impractical, etched hybrid devices should be achievable. Even though the edges of the WTe_2 will degrade, the final device will be almost entirely composed of hybrid material. The thin ring of graphene along the edge of the etched stack allows for contact to the hybrid while being sufficiently narrow to not impact transport measurements.

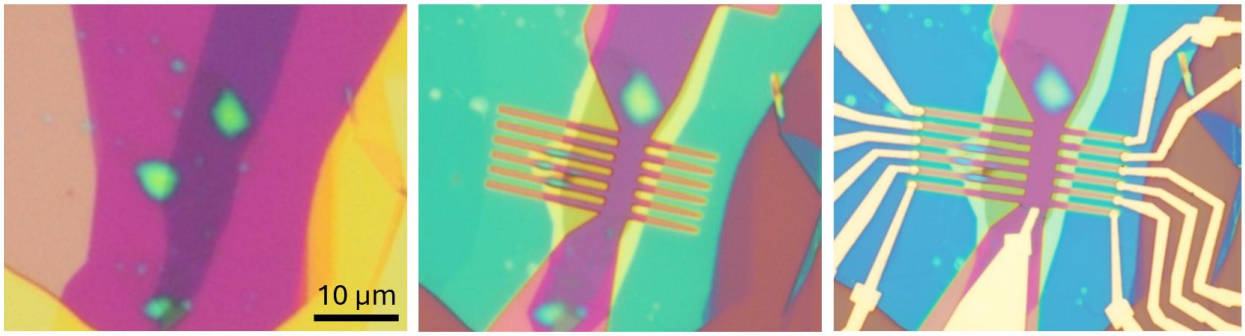

Figure 2.11: Fabrication of an etched hybrid graphene-WTe_2 device. The initial stack is etched into a Hall bar geometry, then metallic contacts are evaporated, completing the device.

2.2.2 *Self-Aligned Oxidation*

Another approach to building a graphene-WTe_2 hybrid utilizes the oxidation of WTe_2 to define the hybrid region. In addition to plasma etching, graphene can also be patterned via local anodic oxidation with an AFM. [60][61] This means that graphene can be made into an oxidation mask for the WTe_2. By picking up WTe_2 then picking up a pre-patterned graphene monolayer, part of the WTe_2 is occluded by the graphene. Exposing this stack to air for five minutes oxidizes any uncovered regions of WTe_2, leaving behind a hybrid in the shape of the etched graphene that can then be deposited onto pre-patterned contacts. We will refer to this technique as self-aligned oxidation, as the process of oxidizing the WTe_2 serves the function of aligning it to the graphene mask. I first developed this technique in 2021 and have used it in the fabrication of several hybrid devices. To date, other groups have independently utilized various oxidation techniques to selectively tune TMDs for a range of purposes, [62][63] but to my knowledge, ours is the only instance of deliberately oxidizing an air-sensitive material for use in transport. The technique is quite robust, with the main limitations being the additional processing time of pre-patterning contacts and etching the graphene. There is also concern over cracks forming in the WTe_2, though this is a known problem common to all WTe_2 transfers as a result of its mechanical brittleness.

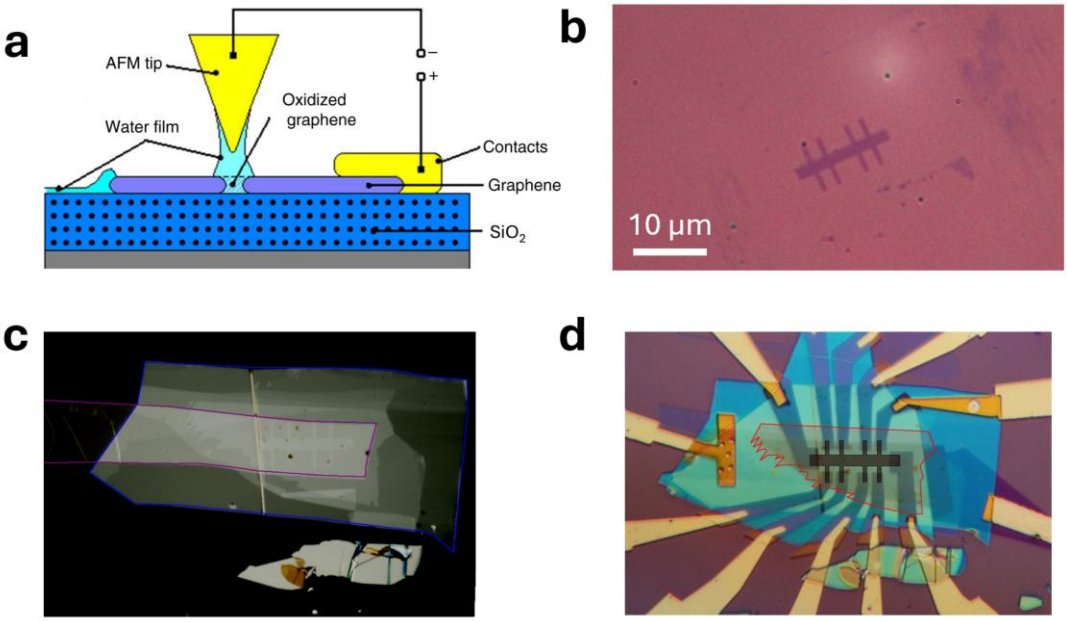

Figure 2.12: Self-aligned oxidation technique for hybrid devices. (a) Reproduced Fig. 3 of [61] schematically demonstrating the AFM etching process. A humidifier creates a water layer between the tip and sample to enable the etching. (b) Optical micrograph of a graphene monolayer that has been etched into a Hall bar. (c) Image of a WTe_2 monolayer and graphene Hall bar on a stamp with a top gate assembly. The BN and graphite of the top gate are outlined in blue and purple respectively. (d) Completed device with the WTe_2 and graphene monolayers outlined in red and black respectively. The region of WTe_2 not covered by the graphene is oxidized by exposing the stack to air before depositing it onto the bottom gate, making it electrically insulating.

It is important to assess the quality of the WTe_2 monolayer after exposure to air to both ensure complete oxidation of the exposed region and lack of degradation of the hybrid region. As with the plasma etching method, one way to confirm the lack of ingress of the oxidation is from the transport data itself. As we will see in Section 2.3, transport measurements show no signatures of pure graphene for either fabrication method, supporting the notion that the oxidation does not impinge on the hybrid region. For self-aligned oxidation devices, we can also check the quality of the interface via AFM. Under AFM, graphene and WTe_2 monolayers are known to read approximately 0.5 and 0.7 nm tall respectively. The compound resulting from exposing WTe_2 to

oxygen should give a different height reading than pure WTe_2, allowing us to confirm the degradation of the uncovered region. Indeed, this is what we see in AFM as demonstrated by Figure 2.13. The exposed region of WTe_2 entirely oxidizes, and the region covered by graphene remains pristine. In fact, this fabrication method may be superior to plasma etching as the oxidized WTe_2 creates a boundary that prevents additional degradation of the hybrid in subsequent fabrication steps. Essentially, the hybrid is hermetically sealed by the surrounding oxide.

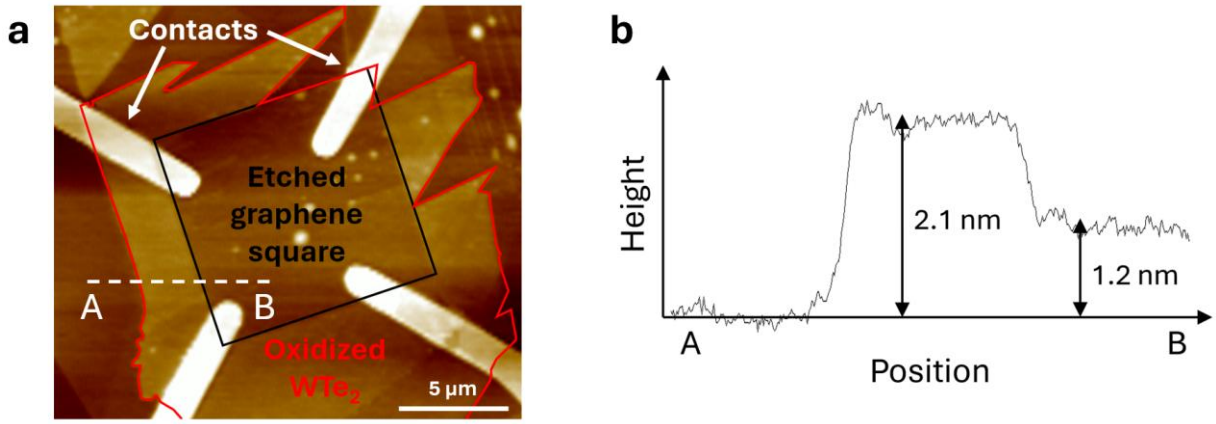

Figure 2.13: AFM height map of a self-aligned oxidation device demonstrating the complete oxidation of exposed WTe_2 and quality of the hybrid. (a) AFM height map of the completed device. Brighter colors mean taller features. Notice that despite the hybrid being composed of two flakes, it is darker than the surrounding oxidized WTe_2. (b) Line cut from point A to point B as indicated in (a). The central region corresponds to the oxidized WTe_2 and reads 2.1 nm tall, triple the thickness of pristine monolayer WTe_2 (~0.7 nm). The hybrid region near point B reads 1.2 nm tall, consistent with the sum of thicknesses of the individual monolayers as read by AFM, supporting the lack of ingress of oxidation into the hybrid region. The transition between regions is very sharp, implying that the boundary between the oxidized and pristine WTe_2 is quite narrow.

2.3 Transport Measurements

We have already alluded to some of the principles of transport measurements, and we will now utilize them to characterize the graphene-WTe_2 hybrid system. I will discuss the different types of measurements I have performed and carefully interpret them in the context of the information

presented in Section 2.1. We will see that the transport properties of graphene-WTe_2 can be understood largely in terms of the two component materials taking into account charge transfer, differences in densities of states, and correlations in the WTe_2. We will also perform an interpolation to recover maps of the individual layers' carrier densities n_g and n_w and use them to calculate quantitative properties of the hybrid system in Section 2.4.

2.3.1 *2D Gate Map*

Perhaps the simplest transport measurement to begin our characterization with is the 2D gate map. We have already been introduced to this measurement in Section 1.2.2 for bilayer graphene, but it is worth re-emphasizing the setup, as the graphene-WTe_2 system is more difficult to interpret. In this measurement, a small current I flows from source to drain, and voltage drops along (V_{xx}) and perpendicular to (V_{xy}) the current flow are measured. As described in Section 2.2, our hybrid devices have been shaped into ideal Hall bar or van der Pauw geometries, so we can find the resistance tensor elements R_{xx} and R_{xy} via $R_{xx} = \frac{V_{xx}}{I}$ and $R_{xy} = \frac{V_{xy}}{I}$. In the absence of intrinsic magnetism or an external magnetic field, R_{xx} is the primary signal of interest. The bottom and top gate voltages V_b and V_t can tune the carrier density via their sum or the displacement field via their difference. Normalizing the gate voltages by their dielectric BN thicknesses allows us to compare fields generated by each gate. It is common practice to convert these gate voltages to carrier density n and displacement field D, but since this is a hybrid system, these quantities are potentially ambiguous. As such, we will use normalized gate voltages $\frac{V}{d}$ instead.

A 2D gate map is shown in Figure 2.14c. The dominant feature is the nearly vertical resistance peak that undergoes a narrow diagonal transition in the bottom right quadrant near the edge of the accessible gate space (before the BN gate dielectrics break down). This peak is easily

resolvable in the $V_t = 0$ line cut at the top of the figure. In this device geometry, the graphene is being contacted. Graphene's spectrum has only one resistive feature in the form of its Dirac point, $n_g = 0$ where n_g is the carrier density of the graphene. The fact that this resistance peak is nearly vertical indicates that it is largely independent of the top gate voltage—the gate facing the WTe_2. We can therefore identify this feature as the graphene's Dirac point, the contour $n_g = 0$.

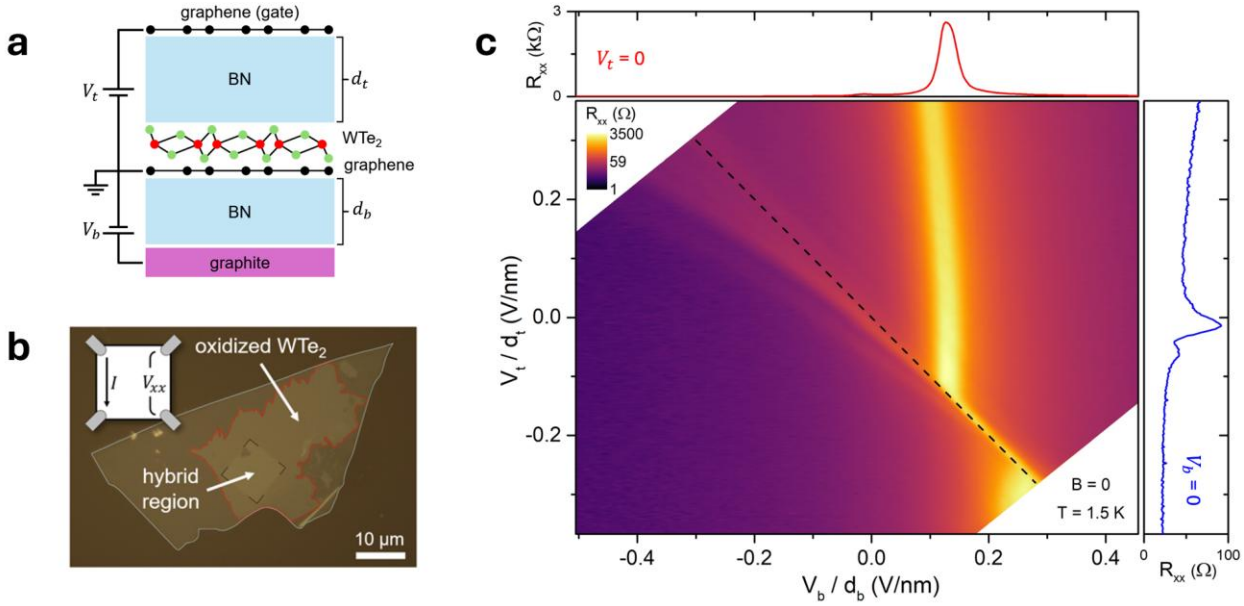

Figure 2.14: Device structure and 2D gate map for a graphene-WTe_2 hybrid device. (a) Side view device schematic. The top gate faces the WTe_2 and the bottom gate faces the graphene. The use of a graphene top gate will be explained in Section 2.5. (b) Optical micrograph of a hybrid sample before depositing. The graphene is etched into a square for a van der Pauw geometry (inset). (c) 2D gate map of R_{xx} for the hybrid. The black dashed line indicates the overall neutrality line, $n_{tot} = 0$. A logarithmic color scale is used to fully capture the finer details. Linear scale line cuts for zero top and bottom gate are shown in red and blue respectively.

In the bottom right quadrant, we see the graphene Dirac point overlapping with the overall neutrality line, $n_g = n_{tot} = 0$. Since the total carrier density is just the sum of the carrier densities of the two layers, $n_{tot} \equiv n_g + n_w$, it follows that the WTe_2 must also be neutral here, $n_g = n_w = 0$. That is to say that this narrow diagonal strip is the overall neutrality region of the system where

the graphene is neutral and the WTe_2 is gapped. When the WTe_2 is gapped, the graphene Dirac point is narrow and tracks both gates equally. When the WTe_2 is conductive, it screens the top gate, making the feature nearly vertical. The Dirac point also broadens, reflecting the disturbance of the electrostatic environment from the conducting WTe_2. The graphene Dirac point has been demonstrated to become dramatically narrower when proximate to a low-disorder metallic gate, reducing charge inhomogeneity and screening Coulomb disorder. [64] However, since WTe_2 is a comparatively low-density and inhomogeneous conductor, it imprints its charge disorder onto the graphene. This serves to enhance potential fluctuations in the graphene, broadening the Dirac point whenever the WTe_2 has finite compressibility.

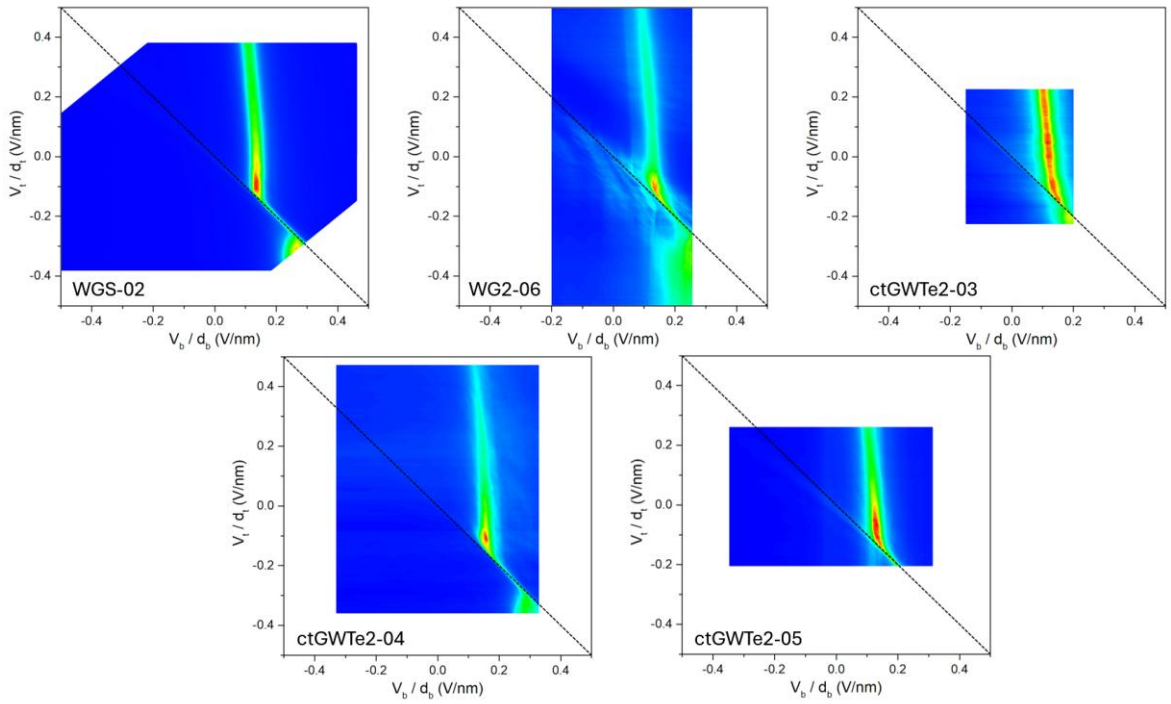

Figure 2.15: Consistency among various hybrid devices. Data are shown with different linear color scales for visual consistency. Both WGS-02 and WG2-06 are self-aligned oxidation devices using van der Pauw and Hall bar geometries respectively. All ctGWTe2 devices are etched Hall bars. Devices shown were fabricated over a three year period using different WTe_2 crystals but still show remarkably consistent transport character and charge transfer. The increased gating range of certain devices comes from the use of thin BN as will be explored in Chapter 3.

It is remarkable how far from the origin the overall neutrality region has shifted. This is a result of graphene's low density of states as described in Section 2.1.1. The location of the neutrality region in the lower right quadrant implies that we must add electrons to the graphene (positive bottom gate) and remove them from the WTe_2 (negative top gate) to reach overall neutrality. Both of these point to intrinsic charge transfer of electrons from graphene to WTe_2. We will quantify this charge transfer in Section 2.4. For now, let us note that all devices show consistent charge transfer, regardless of fabrication method or contact geometry. Moreover, none of the devices shown exhibit any transport characteristics of pure graphene. This is significant as it indicates negligible degradation of the WTe_2 in the hybrid. There is also a faint feature in Figure 2.14c below the $n_{tot} = 0$ line that gently curves down and is visible in the $V_b = 0$ line cut as well. It is reasonable to assume that this feature traces the WTe_2 neutrality contour $n_w = 0$, a statement we will prove rigorously in Section 2.3.4.

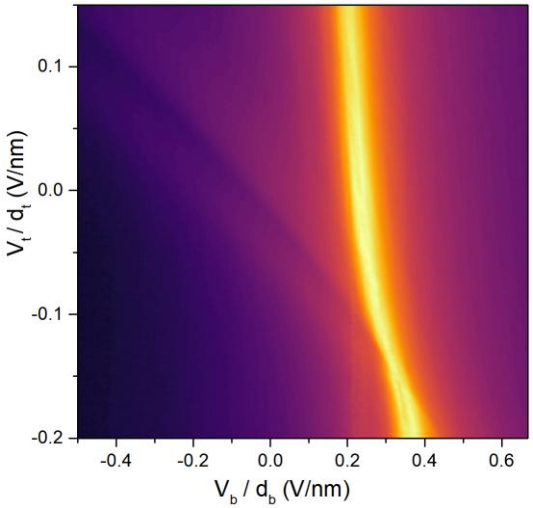

Figure 2.16: An example of a device with poor quality WTe_2. There is still clear evidence of charge transfer and the WTe_2 neutrality feature, and there are no signs of pure graphene, confirming the WTe_2 is still intact. However, the shape of the Dirac point is significantly different. The lack of a sharp gap suggests that the quality of WTe_2 is lacking, possibly due to an excess of tellurium vacancies. Improved WTe_2 growth remains an active subject of research. [37]

2.3.2 *Band Alignment Model*

To begin interpreting our transport results, we will develop a band alignment model. For simplicity, we begin by assuming that neither material's band structure is altered and the bands only move relative to each other in energy. It is simple to model the low-energy structure of graphene as it just has a linear band crossing at the Dirac point. Modeling WTe_2 is more complicated, as the presence of correlations violates the single particle band picture. [31] As such, we will use the density of states as a proxy for the bands, as this quantity can convey the same information while preserving generality. As a starting point, we model WTe_2 as a semiconductor with a fixed band gap and a constant density of states that is substantially larger than that of graphene. This is not the most accurate model, as it ignores differences between valence and conduction bands as well the diverging density of states at the valence band edge, [31] but it is capable of qualitatively describing the vast majority of observed transport phenomena.

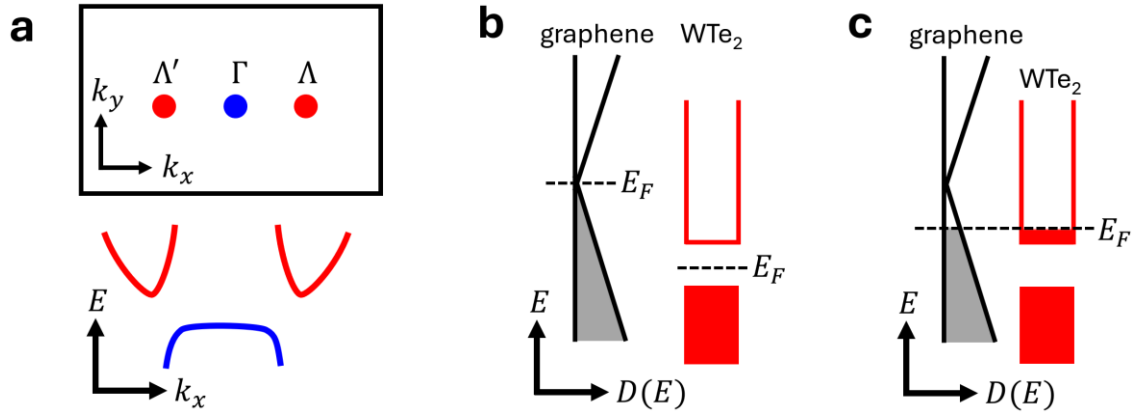

Figure 2.17: Band alignment model for graphene-WTe_2. (a) Band diagram of WTe_2 showing electron pockets at Λ and Λ' (red) and the hole pocket at Γ (blue). (b) Fermi energy of each material separately. The plot shows density of states on the horizontal axis and energy on the vertical axis for maximum generality. Graphene's Fermi energy coincides with the Dirac point, and WTe_2's lies in its gap. The figure is not to scale, and we consciously ignore the diverging density of states at the valence band edge for now. (c) Band alignment when graphene and WTe_2 are in contact with no gating. Aligning the Fermi energies forces spontaneous charge transfer between the layers.

When the materials are brought in contact with each other, their work function difference drives a flow of electrons out of the graphene and into the WTe_2 as shown in Figure 2.17c. Let us call this a p-n alignment, referring to the graphene-WTe_2 dopings. Returning our attention to the hybrid 2D gate map, we can identify three distinct regions by the dopings of the layers.

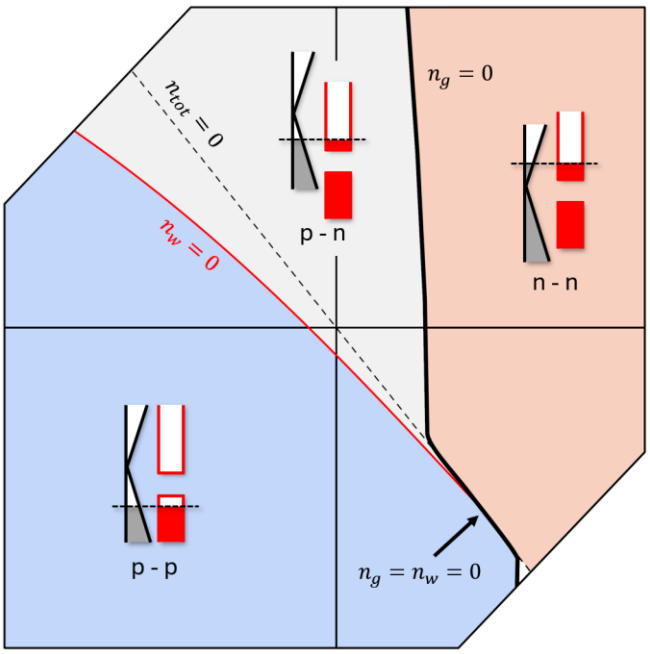

Figure 2.18: Band alignment for the different regions of the 2D gate space. The graphene-WTe_2 has a p-n alignment in the gray region including the origin (zero gating). Below the $n_w = 0$ contour in the blue region, the WTe_2 is hole doped, giving a p-p alignment. In the red region, both materials are electron doped, giving an n-n alignment. The n-p alignment region does not lie within our accessible gating range, but we should expect it in the bottom right.

2.3.3 *Magnetic Field Measurements*

As we have seen, the transport signal is largely dominated by graphene. By applying a magnetic field, we can force the graphene carriers into Landau levels separated by incompressible gaps. WTe_2 is comparatively unaffected by magnetic field with quantum oscillations only faintly emerging below 1 K at strong fields. [37] As a result, we should be able to resolve more features of the WTe_2 spectrum by applying an out of plane magnetic field to the hybrid. Specifically,

whenever the WTe_2 is insulating, we should see a quantum Hall signal in the graphene indicated by vanishing R_{xx} and quantized $R_{xy} = \frac{1}{\nu}\frac{h}{e^2}$. [4] Repeating the same 2D gate map measurements in the presence of magnetic field gives the following:

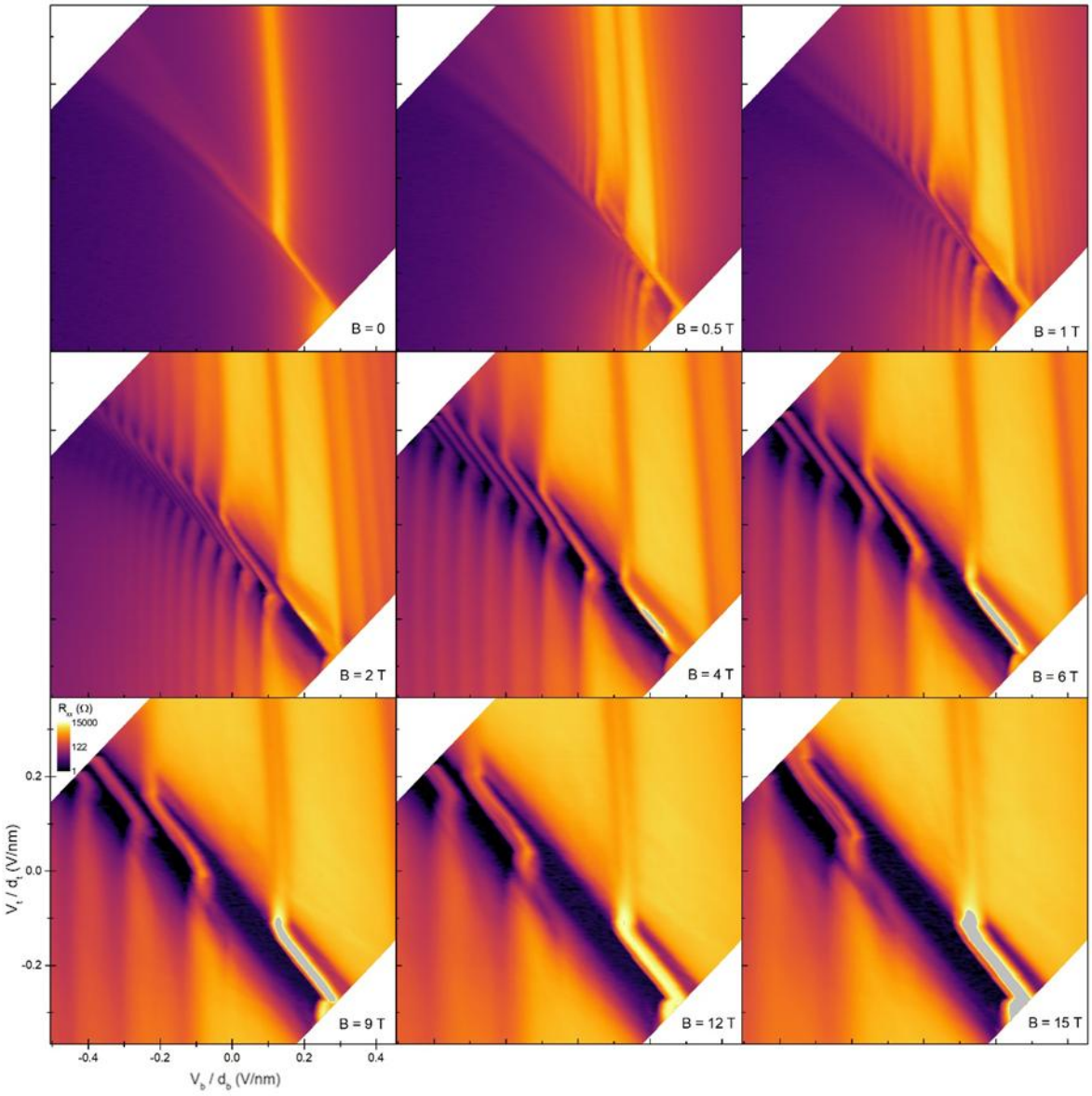

Figure 2.19: 2D gate maps of longitudinal resistance R_{xx} in the presence of magnetic field. All plots have the same axes and color scales. ($T = 1.5$ K) As magnetic field increases, Landau levels in the graphene spread in energy, resulting in multiple copies of the $n_g = 0$ contour. The black curved region that emerges above $B = 2$ T has vanishing R_{xx} and corresponds to insulating WTe_2. At the highest magnetic fields, the fourfold degeneracy of each Landau level begins to lift.

These 2D gate maps show an emerging region of vanishing R_{xx} that tracks the trajectory of the zero field feature identified as the $n_w = 0$ contour. Within this region, the graphene Landau levels form a distinct pattern of narrow diagonal transitions between broader vertical features. Effectively, these are copies of the Dirac point contour seen in the zero field data now corresponding to different filling factors ν. These Landau levels therefore trace out contours of constant n_g. This has incredibly useful implications that will be explored in Section 2.3.4. We confirm the presence of quantum Hall states in the graphene by plotting traces of R_{xx} and R_{xy}.

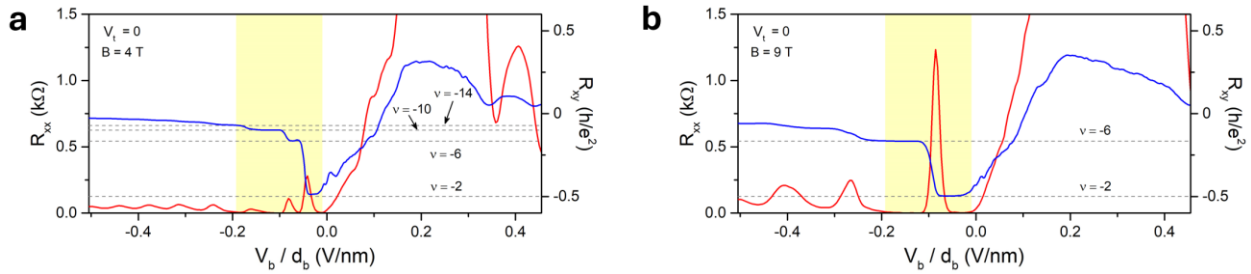

Figure 2.20: Line cuts of R_{xx} and R_{xy} at zero top gate for (a) $B = 4$ T and (b) $B = 9$ T. R_{xx} traces are shown in red and R_{xy} traces are shown in blue. The WTe_2 is insulating within the yellow window, giving quantized conductance in the graphene. Outside of this window, parallel conductance through the WTe_2 disrupts the quantization. ($T = 1.5$ K)

We can glean additional information by creating a Landau fan diagram for this hybrid system. A Landau fan measurement varies carrier density or gate voltage at a range of magnetic fields in order to see the evolution of Landau levels. A typical example for monolayer graphene is shown in Figure 2.2. The gate voltage tunes carrier density, meaning $\Delta V \propto \Delta n$. Since graphene has spin and valley degrees of freedom, each Landau level holds four electrons, so moving across one changes the carrier density by an amount $\Delta n = \frac{4eB}{h}$. This gives a linear relationship between gate voltage and magnetic field, resulting in a spreading fan with all lines projecting to the graphene's neutrality point at zero magnetic field. When the WTe_2 is incompressible, the hybrid

system behaves as intrinsic monolayer graphene in transport, so we should expect to see a well-defined Landau fan that projects to near zero gating at zero field.

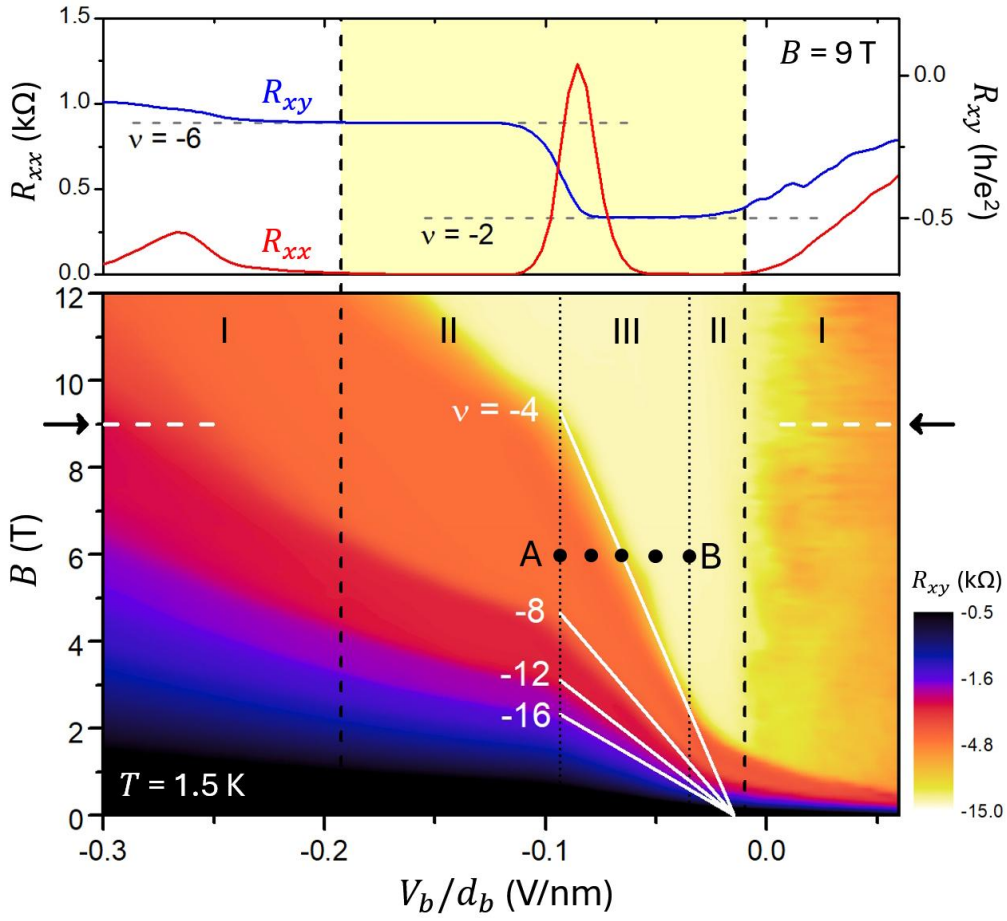

Figure 2.21: Hybrid Landau fan diagram with line cuts at $B = 9$ T. Three distinct regions can be identified. In region I, there is no quantization as the WTe_2 is conductive. This can be seen in both the line cuts and Landau fan, particularly on the right side (n-doped WTe_2). In region II, R_{xy} is quantized, but the Landau fan is not linear, implying insulating but compressible WTe_2. In region III, the WTe_2 is gapped (insulating and incompressible), and we see a Landau fan consistent with monolayer graphene with slight intrinsic n-doping. The white lines are calculated for graphene with intrinsic doping being the only free parameter. Points from A to B are shown in Figure 2.22.

The Landau fan shows nuance not present in the line cuts of Figure 2.20. Those showed two distinct regimes of transport, one of which saw quantized conductance in the graphene when the WTe_2 is insulating, and the other of which saw conductive WTe_2 disrupting that quantization.

However, we see three distinct regions in the Landau fan. Region I has the same disrupted quantization as a result of conductive WTe_2. Regions II and III on the other hand both see quantized conductance in the graphene, but they have different characteristics in the Landau fan, with region III having a linear fan dispersion with field and region II seeing that disrupted. We will discuss region III first, as it is simpler to interpret. In this region, the WTe_2 is both insulating and incompressible, that is to say gapped. As such, it has a negligible effect on the graphene, so the Landau fan resembles that of pure monolayer graphene. The intrinsic n-doping of the graphene is found to be $n_0 = 1.8 \times 10^{11}$ cm^{-2}, consistent with other graphene transport devices.

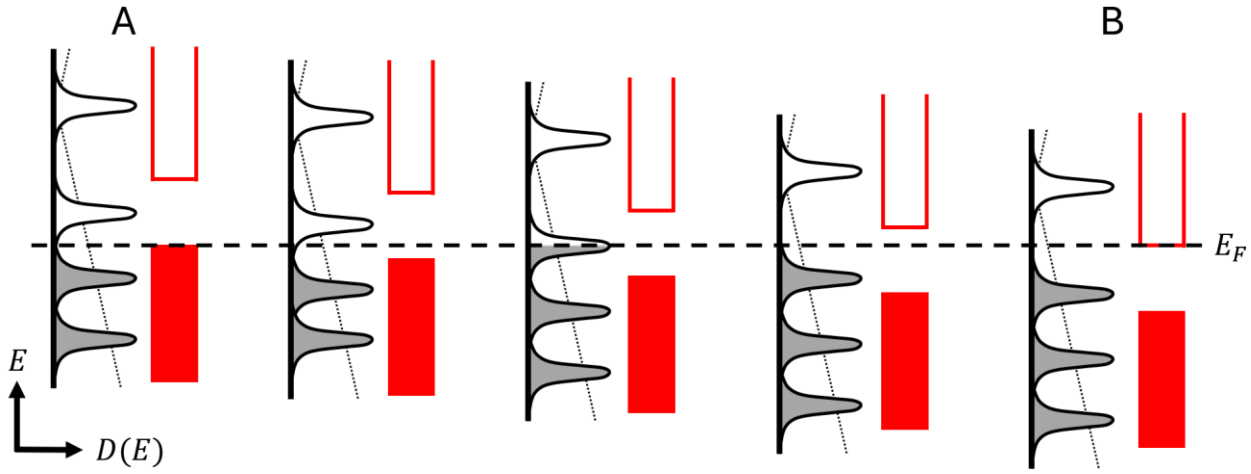

Figure 2.22: Band alignment diagram at the indicated points of region III in Figure 2.21. The graphene density of states has a comb-like structure as a result of Landau quantization. [44] From point A to point B, the $N = -1$ Landau level is filled and the WTe_2 gap is crossed.

Region II is more difficult to interpret, as there is seemingly a discrepancy between the shape of the Landau fan and the R_{xy} line cuts. Since the graphene transport is quantized, there cannot be any parallel conductance through the WTe_2, implying it is insulating. However, since the slope of the features in the Landau fan changes, the WTe_2 is no longer incompressible. We are left with the peculiar conclusion that the WTe_2 is both insulating and compressible in region II. This implies that it is possible to add charge to the WTe_2, but that charge remains localized. This

behavior is also observed in intrinsic monolayer WTe_2 [31][39] where transport measurements indicate a wide insulating range in doping despite compressibility measurements showing incompressibility only at charge neutrality. Such behavior is not predicted in conventional theory of neutral excitonic insulators. Sun *et al* offer a potential explanation, saying "it seems possible that the Coulomb interaction, which has a long range for these doping values, could stabilize both the excitonic phase and the Wigner crystallization of unbound carriers, whose effective mass is enhanced by the opening of a many-body gap." [31][65] Turning our attention back to the 2D gate maps of Figure 2.19, we can see that the region of vanishing R_{xx} includes areas where the narrow diagonal features of the graphene become nearly vertical and slightly broadened, reflecting this same behavior. The narrow diagonal features correspond to insulating and incompressible WTe_2 (region III) while the edges correspond to insulating but compressible WTe_2 (region II). Region II extends further on the WTe_2 hole side than the electron side in all measurements, including those of pure WTe_2. [31][39] These regions are highlighted in Figure 2.27.

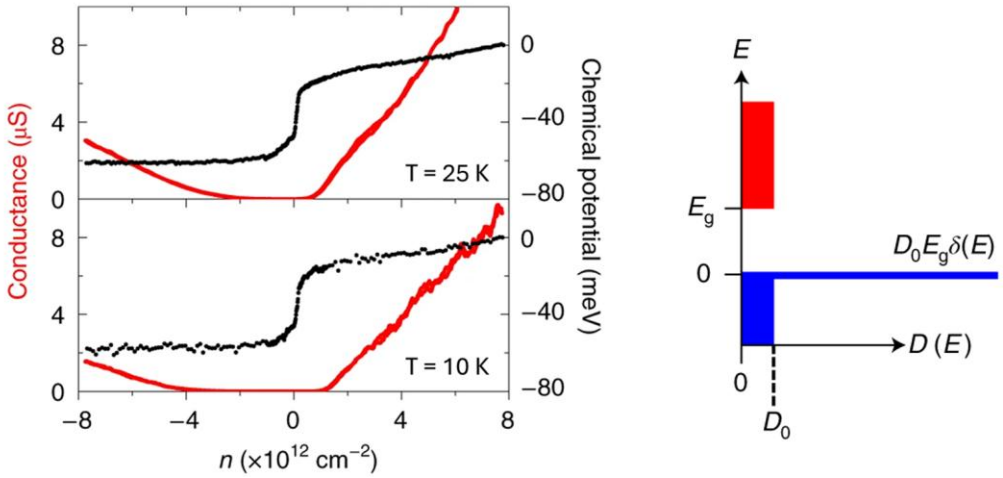

Figure 2.23: Reproduced sections of Fig. 3 of [31]. Insulating behavior is observed over a wide doping range. The chemical potential is nearly independent of density below neutrality, implying a diverging density of states $\frac{dn}{d\mu}$ at the valence band edge (right). This diverging density of states is likely responsible for the increased width of region II on the hole side.

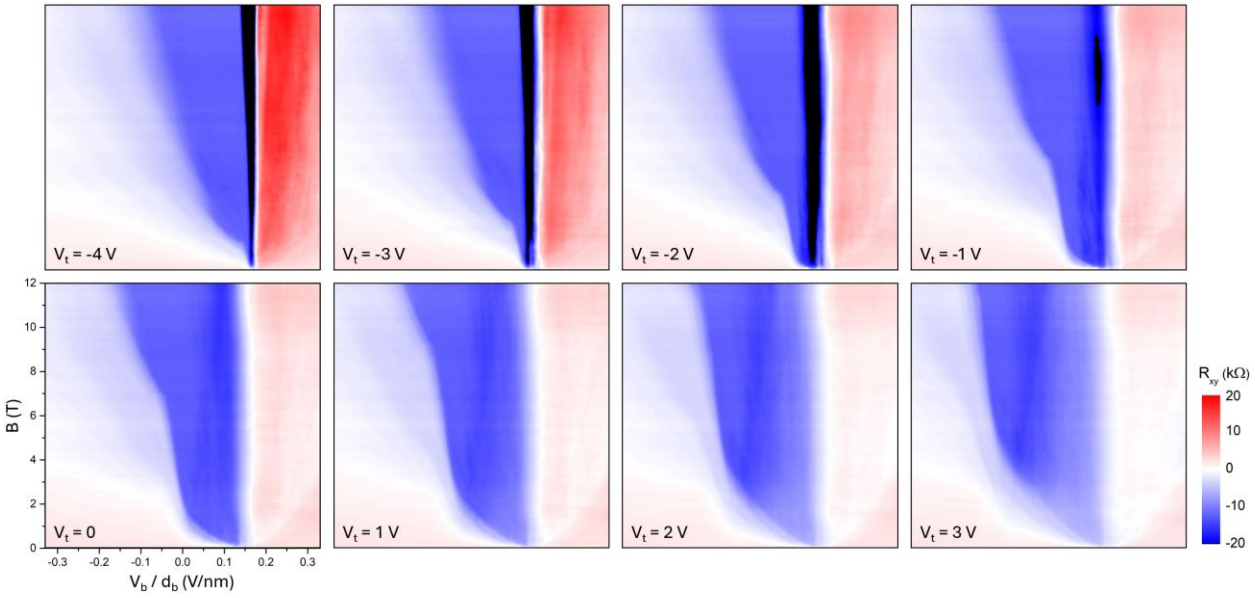

Figure 2.24: Landau fan diagrams for an etched device with varying top gate voltage. The incompressible region of WTe_2 grows with gate. This can in principle be used to calculate the WTe_2 gap, but it relies on multiple free parameters. A better method for determining the size of the gap is presented in Section 2.5. All plots have the same axes and color scales. ($T = 1.5$ K)

2.3.4 *Contour Interpolation*

The magnetic field response of graphene can also be used to extract the individual carrier densities of the materials everywhere in the accessible gate range. This is not a trivial fact, as only the sum density $n_{tot} = n_g + n_w$ can be inferred from the gate voltages alone—the exact split of carriers requires additional information. Fortunately, we have contours of known, constant graphene density in the form of Landau levels. Interpolating between them gives a full map of n_g over the gate space. From there, it is simple to calculate the WTe_2 density via $n_w = n_{tot} - n_g$. While this process is straightforward to describe at a high level, there are many details regarding the calculation and interpolation of the graphene contours worth discussing. To begin, we choose a 2D gate map at an intermediate magnetic field strength, $B = 4$ T. Here the magnetic field is strong enough to create easily resolvable Landau levels in the graphene, but it is still weak enough that

many Landau levels are visible in the gate range. Peaks in the data are identified programmatically and interpolated into rough polylines. For higher index Landau levels where only part of the contour is visible, the next lowest index contour is copied over to fill in the missing regions. This is a valid approximation as all contours have approximately the same shape, particularly at higher indices and on the WTe_2 electron side. These are adapted into splines which are then manually refined to fit the data as accurately as possible. More points are then interpolated between these knots in order to increase the fidelity of subsequent interpolations between splines.

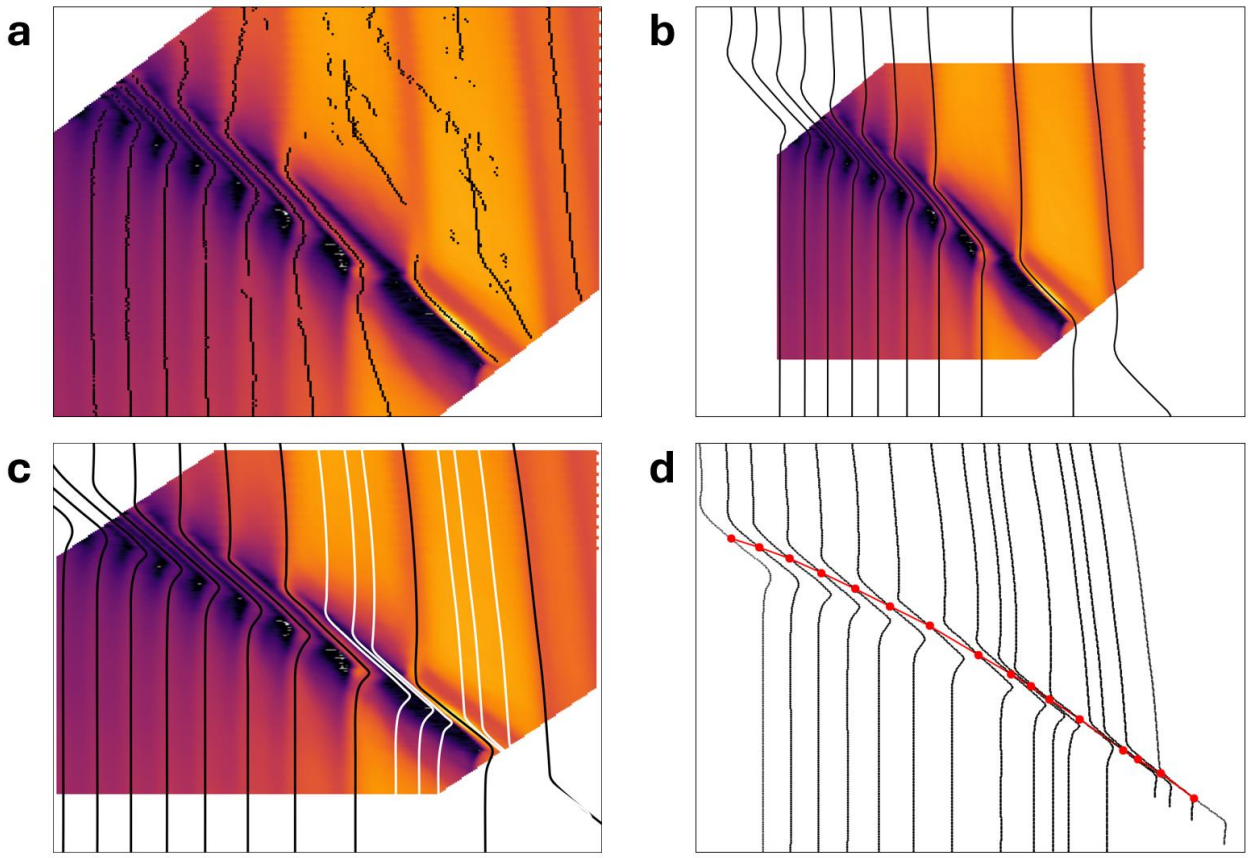

Figure 2.25: The contour interpolation process. (a) The initial peak mapping algorithm fits most features well but others are lacking and require manual adjustments. (b) The initial splines formed from the points in (a) with additional linear patches. (c) The manually refined splines including data for $B = 0.5$, 1, and 2 T (white). These additional splines fill in the large gap between $N = 0$ and $N = \pm 1$. (d) The centers of the WTe_2 gaps are used as the interpolation points (red).

We then employ a linear interpolation between the splines. Though not strictly accurate, it is a sufficiently close approximation given our data granularity everywhere except for the region between the $N = 0$ and $N = \pm 1$ Landau levels. For this region, we fit splines to the $N = \pm 1$ Landau levels at lower magnetic fields, $B = 0.5$ T, 1 T, and 2 T. Since the graphene carrier density within a Landau level with index N is given by $n_g = \frac{4NeB}{h}$, it is possible to relate these lower field contours to the $B = 4$ T data. Splines are then interpolated between the centers of the WTe_2 gaps. This approach works well in the regions where the contours are approximately vertical, but within the gapped region of WTe_2 where the contours are diagonal, many interpolated points map to the same bin—a discrete region with finite size in our gate space. As such, we must average the value of the interpolated points that map to a given bin. The end result is a map of n_g everywhere in the gate space from which we calculate n_w via $n_w = n_{tot} - n_g$.

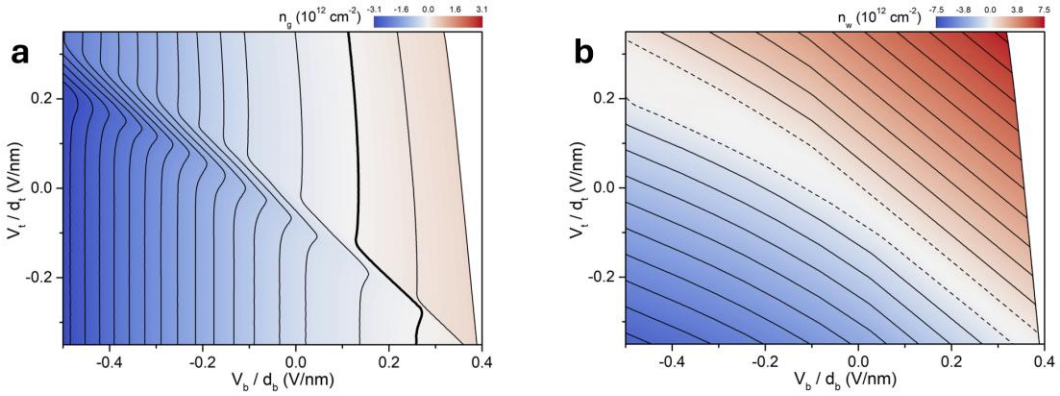

Figure 2.26: Extracted carrier densities in graphene and WTe_2. (a) n_g map with equally spaced (2×10^{11} cm^{-2}) contours. The thick contour indicates the Dirac point $n_g = 0$. (b) n_w map with equally (7×10^{11} cm^{-2}) spaced contours. The dashed lines correspond to $n_w = \pm 2 \times 10^{11}$ cm^{-2}. Below this density, the contours become unstable from numerical fluctuations.

The density maps of Figure 2.26 accurately reproduce the features seen in the 2D gate maps of Figure 2.19. We see that the curved feature we associated with $n_w = 0$ is indeed the contour of

WTe_2 neutrality. It is tempting to associate the width of this window to the WTe_2 gap, but such analysis is potentially misleading. Instead, we use another technique to quantify the gap in Section 2.5. We see sharp zig-zag contours of constant density in the graphene. The lower region of the contours is almost perfectly vertical, while the upper region is nearly straight with a slight tilt. This is consistent with the compressibility measurements of pure monolayer WTe_2 reproduced in Figure 2.23 which show a diverging density of states (nearly infinite compressibility) at the valence band edge and a high but finite density of states at the conduction band edge. This results in perfect screening on the hole side and large but finite screening on the electron side. The slope of the graphene contours in regions where the WTe_2 is conductive reflects the ratio of densities of states between the two materials. In fact, we can quantify this density of states, as we shall now see.

2.4 Transport Analysis

Equipped with our maps of n_g and n_w, it is possible to make quantitative statements about the graphene-WTe_2 hybrid. For example, we can simply read off the intrinsic charge transfer from our inferred values of n_g and n_w at zero gating. Doing so gives a value of 1.3×10^{11} cm^{-2}, well below the critical density for superconductivity in bare WTe_2. [37] It is also possible to extract other parameters including the interlayer charge separation and WTe_2 conduction band density of states. We find that the WTe_2 is largely unaffected by the presence of graphene, but there are still some open questions about the hybrid system that remain to be answered.

2.4.1 *Band Alignment Model Revisited*

We have already introduced the band alignment model in Section 2.3.2, and we will now expand upon it. Specifically, let us consider the electron energy as a function of position in the device. The gates create electric fields that change the electron energy, $-e\phi$. For a monolayer sample, this is

the only concern. However, since a charge imbalance can exist between the layers of the hybrid, we must also consider its associated potential drop. This effect is illustrated in Figure 2.27 for two points with the same graphene density but different WTe_2 densities. At point A, the WTe_2 is gapped, and the electric field only changes at the graphene layer. However, at point B, both layers have charge, resulting in three distinct electric fields in different parts of the device. The differences can be dramatic, even inverting the sign of the electric field between layers relative to those created by the gates. This analysis also reveals the presence of another parameter of importance, the interlayer charge separation d. We will discuss next how to calculate its value.

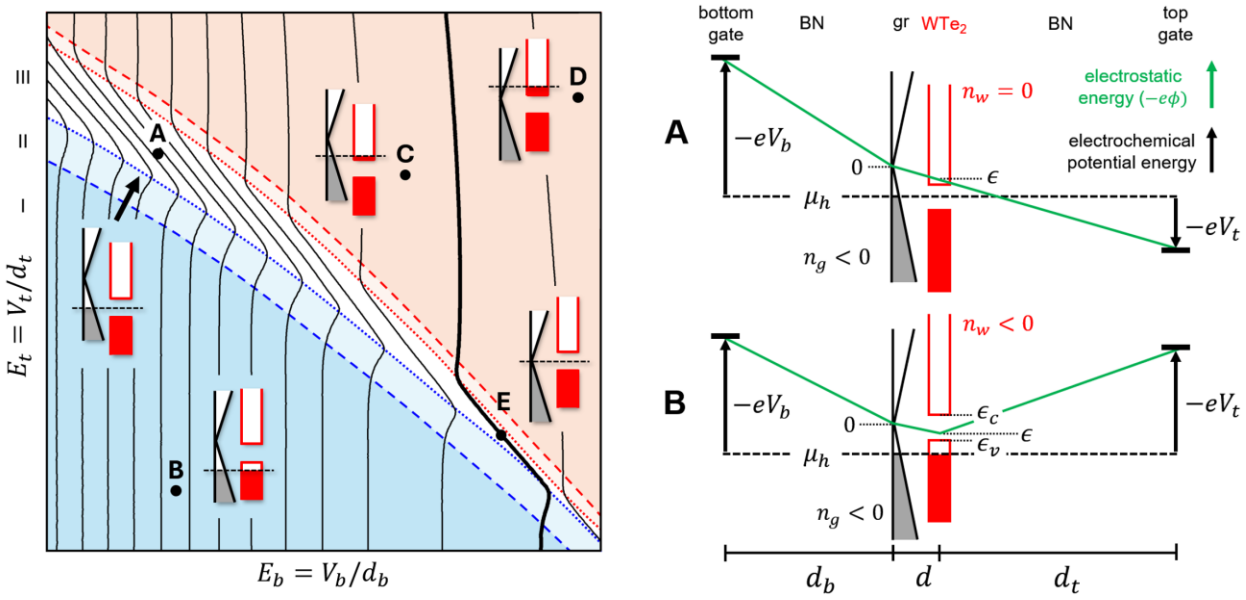

Figure 2.27: Refined band alignment model with electrostatic energy. The plot on the left shows extracted graphene contours and WTe_2 doping type by color. Distinct regions are identified and associated with the regions seen in the Landau fan in Figure 2.21. As in the Landau fan, region II is significantly wider on the hole side (blue) than the electron side (red). On the right, we plot the electrostatic energy (green) and electrochemical potential energy (black) as a function of position in the stack for points A and B. The charge difference between the graphene and WTe_2 alters the electric field between the layers. The diagram is to scale vertically with allowance made to increase the width of d for viewing clarity.

2.4.2 *Interlayer Charge Separation*

We know the charge transfer between layers, and we can also recover the separation of that charge, d. This quantity will be integral for subsequent calculations, but it is not trivial to calculate. In order to quantify d from the density maps, we must first consider the action of the gate in the p-p region of the gate space (near point B in Figure 2.27). We have already discussed how the verticality of the graphene contours in this region implies perfect screening and a diverging density of states in the WTe_2. As such, we can treat the chemical potential of the WTe_2 as being pinned at the valence band edge. Let us now consider the effect of varying the bottom gate in this regime. Since the bottom gate faces the graphene and the chemical potential is fixed in the WTe_2, the gate acts like a lever arm, shifting the chemical potential in the graphene by an amount

$$\Delta\mu_g = e\,\Delta V_b \left(\frac{d}{d+d_b}\right)$$

This is a useful quantity, as it relates to the graphene density of states via $D_g(\mu) = \frac{dn_g}{d\mu_g}$. Substituting in the above expression for $\Delta\mu_g$ in the limit of small changes allows us to solve for d:

$$\frac{dn_g}{d\mu_g} = \frac{2|\mu_g|}{\pi\hbar^2 v_F^2} \Rightarrow \frac{dn_g}{dV_b} = \frac{2|\mu_g|}{\pi\hbar^2 v_F^2}\left(\frac{ed}{d+d_b}\right)$$

$$d = \frac{\pi\frac{dn_g}{dV_b}\hbar^2 v_F^2 d_b}{2e|\mu_g| - \pi\frac{dn_g}{dV_b}\hbar^2 v_F^2} = \left[\frac{\pi\frac{dn_g}{dV_b}\hbar v_F}{2e\sqrt{\pi|n_g - n_0|} - \pi\frac{dn_g}{dV_b}\hbar v_F}\right] d_b$$

In the final line, we have made the substitution $|\mu_g| = \hbar v_F\sqrt{\pi|n_g - n_0|}$ where n_0 is the initial doping of the graphene, found to be 1.3×10^{11} cm^{-2} at the start of this section. We will discuss the calculation of the graphene Fermi velocity in Section 2.5.2, but for now we will just use its determined value, $v_F = 1.01 \times 10^6$ m/s. This value is consistent with other reports. [29]

The remaining parameter to find is $\frac{dn_g}{dV_b}$, the change in graphene doping with respect to bottom gate voltage. This is not a universal parameter, as its value varies greatly depending on where in the gate space it is measured. As such, we will limit ourselves to maximally negative top gate voltage over a range of negative bottom gate voltages (the bottom left corner of the gate space). We perform a linear regression on the extracted graphene density values n_g vs. bottom gate voltage along this line cut, the slope of which gives $\frac{dn_g}{dV_b}$.

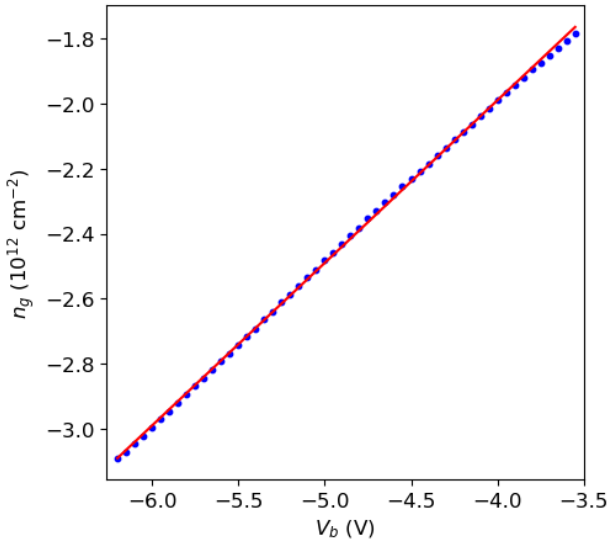

Figure 2.28: Linear regression of graphene density n_g vs. bottom gate voltage V_b. The slope is 0.50×10^{12} cm^{-2} V^{-1} with an R^2 value of 0.9997. The selected voltage range is $V_t = -6.5$ V and $-6.2 \leq V_b \leq -3.5$. This corresponds to approximately -0.50 to -0.28 V/nm in Figure 2.14.

Plugging the calculated value of $\frac{dn_g}{dV_b} = 0.50 \times 10^{12}$ cm^{-2} V^{-1} gives $d = 0.24$ nm, comparable to the thickness of a graphene monolayer (~0.3 nm).

2.4.3 *WTe_2 Density of States*

Now that we have determined the charge separation d, we can calculate the WTe_2 density of states. Recall that to calculate d, we used a fixed point in energy for the WTe_2 (the Fermi energy pinned

at the valence band edge) and considered the action of the gate as a kind of lever arm, shifting the electrostatic energy of the graphene proportional to the ratio $\frac{d}{d+d_b}$. We can perform a similar trick by considering a resolvable feature of the graphene, its Dirac point. When the graphene is neutral, we know that the electric field between the bottom gate and graphene must equal the electric field between the graphene and WTe_2 by Gauss's law. Let us now consider the effect of a small change in bottom gate voltage ΔV_b. The graphene remains approximately neutral, but the electrostatic energy of the WTe_2 changes by an amount proportional to the ratio $\frac{d}{d_b}$. By remaining neutral, the graphene acts like the fulcrum of a lever that connects the bottom gate and WTe_2 potentials. As such, the change in chemical potential $\Delta\mu_w$ is given by

$$\Delta\mu_w = e\,\Delta V_b\left(\frac{d}{d_b}\right)$$

We have already seen that in the zero temperature limit, the density of states is $D(\mu) = \frac{dn}{d\mu}$. We can express the change in carrier density as $\Delta n_w = C_t\Delta V_t + C_b\Delta V_b \approx C_t\Delta V_t$ since we have already made the approximation that the change in back gate is sufficiently small as to not tune n_g. Thus

$$D_w = \frac{\Delta n_w}{\Delta\mu_w} \approx \frac{\varepsilon_0\varepsilon_{BN}}{e^2}\left(\frac{d_b}{dd_t}\right)\left(\frac{\Delta V_t}{\Delta V_b}\right)$$

The slope of the graphene Dirac point on the conduction band side of the WTe_2 in our 2D gate maps can be used in conjunction with d to recover the approximate WTe_2 density of states. Unfortunately, the slope is not consistent along the entirety of the Dirac point, affecting the calculation. Including the full range of the Dirac point gives $D_w = 8.5 \times 10^{11}$ cm^{-2} meV^{-1}, while considering only the upper half of points gives $D_w = 5.7 \times 10^{11}$ cm^{-2} meV^{-1}. There is considerable uncertainty in each of these values depending on the exact coordinates chosen, and we have made several coarse approximations to get this far, so these values should be treated as approximate

only. As such, we will report a value of 7.1×10^{11} cm^{-2} meV^{-1} with the understanding that the uncertainty is substantial. Comparing to existing studies of WTe_2, remote sensor measurements report a value of 3.7×10^{11} cm^{-2} meV^{-1} [31] while calculations utilizing the superconducting coherence length give a value of $\sim 8 \times 10^{11}$ cm^{-2} meV^{-1}. [37] The large spread of calculated D_w values can likely be attributed to a combination of methodology and sample quality. We have already seen in Figure 2.3f how improvements in crystal quality can dramatically change the superconducting parameters of WTe_2, so it stands to reason that the experimentally inferred density of states should be similarly sensitive. It is worth noting that the hybrid device we have been analyzing was made with the same WTe_2 crystals that gave the value $D_w \approx 8 \times 10^{11}$ cm^{-2} meV^{-1}.

2.4.4 *Open Questions*

While we have demonstrated our ability to recover various physical parameters from the graphene-WTe_2 hybrid and shown that they are consistent with the known properties of the constituent materials, some questions still remain. One of the most perplexing relates to the apparent dielectric constant of the BN gate dielectrics. We will discuss hexagonal boron nitride in greater detail in Chapter 3, but for now we will focus specifically on its relative dielectric constant, ε_{BN}. This is a well-studied and important parameter that is required to convert gate voltages to carrier density. While its reported value depends somewhat on the measurement technique, most sources agree that for BN nanosheets, ε_{BN} lies between 3 and 4 [66] with no sources reporting values below 3. However, when converting gate voltages to carrier density to fit the Landau levels, we require a value of $\varepsilon_{BN} = 2.07$ in order to do the fitting. This value is considerably lower than any reported in transport literature despite many graphene devices determining values for ε_{BN} as part of their analyses. Moreover, the value of $\varepsilon_{BN} \approx 2$ is consistently seen across hybrid devices, suggesting that it is an intrinsic property of the graphene-WTe_2 hybrid system.

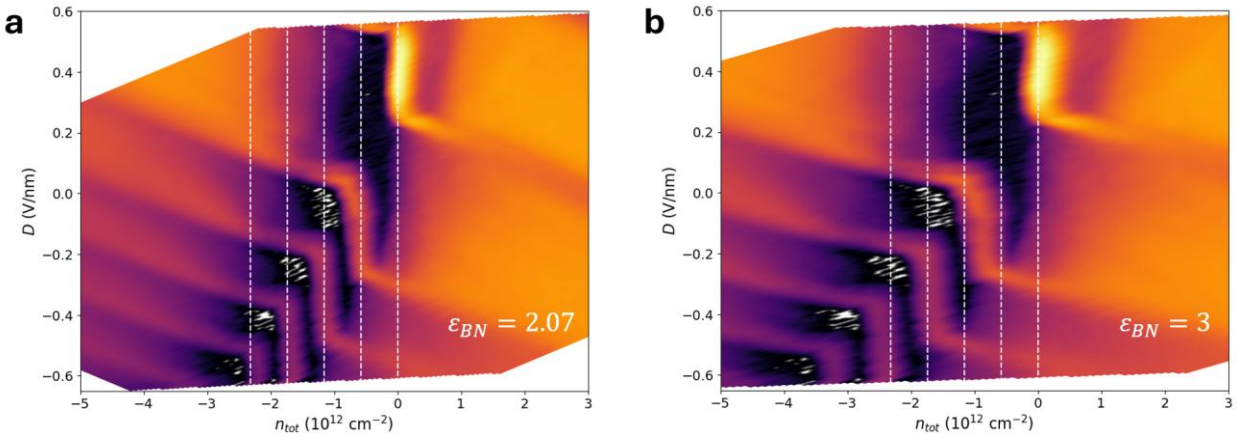

Figure 2.29: Landau levels with different dielectric constants. Both plots show the same data ($B = 6$ T, $T = 1.5$ K) converted to n-D coordinates using (a) $\varepsilon_{BN} = 2.07$ and (b) $\varepsilon = 3$. The white dashed lines correspond to the densities associated with the $N = 0$ through $N = -4$ Landau levels. Only $\varepsilon_{BN} = 2.07$ is consistent with the data; $\varepsilon_{BN} = 3$ cannot be made to agree.

It is unlikely that this low of a dielectric constant is a result of random chance, particularly given its consistency between devices. Since the dielectric constant relates gate voltage to induced carrier density via $n \propto \varepsilon_{BN} V$, if the actual dielectric constant of the BN is indeed 3, then that would suggest that only two thirds of the charge is present in the graphene transport even when the WTe_2 is gapped. While other properties of the hybrid align well with those of intrinsic monolayer graphene in this regime, we can still consider the possibility that some of the charges are not contributing to transport. We would need to invoke an external mechanism that localizes excess charge in the graphene without affecting its apparent Fermi velocity or Landau quantization. It is conceivable in the abstract that many body correlations from the WTe_2 are somehow localizing the charge. Though given the ambiguity about the method of charge localization in intrinsic monolayer WTe_2, it is difficult to make any prescriptive statements about the hybrid.

Another peculiar feature of the hybrid transport is the apparent absence of superconductivity. Assuming the hybridized WTe_2 behaves similarly to intrinsic monolayer WTe_2,

we should see superconductivity at densities above 5×10^{12} cm^{-2} and temperatures below 1 K. However, I have measured multiple hybrid devices at dilution temperatures (~10 mK) and have seen no evidence of it. Interpreting this absence is difficult, as it is impossible to rule out several trivial explanations. For example, it is known that superconductivity in monolayer WTe_2 is inconsistent, with many devices made from ostensibly high-quality crystals not superconducting. It is difficult to imagine graphene disrupting the superconductivity in WTe_2, suggesting that the devices measured would not have superconducted even in the absence of graphene. Ideally, we would measure superconductivity in a device that has WTe_2 only partially covered by graphene which would allow us to definitively determine what effects if any graphene has on the state.

Finally, it is worth mentioning that the hybrid system has strange magnetotransport character near the graphene Dirac point. The behavior is non-monotonic, inconsistent with weak (anti)localization, and highly sensitive to gate voltages. Further work is needed to explore and explain this magnetic field response, particularly given graphene's weak magnetic coupling.

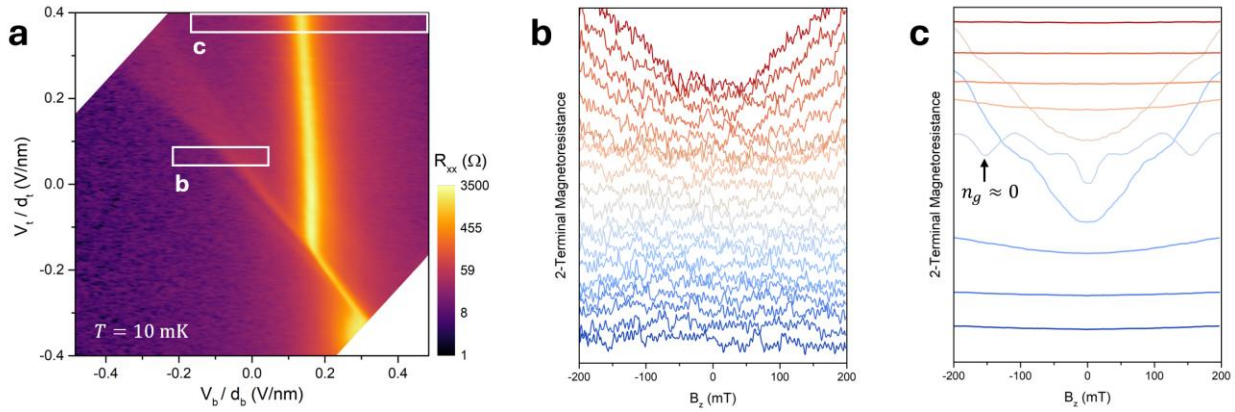

Figure 2.30: Hybrid magnetotransport. (a) 2D gate map showing resistance R_{xx}. There is no sign of superconductivity in the hybrid. ($T = 10$ mK) Cuts used for magnetotransport are shown. (b) Waterfall plot of magnetoresistance across the WTe_2 neutrality point. Blue to red corresponds to left to right in (a). There are no discernable features beyond a slight curvature near the Dirac point. (c) Magnetoresistance across the graphene Dirac point. The response becomes pronounced very near the Dirac point. When $n_g \approx 0$, the behavior is non-monotonic with field.

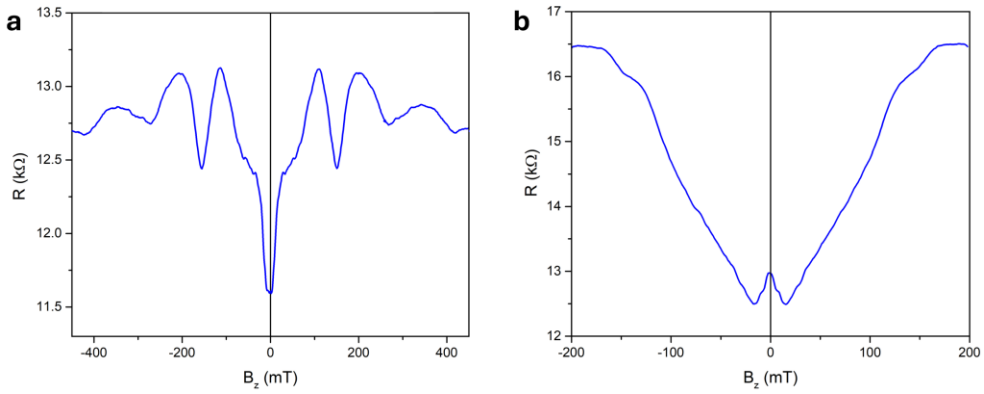

Figure 2.31: Two-terminal magnetoresistance near the Dirac point. Both datasets were taken at $T = 100$ mK. (a) A point at the uppermost region of the gate space for maximal top gate. (b) A point at intermediate positive top gate. Both curves are extremely sensitive to gate voltage.

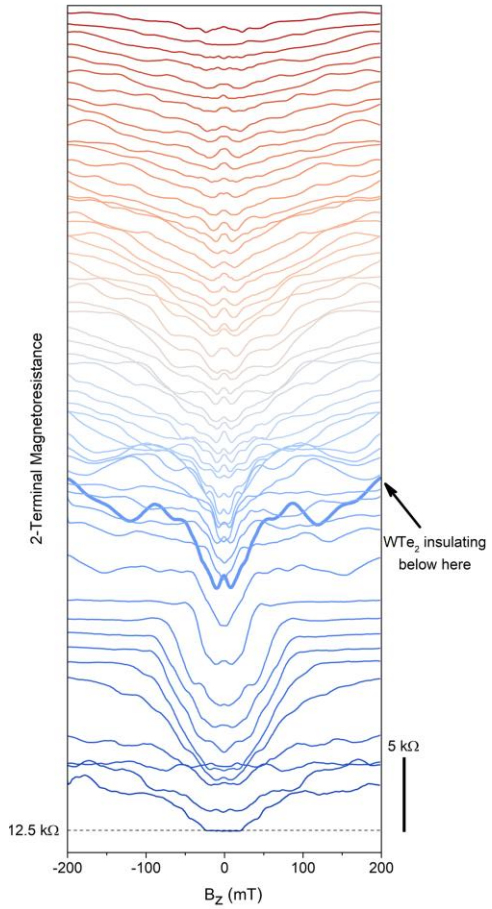

Figure 2.32: Waterfall plot of two-terminal magnetoresistance along the Dirac point. Red to blue is positive to negative V_t (proxy for WTe_2 density). A quantum spin Hall plateau may emerge at the valence band edge (bottommost trace), but we are limited by our gate range. ($T = 100$ mK)

2.5 COMPRESSIBILITY MEASUREMENTS

In addition to transport, I have also performed a type of remote compressibility measurement that is capable of inferring the chemical potential of the hybrid. This work follows the precedent of prior studies by using a remote monolayer graphene sensor to indirectly infer chemical potential. Doing so allows us to calculate the graphene Fermi velocity and WTe_2 gap at various dopings. The hybrid also shows negative compressibility near the WTe_2 valence band edge, indicating that electron-electron correlations play a significant role in its behavior.

2.5.1 *Remote Sensing with Graphene*

The technique we will develop in this section is a remote sensing method, meaning that it uses a sensor (monolayer graphene) that is physically separated from the sample in order to infer its properties. This method has been utilized previously to characterize both graphene [67][68] and monolayer WTe_2. [31] However, the measurement is complicated to describe and execute, all the more so for a hybrid system. The core operating principle relies on the use of monolayer graphene specifically as the sensor. As we have seen, graphene has only one resistive feature in its spectrum, the Dirac point. In transport, the graphene Dirac point is sharp, easily resolvable, and unambiguously indicates when the graphene is charge neutral. Gauss's law tells us that a 2D sheet with charge density n satisfies $n = \varepsilon_r \varepsilon_0 (E_1 - E_2)$ where E_1 and E_2 are the electric fields on either side of the sheet. Put another way, when the sheet is charge neutral, the electric fields are equal on either side. This is intuitive, and we have already seen this result used in Figure 2.27.

It follows that whenever the sensor is maximally resistive (at its Dirac point), we know the electric field between the sample and sensor must equal the field between the sensor and the gate facing it. We can obtain the latter easily from the voltage applied to the gate, which we will call the sensor gate voltage V_s. It is important that we distinguish between voltage V, which is an

electrochemical potential, and the electrostatic potential ϕ. Converting to energies, the two are related via $-eV = -e\phi + \mu$ where μ is the chemical potential. Since we are measuring the resistance of the graphene sensor to determine when it is neutral, let us take it to be our ground, the reference point of zero electrochemical potential energy ($-eV = 0$). We have freedom to choose the zero point for the electrostatic potential energy, so let us choose its zero to coincide with the hybrid graphene. Before proceeding further, we will look at the electrochemical potential and electrostatic energies as a function of position within our device, as this will be useful to reference for the subsequent analysis and calculations.

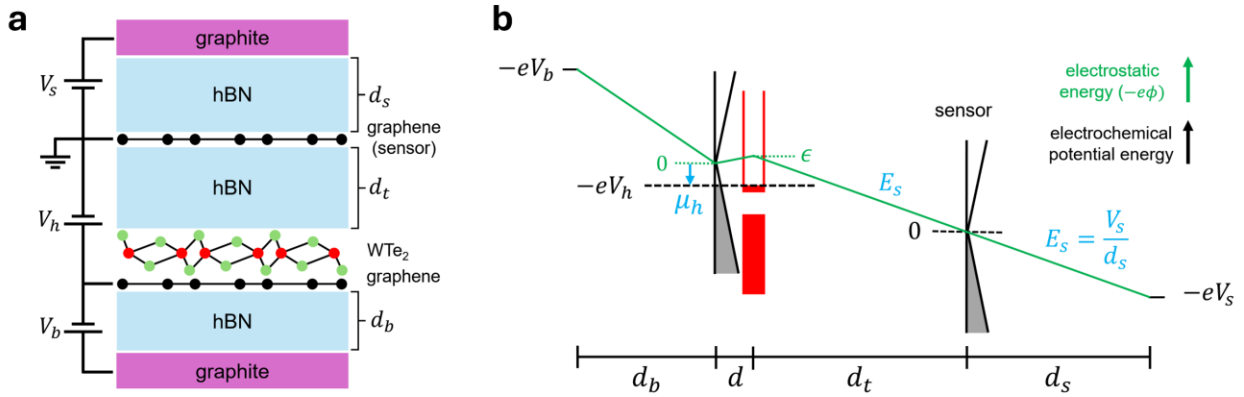

Figure 2.33: Schematic of a remote sensor measurement. (a) Side view device schematic with voltages labeled. Voltages are measured relative to the sensor, which is held at ground while measuring its two-terminal resistance. Gate voltages V_s and V_b tune the carrier densities of the layers, and V_h shifts the electrochemical potential of the hybrid. (b) Electrostatic energy (green) and electrochemical potential energy (black) as a function of position. The quantity of interest is $\mu_h + \epsilon$. The figure is drawn to scale in both position and energy with an exaggeration in the interlayer charge separation d for visual clarity.

A sensor measurement proceeds as follows. First, a voltage V_s is applied to the sensor gate. Next, the bottom gate voltage V_b is set. All contacts to the hybrid are shorted together to a voltage V_h. Two-terminal resistance is measured through the sensor while V_h is swept over a narrow range. The use of a two-terminal measurement allows us to sample the smallest possible area directly

above the hybrid material. By grounding adjacent contacts, current can be forced to flow over a narrow (~5 μm) channel that is entirely aligned with the hybrid. This is critical as it prevents the sensor from responding to external fields and improves the fidelity of the measurement. For each voltage pair (V_s, V_b), we find the value of V_h that maximizes the sensor resistance. We apply a quadratic fit to the data near the maximum measured resistance to improve accuracy.

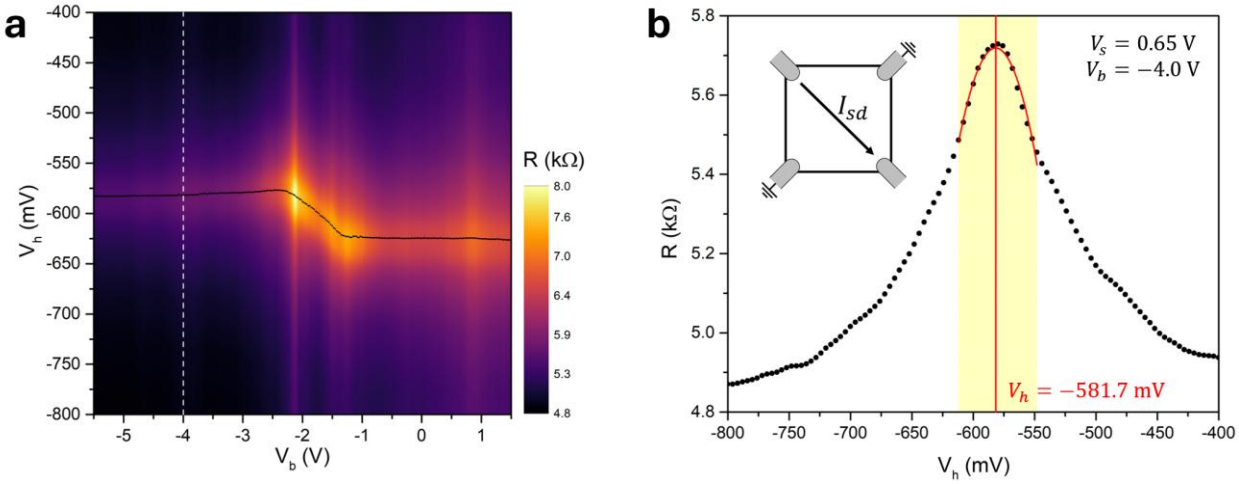

Figure 2.34: A single sensor measurement. (a) 2D gate map of the two-terminal sensor resistance as a function of bottom gate voltage V_b and hybrid voltage V_h. ($V_s = 0.65$ V, $T = 1.5$ K) The determined coordinates of maximum resistance are shown in black. (b) Line cut of sensor resistance for $V_b = -4$ V. The inset shows the measurement geometry for the sensor. A quadratic fit (red) is performed over the yellow region to find the value of V_h that maximizes the resistance.

When the sensor is neutral, the electric field $E_s = V_s/d_s$ penetrates it, changing the electrostatic potential energy of the WTe_2 by an amount $-eE_s d_t$. Let us take ϵ to be the electrostatic potential energy of the WTe_2 relative to the hybrid graphene. Returning to our definition of voltage, we now consider the electrochemical potential energy difference between the hybrid and sensor: $-e\Delta V = -e\Delta\phi + \Delta\mu$. Since the sensor is grounded, $\Delta V = V_h$, so the left hand side of the equation becomes $-eV_h$. The hybrid graphene is taken to have $\phi = 0$, so $-e\Delta\phi = \epsilon + eE_s d_t$. Since the sensor is at its Dirac point, we take its chemical potential to be zero. Therefore $\Delta\mu = \mu_h$, where μ_h is the

chemical potential of the hybrid such that $\mu_h = 0$ corresponds to the hybrid graphene Dirac point. Putting this all together, we find

$$\mu_h + \epsilon = -e\left[V_h + V_s\left(\frac{d_t}{d_s}\right)\right]$$

2.5.2 *Hybrid Graphene Fermi Velocity*

In short, by tuning the gate and hybrid voltages V_s, V_b, and V_h such that the sensor is maximally resistive, we can recover the quantity $\mu_h + \epsilon$. (The energy offset between layers ϵ initially seems problematic, but since we are most interested in the hybrid behavior when the WTe_2 is gapped, this term will not be important.) However, the derivation was far from straightforward, and it is good practice to interrogate the validity and efficacy of the measurement technique. One useful check is to see if we are capable of determining the Fermi velocity of the hybrid graphene. Graphene's Fermi velocity is well known to be approximately 10^6 m/s. [29] When the WTe_2 is gapped, it should have no effect on this value. In the WTe_2 gap, ϵ can be ignored and μ_h reduces to the hybrid graphene μ_g. Similarly, since the sensor is electrically transparent when it is neutral, both V_s and V_b tune the hybrid graphene's carrier density n_g. Recall for graphene that the chemical potential is related to both the carrier density and Fermi velocity v_F by

$$\mu_g = \hbar v_F \sqrt{\pi |n_g - n_0|}\ \mathrm{sgn}(n_g - n_0) \implies \frac{d\mu_g}{dn_g} = \frac{\hbar v_F \sqrt{\pi}}{2\sqrt{|n_g - n_0|}}$$

Therefore, we can recover both the Fermi velocity and the initial graphene doping n_0 from the slope of our sensor measurements $\frac{d\mu_g}{dn_g}$ when the WTe_2 is in its gap. We will look at some traces of $\mu_h + \epsilon$ in detail in Section 2.5.3, but for now we will just comment that $\frac{d\mu_g}{dn_g}$ is very straight in this region (see Figure 2.37), and a simple linear regression can find the slopes.

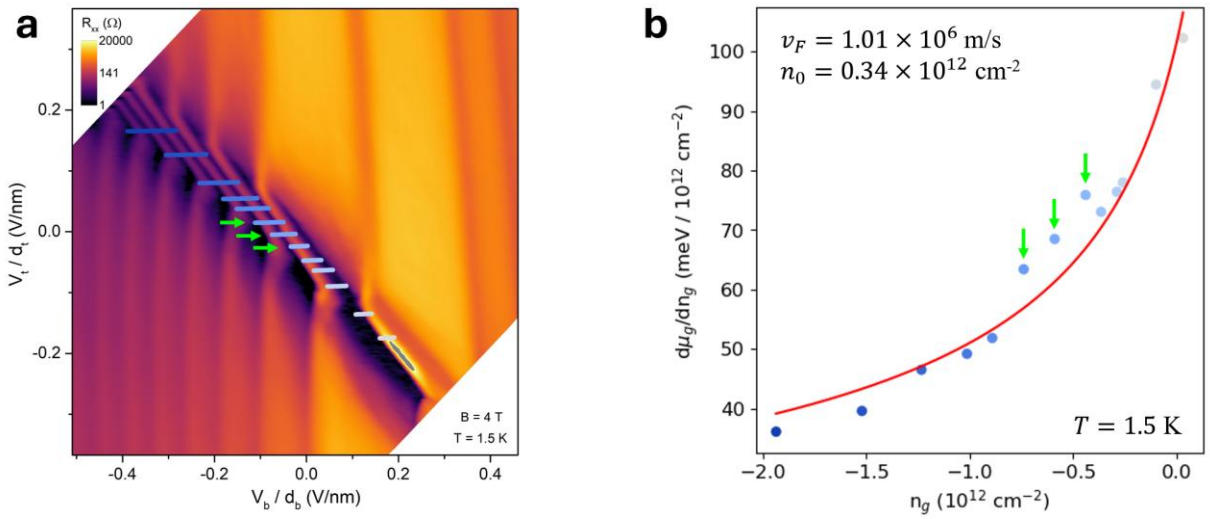

Figure 2.35: Hybrid graphene Fermi velocity calculation. (a) 2D gate map at $B = 4$ T with the effective gate voltages of the sensor measurements indicated. Regions of linear $\frac{d\mu_g}{dn_g}$ align well with the gaps seen in the hybrid transport. (b) Plot of $\frac{d\mu_g}{dn_g}$ vs. n_g used to calculate the Fermi velocity. The curve of best fit is shown in red. The points indicated with the green arrows are not included in the fit, as the negative compressibility is exceedingly strong there.

To plot the coordinates of the sensor neutrality in our original 2D gate space, we must compute the "effective" gate voltages, i.e. the voltages of the gates relative to the hybrid. This is done by converting $V_b' = V_b - V_h$ and $V_t' = \left(\frac{V_s - V_h}{d_s + d_t}\right) d_t$ where the primed values are the equivalent gate voltages the hybrid would have seen if the sensor were used as a gate as it was in Section 2.3. We see excellent agreement for the location of the WTe_2 gap between the sensor and hybrid transport measurements. Fitting the slopes to extract the Fermi velocity gives a value of 1.01×10^6 m/s, entirely consistent with the accepted value. The calculated intrinsic doping of the graphene $n_0 = 3.4 \times 10^{11}$ cm^{-2} is positive, suggesting an intrinsic n-type doping. This is consistent with the n-type doping observed from the graphene Landau fan in Figure 2.21 for which the projected intrinsic doping was $n_0 = 1.8 \times 10^{11}$ cm^{-2}. (These values should not be confused

for the doping of the graphene in the hybrid at zero gating!) Finally, we note that three of the points indicated with green arrows are significant outliers. These points all occur near zero net gating, and as we will see in Section 2.5.3, they correspond to the traces with the strongest negative compressibility. Possible connections between these facts are murky, but even if we do include these points in our fit, the Fermi velocity only changes slightly to $v_F = 1.07 \times 10^{12}$ cm^{-2}.

2.5.3 *Chemical Potential and Negative Compressibility*

Before proceeding further, I will formally introduce electronic compressibility. We have already alluded to the concept of incompressibility when discussing the gap of WTe_2, a state that can accept no charges. The electronic compressibility of a system κ is defined as $\kappa \equiv \frac{1}{n^2}\frac{dn}{d\mu}$ in analogy to the isothermal compressibility of a gas, $-\frac{1}{V}\frac{dV}{dP}\Big|_{T,N}$. [4] It will also be useful for us to consider the inverse compressibility $\kappa^{-1} = n^2\frac{d\mu}{dn}$. Recall as well that at zero temperature, the density of states is given by $D(\mu) = \frac{dn}{d\mu}$. As such, the inverse compressibility is a proxy for the inverse density of states: a low value of inverse compressibility indicates a system that can easily accept charge since the chemical potential doesn't change much with density. On the other hand, a large value for the inverse compressibility implies an incompressible state—a state where it costs significant energy to add more charges to the system. We have encountered the quantity $\frac{d\mu}{dn}$ when computing the graphene Fermi velocity. At the time, we only considered $\frac{d\mu_g}{dn_g}$, the inverse compressibility (up to a factor of n^2) of the graphene. Let us now consider the general shape of $\frac{d\mu}{dn}$ for the hybrid material, starting with zero sensor gating.

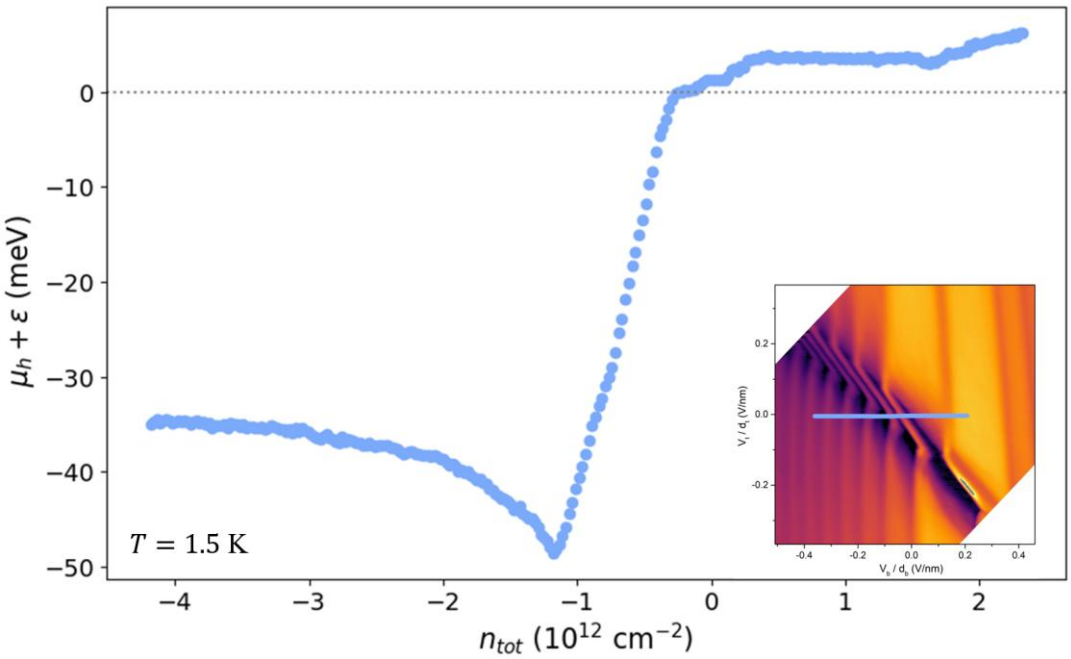

Figure 2.36: Hybrid chemical potential vs. total doping. The inset shows the equivalent location in the gate space the cut is taken over. The WTe_2 gap is clear where the chemical potential is rapidly changing. There is also a pronounced negative compressibility dip. The zero point is freely chosen to coincide with the WTe_2 conduction band edge to make reading gap sizes easier.

From the plot of $\mu_h + \epsilon$ vs. total hybrid density n_{tot}, two things are readily apparent. First, there is a region where the chemical potential changes rapidly with density that we can associate with the WTe_2 gap. In this region, the chemical potential and doping should reduce to those of the graphene, giving the finite slope $\frac{d\mu_g}{dn_g}$ used to calculate the Fermi velocity in Section 2.5.2. Second, there is a large dip in chemical potential for carrier densities below the gap. In this region, $\frac{d\mu}{dn} < 0$, so the electronic compressibility is negative. This is not possible for a non-interacting Fermi gas. Increasing the density forces the carriers into ever-higher energy states, implying $\frac{d\mu}{dn} > 0$. Stated another way, the single particle density of states cannot be negative. However, in the presence of electron-electron correlations, the balance between the correlation and kinetic energy of the carriers matters. The two can oppose each other, and if conditions are right, the system can end up

with negative electronic compressibility. [69] Negative compressibility has been observed in GaAs quantum wells as well as vdW systems like WSe_2. [69][70]

It is significant that we see the negative compressibility at the bottom of the WTe_2 gap, i.e. at the top of its valence band. As we have seen, the valence band edge is flat and is the source of significant electronic correlations in both bare WTe_2 and the graphene-WTe_2 hybrid. In fact, we can even identify this negative compressibility in the hybrid transport itself. Consider Figure 2.27 which shows contours of constant graphene density. Recall that region II was the transition region between gapped and conductive WTe_2 where the WTe_2 was both insulating and compressible. In region II on the hole side, we see that the contours have a positive slope, bending up and to the right. In the absence of screening, a contour of constant density in the graphene should have a slope of -1 on this 2D gate map (as seen in region III). When the WTe_2 is perfectly screening in region I, these contours are vertical. Partial screening should have some intermediate slope as is seen in the graphene Dirac point. The presence of a positive slope in region II indicates over-screening by the WTe_2—increasing the top gate voltage increases n_w, but we must also increase the bottom gate voltage to maintain constant n_g. In other words, we are adding electrons to both layers but maintaining a constant graphene carrier density. It is also worth mentioning that previous works did not observe negative compressibility in bare WTe_2. [31] It is unclear then if the negative compressibility we see is a result of improvements to crystal quality in the intervening years or an effect specifically related to the hybrid. We can speculate that the diverging density of states for holes at the valence band edge in the WTe_2 may be binding excess electrons from the graphene into excitons. This would explain the apparent over-screening seen in region II of transport measurements and may also shed light on the apparently low relative dielectric constant for BN. A proper theoretical treatment is definitely warranted in the future.

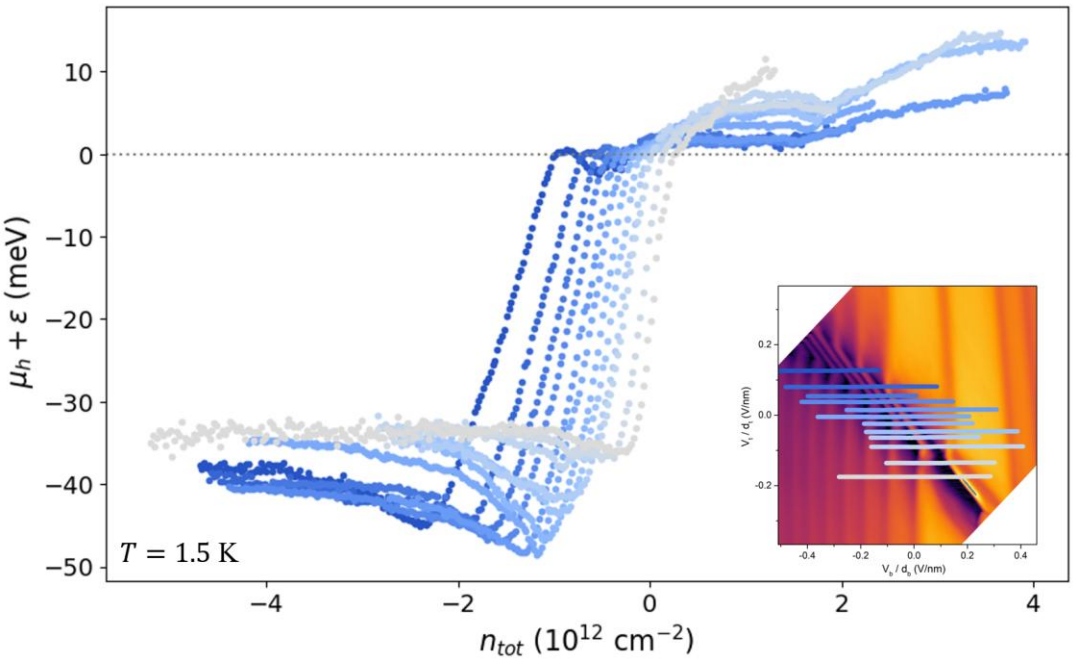

Figure 2.37: Hybrid chemical potentials vs. total hybrid doping across the gate space (inset). The negative compressibility is most pronounced near zero net gating. The size of the WTe_2 gap depends on where the gap bottom is defined as a result.

Looking at the full range of chemical potential traces, we see some degree of negative compressibility in all traces, but its strength evolves over the gate space. Specifically, it is strongest and sharpest at zero net gating (Figure 2.36) and weakest near the overall neutrality point of the system (the gray trace in Figure 2.37). The shape of the traces on the WTe_2 conduction band side, what we have chosen as $\mu_h + \epsilon > 0$, seems mostly consistent between traces. In principle, its slope can be used to recover the WTe_2 conduction band density of states, but the large fluctuations (results of measurement artifacts) and effects of ϵ make this an unlikely prospect. More qualitatively, the traces become flatter in this region as we move away from the overall neutrality point which is consistent with an increasing density of states in the materials away from neutrality. The traces become completely flat on the WTe_2 valence band side, seen most clearly in the trace that crosses the overall neutrality point. This is consistent with earlier compressibility

measurements of WTe_2 [31] and indicates the diverging density of states at the WTe_2 band edge. Even the trace through the overall neutrality point shows some negative compressibility, though it is less pronounced than what is seen in other traces. This suggests that the effect may be intrinsic to monolayer WTe_2 but is exaggerated by the presence of graphene. Further research is needed to definitively determine the origin and mechanism of this negative compressibility.

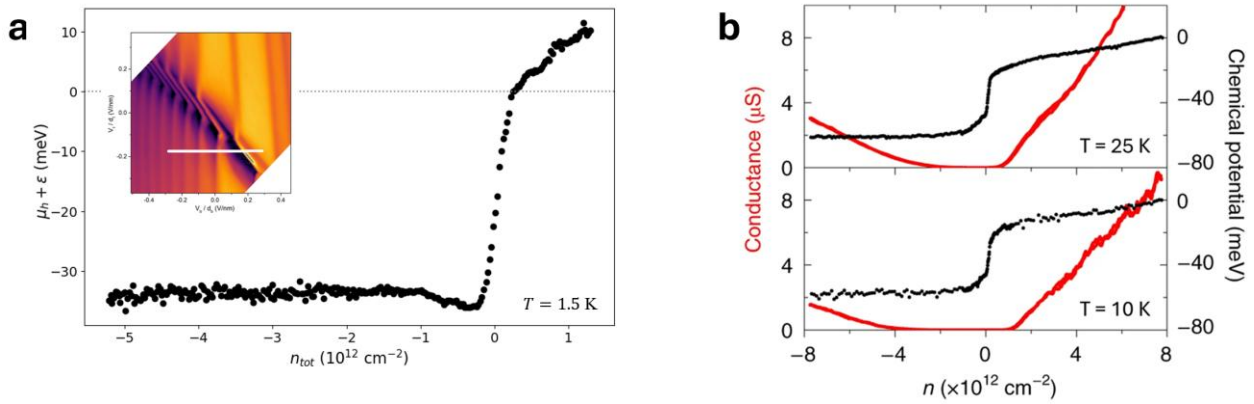

Figure 2.38: Comparing electronic compressibility. (a) The hybrid trace that goes through the overall neutrality point of the system (inset). A small amount of negative compressibility is visible. (b) Reproduced section of Fig. 3 of [31] showing the compressibility of bare WTe_2. There is no sign of negative compressibility, but the gap size is comparable to the hybrid measurements.

Quantifying the WTe_2 gap size requires us to make a choice in how we define the gap itself. The top of the gap is easy to identify, as the hybrid chemical potential stops rapidly changing at a clear point in all of the traces. The bottom of the gap is more ambiguous. If we choose to define the bottom of the WTe_2 gap as the bottom of the negative compressibility region, we are left with the uncomfortable conclusion that the gap changes by upwards of 30% across our gate space. This would contradict previous measurements of the bare WTe_2 gap from STM; Figure 2.7c shows that the bare WTe_2 gap is unaffected by the gate voltage. As such, it is sensible to define the bottom of the WTe_2 gap as the energy asymptotically approached on its valence band side. This method also quantitatively agrees with the slope $\frac{d\mu_g}{dn_g}$ predicted for graphene when the WTe_2 is gapped.

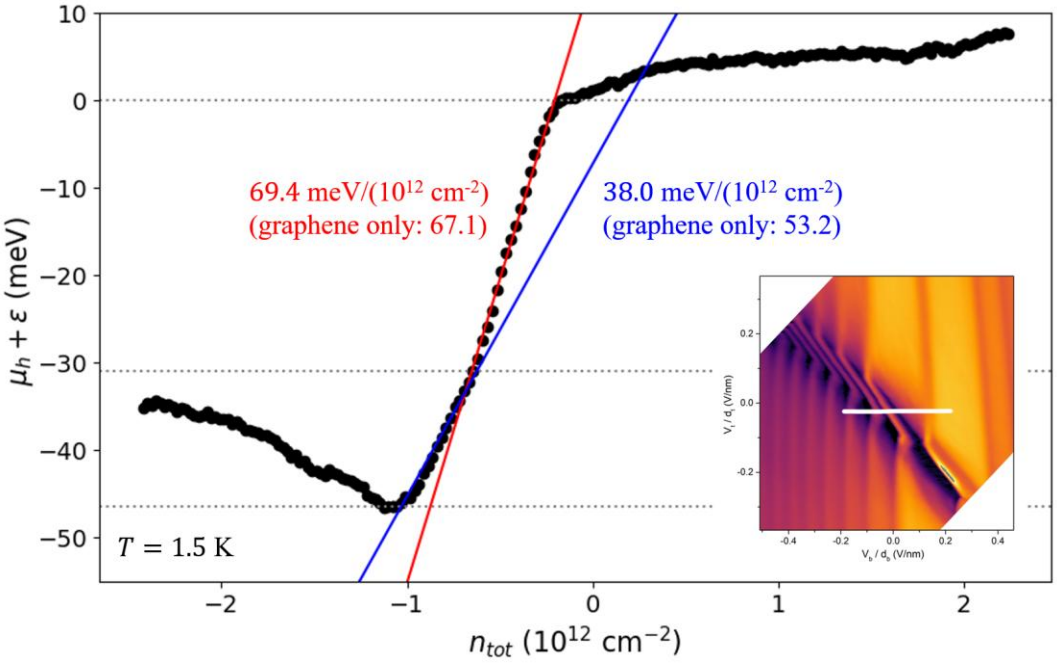

Figure 2.39: Change in slope within the negative compressibility region. This trace near zero gating (inset) has two distinct regions with different slopes indicated in red and blue. The gray dotted lines indicate the ranges over which the fits are done. The red fit agrees with the predicted value of $\frac{d\mu}{dn}$ for bare graphene, suggesting only this region is gapped. The resulting gap is 31 meV.

For traces near zero net gating where the negative compressibility is strongest, there is a faintly perceptible shift in the slope $\frac{d\mu}{dn}$ between the bottom of the negative compressibility and the energy asymptotically projected to on the WTe_2 valence band side. This is demonstrated most clearly in the chemical potential trace shown in Figure 2.39, but it can also be seen in transport in Figure 2.29 where the Landau levels deviate from verticality near the negative compressibility of region II. The chemical potential trace provides an opportunity to check which of these two slopes best matches the predicted value of $\frac{d\mu_g}{dn_g}$ for pure graphene. Calculating this value (see Section 2.5.1) gives slopes of 67.1 and 53.2 meV/(10^{12} cm^{-2}). Comparing to the data, the upper region (red fit in Figure 2.39) has a slope of 69.4 meV/(10^{12} cm^{-2}), a 3.4% difference from our prediction for pure graphene. However, the lower region (blue fit) has a slope of only 38 meV/(10^{12} cm^{-2}), a

28.5% difference. This implies that the lower region of the trace is not reflective of the behavior of pure graphene, so it should not be considered in the gap calculation. As such, we find the gap for this particular trace to be 31 meV. Repeating this procedure for the other traces gives a final value for the WTe_2 gap of 36.0 ± 3.8 meV. This value is consistent with the 40 meV gap reported in remote sensor measurements of bare WTe_2. [31]

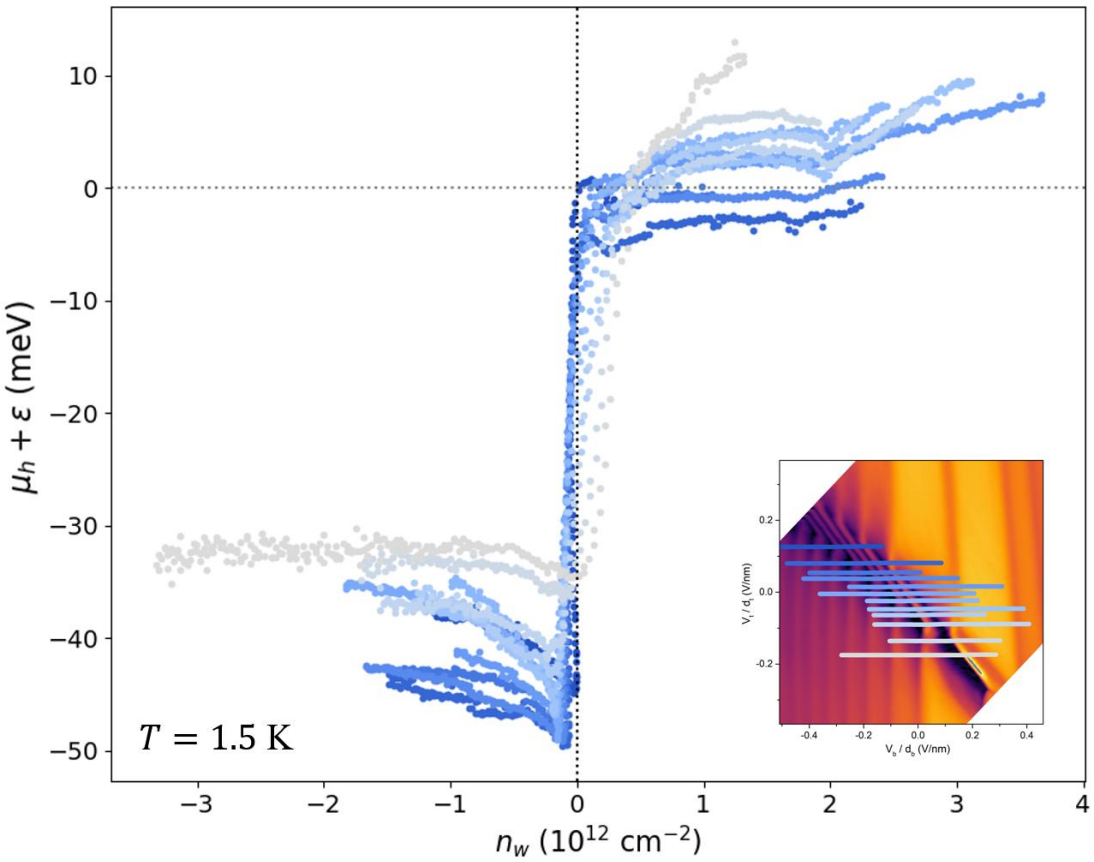

Figure 2.40: Hybrid chemical potential vs. inferred WTe_2 density n_w. n_w is computed from the contour interpolation map described in Section 2.3.4. The traces become vertical as we should expect with only slight discrepancies near the overall neutrality point (inset). This can be attributed to the decreased resolution of the contour interpolation near zero graphene doping as well as the increased numerical sensitivity near these points. Note that we cannot cleanly extract the WTe_2 density of states $D_w(\mu) = \frac{dn_w}{d\mu_w}$. In addition to the measurement artifacts on the conduction band side, ϵ, the energy offset between graphene and WTe_2, becomes relevant outside the gap. It does not seem possible to uniquely isolate μ_h as a result.

2.6 SUMMARY AND OUTLOOK

Unsurprisingly, the hybrid material graphene-WTe_2 can be principally understood as a combination of graphene and WTe_2. The two materials retain many of their individual properties including Landau quantization in the graphene and a correlated gap in WTe_2. We have seen, however, that the combination of graphene specifically with WTe_2 has many useful benefits. For instance, the use of graphene enabled the shaping of the hybrid into a suitable transport geometry. This includes both conventional reactive ion etching with edge contacts as well as a novel self-aligned oxidation technique. The use of graphene also allowed us to identify contours of constant graphene density by placing the hybrid in a strong magnetic field. This enabled us to extract the carrier densities of each material individually across our accessible gate range. Equipped with this information, we were able to calculate the interlayer charge separation in the hybrid, finding it to be 0.24 nm. We also estimated the WTe_2 density of states in the conduction band to be approximately 7.1×10^{11} cm^{-2} meV^{-1}, though there was considerable uncertainty in this value. Finally, we employed the use of a remote graphene sensor to measure the chemical potential of the hybrid relative to an electrostatic offset between the layers, $\mu_h + \epsilon$. This gave us a value of 1.01×10^6 m/s for the hybrid graphene Fermi velocity as we should expect. Despite some complications from strong negative compressibility, we determined the hybrid WTe_2 gap to be 36.0 ± 3.8 meV, consistent with the intrinsic gap. [31] It remains to be explained why the apparent dielectric constant in these hybrid devices is so low, why we do not see superconductivity, and why the low field magnetotransport is so peculiar when the graphene is neutral. It would be particularly exciting if the emergent feature seen in magnetotransport at the WTe_2 valence band edge is indeed a quantum spin Hall plateau. This may indicate that we have induced quantum spin Hall edges into the graphene which would certainly warrant extensive further study.

Chapter 3. Characterizing 2D Dielectrics

As we have seen, an external displacement field can shift the chemical potential of a 2D sample, making it a critical tuning knob for transport experiments. However, despite their use in transport devices, 2D dielectrics remain relatively understudied. In this chapter, I present my studies of 2D dielectric materials and offer some interpretations and best practices.

3.1 Hexagonal Boron Nitride

Following the successful mechanical exfoliation of graphene, one of the first major improvements to 2D devices was the use of hexagonal boron nitride. [71] While multiple crystal phases of boron nitride exist, we use "BN" to refer exclusively to hexagonal boron nitride, as it is the relevant polymorph for 2D physics. BN has a similar lattice constant to graphite with boron and nitrogen sublattices (some works even refer to it as "white graphene"). Unlike SiO_2, BN is crystalline, reducing disorder and improving mobilities of samples when used as a substrate. Electrically, BN is a robust insulator with a bandgap of roughly 6 eV. [72] Its ease of mechanical exfoliation and clean vdW interfaces with graphite and TMDs make it the default substrate and encapsulating material for 2D vdW devices as a result.

3.1.1 *Thickness Dependence and Dielectric Breakdown*

Let us consider a singly gated, grounded sample with gate voltage V and BN thickness d. We see the role of BN in determining the electron dopings and displacement fields we are able to achieve in the form of its relative dielectric constant, ε_{BN}.

$$n = \frac{\varepsilon_0 \varepsilon_{BN}}{e}\frac{V}{d} \Rightarrow n \propto \frac{\varepsilon_{BN}}{d} \qquad\qquad D = \varepsilon_{BN}\frac{V}{d} \Rightarrow D \propto \frac{\varepsilon_{BN}}{d}$$

Both the maximum doping and displacement field depend on the ratio $\frac{\varepsilon_{BN}}{d}$ for any given gate voltage. Given that $\varepsilon_{\mathrm{BN}}$ is a material property that is independent of thickness (at least for the thicknesses we are considering), it seems that thinner BN is better BN. However, the equations above ignore tunneling effects which become pronounced as d decreases. Consider the limiting case of monolayer BN ($d \approx 0.4$ nm). At this length scale, electrons can easily tunnel across, making it effectively electrically transparent. While this can be useful for encapsulating air-sensitive samples for measurements with STM or ARPES, it makes monolayer BN entirely unusable as a gate dielectric. In fact, BN thinner than ~3 nm is usually unsuitable for use in gates.

More importantly, no dielectric remains insulating to arbitrarily high fields. Eventually, if the electric field is strong enough, electric current can cross an insulator in a process called dielectric breakdown. [79] The microscopic mechanisms for how this occurs are varied and complex. [80][82][83] Even in the absence of defects, dielectric breakdown will occur when the electric field is strong enough. For example, the Zener effect describes a type of intrinsic breakdown where valence electrons get sufficient energy from a strong electric field to transition to the conduction band, resulting in a sudden onset of conductance. A similar type of breakdown called an avalanche cascade breakdown can occur when a strong electric field imbues electrons with sufficient energy to ionize atoms in the lattice during collisions. This same field then accelerates the ionized electrons into other atoms, resulting in a cascading current. [79] This is to say nothing of the effects of charged defects, vacancies, or other confounding factors in real samples. We will discuss the physical mechanisms of dielectric breakdown in detail in Section 3.1.2. For now, let us define $E_c = \frac{V_c}{d}$ as the critical electric field at which dielectric breakdown begins where V_c is the critical gate voltage and d is again the dielectric thickness. Unfortunately, there is not a singular relationship between E_c and d. [73] This fact combined with the uncontrolled

effect of defects and other processing steps (oxygen plasma etching, e-beam lithography, etc.) mean that direct empirical testing is the best way to determine E_c for BN in our devices. Anecdotally, a "good" BN gate has a breakdown field of $E_c \approx 0.5$ V/nm. Gates with breakdown fields of up to 1 V/nm do occur but are frustratingly uncommon.

3.1.2 *Measuring Breakdown Field*

Despite its ubiquitous use, there has been fairly limited research studying the breakdown field of BN. Recent studies of exfoliated BN using conductive atomic force microscopy (CAFM) have reported a breakdown fields ranging from $E_c = 1.2$ to 2.1 V/nm [74][75], however these results are not necessarily applicable to the 2D device use case. In CAFM measurements, a sharp conductive tip is brought near the sample, creating a very intense and highly localized (diameter ~100 nm) electric field gradient. While this provides a more intrinsic measurement of BN's material properties by sampling a small, homogeneous region, in a typical 2D device, the sample has an area of hundreds of square microns and any weak points in the BN form paths for breakdown. Moreover, existing CAFM measurements have been performed at room temperature, and the mobility of defects in such a strong field gradient has a large effect on breakdown character, as explored in Ref. [74]. The CAFM measurements are also destructive, damaging or even destroying the BN flake, making it difficult to gauge reproducibility and similarity to our use case. A more applicable study can be found in Ref. [76] in which the authors measure dielectric breakdown of various BN thicknesses both at room temperature and 10 K in similar geometries to those used in 2D devices. In DC measurements, they report increased breakdown field in thinner flakes of a given crystal source. However, the work is far from conclusive, and further study of different BN thicknesses, repeated measurements, and temperature dependence is warranted. Thusly motivated, I began making and testing BN breakdown devices. The structure of these

devices is incredibly simple: a BN flake is stacked on top of graphite to form a bottom gate geometry. Next, platinum contacts are evaporated by the same procedure used for transport devices. Some devices use transferred graphite contacts instead to eliminate any effects from metal evaporation or a work function mismatch between the graphite gate and contacts. BN flakes with regions of different thicknesses were deliberately chosen to demonstrate the effect of thickness on breakdown field within the same flake, adding more controls compared to previous studies.

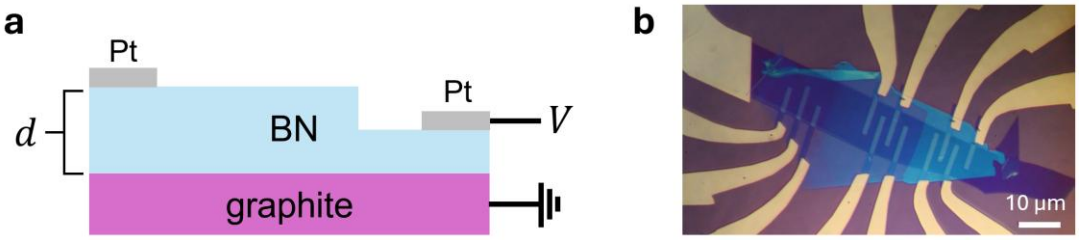

Figure 3.1: Device structure used for BN breakdown measurements. A DC voltage is applied to one contact at a time while the leakage current is measured. (a) Side view schematic of a device. Either platinum or graphite contacts are used. (b) Optical image of a BN breakdown device with graphite contacts (~2 μm across). Three regions of different thicknesses are measured.

By applying a voltage to a single contact with the graphite gate grounded, multiple data points can be obtained for a given BN thickness (one per contact). For each contact, the voltage was slowly increased until the onset of breakdown, always limiting the current to below 1 nA. Once the onset of breakdown was observed, the voltage was decreased back down to zero and the measurement was repeated. Both positive and negative voltages were measured. A typical charging loop is shown in Figure 3.2. The large current offsets are a result of capacitive charging of the measurement circuit, so $I \propto \frac{dV}{dt}$. The nonzero slope of the charging section represents the finite resistance of the BN and measurement circuit leakage, approximately 100 GΩ. The onset of breakdown can be seen as the current abruptly and rapidly increases.

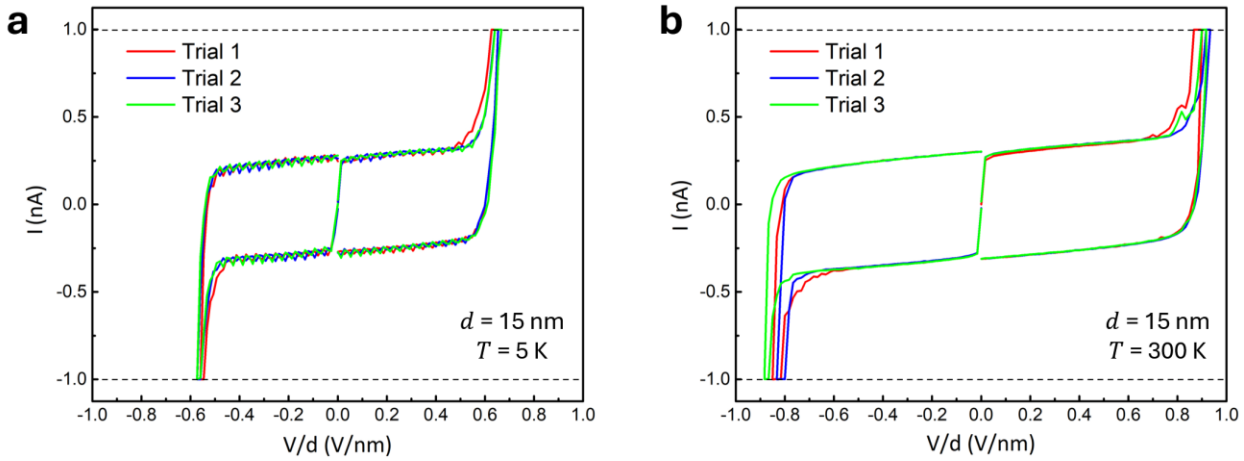

Figure 3.2: A typical charging loop for a 15 nm thick BN flake at (a) $T = 5$ K and (b) room temperature. The current is limited to 1 nA for both measurements. The fluctuations in the low temperature measurement are a result of mechanical noise from the cryostat's compressor.

These curves clearly demonstrate an inverted temperature dependence, with the room temperature breakdown field of 0.9 V/nm being substantially larger than the 0.65 V/nm breakdown field seen at 5 K. While trials are largely repeatable, there is also a slight "conditioning" effect where the breakdown field increases with repeated charging. This is a common occurrence in dielectrics that is not intrinsic to BN, [77] but it is a useful property for transport measurements. As we have seen in our studies of the graphene-WTe_2 hybrid, even small increases in gate range can be invaluable when probing physics far from charge neutrality. Additionally, there is a pronounced difference (10-15%) between the positive and negative breakdown fields. Devices with platinum and graphite contacts both showed similar imbalances, ruling out any effects of work function differences between contact and gate. However, these imbalances were not consistent between devices or even contacts on the same device, suggesting that local variations in the dielectric environment may be to blame. This is purely speculative though, and the exact cause of the asymmetry remains unknown. As seen in Figure 3.3, thinner BN showed higher breakdown fields than thicker BN, consistent with the findings of Ref. [76].

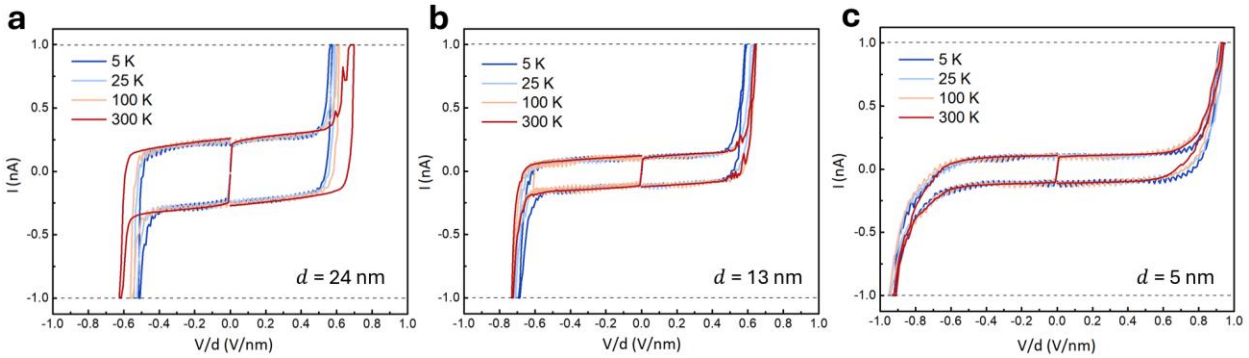

Figure 3.3: BN thickness dependence of breakdown field. (a), (b), and (c) represent three separate devices with BN thicknesses of 24, 13, and 5 nm respectively. The increased height of the charging loop in (a) reflects a faster voltage sweep rate.

Here we also see that the temperature dependence of the breakdown field becomes more pronounced with increasing thickness. Across the thinnest BN flakes measured (5-7 nm), there is relatively little temperature dependence. However, for thicker flakes, we see the breakdown field increase monotonically with temperature. Naïvely, this is the opposite behavior to what we should expect. Elevated temperatures serve to increase phonon scattering (lowering the threshold for impact ionization), decrease the effective bandgap, and increase the mobility and activation of defects, all of which should decrease the breakdown field. Nevertheless, this inverted temperature dependence is ubiquitous. In total, I have tested the breakdown of five separate BN devices, each with 5-10 functioning contacts, all of which show either weak temperature dependence or a marked increase in breakdown field with temperature. Temperature effects are more pronounced in thicker regions of BN. I have also tested the gates of other transport devices, each of which show the same trend. The effect survives thermal cycling as well; the breakdown field does not seem to be permanently altered by repeatedly cooling and warming. We will discuss potential causes of this seemingly inverted temperature dependence for BN breakdown in Section 3.1.3.

It is worth pausing to summarize the main takeaways from this work: (1) Thin BN supports higher breakdown fields than thicker BN. Thicknesses of 5-7 nm seem optimal for achieving the largest displacement fields. (2) BN breakdown shows an inverted temperature dependence, with the breakdown field increasing with temperature. (3) Thermal cycling has no appreciable effect on the dielectric properties of BN. (4) Thicker BN gates may be conditionable (repeatedly charging to "condition" the system to support higher fields) so long as fields are kept reasonably below breakdown. (5) High-current breakdown events may permanently decrease the breakdown field of BN. This is corroborated by Refs. [75] and [78]. (6) While higher temperatures support higher breakdown fields, the breakdown events tend to be more sudden and violent. It is not advisable to test gates at room temperature as a result. (7) There may be significant variance even among contacts on the same region of a single BN flake. This last point is particularly important and makes it difficult to make broadly prescriptive statements about best practices for the use of BN in transport devices. Consider, for example, the breakdown characteristics of the two adjacent contacts shown below in Figure 3.4. Both contacts show highly repeatable breakdown curves, but they have vastly different critical fields. The cause of this difference is currently unknown, and it is difficult to imagine either variations in fabrication process or local BN quality being to blame.

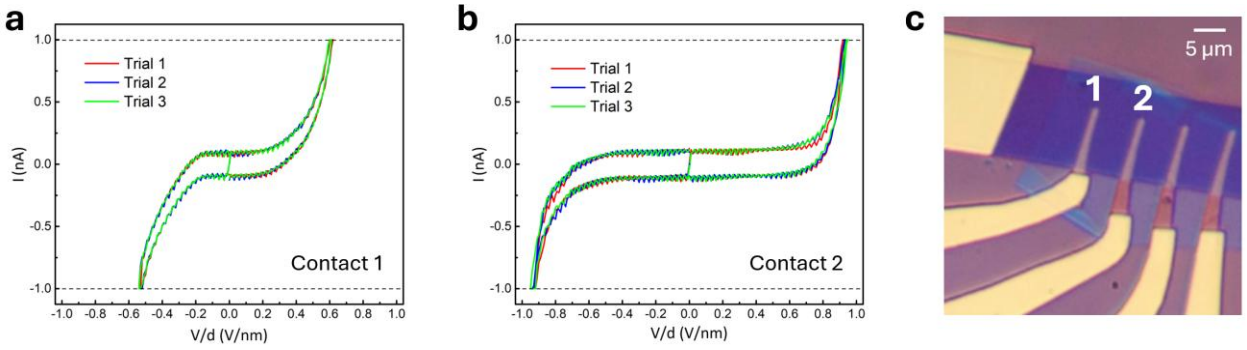

Figure 3.4: Breakdown characteristics of adjacent contacts (a) 1 and (b) 2 as labeled in (c). Both platinum contacts were formed via the same fabrication process at the same time and are contacting the same 5 nm thick region of a single BN flake. Data are shown for T = 5 K.

3.1.3 *Interpreting BN Breakdown*

Many of the findings we have presented are consistent with naïve expectations. For instance, the fact that BN can be permanently damaged by strong electric fields is in no way surprising. What is harder to reconcile is the apparently inverted temperature dependence of the breakdown field in BN. To properly consider this question, we must start with the basic microscopic mechanisms by which charges can cross an insulator. In an insulator, the Fermi energy lies between bands such that the valence band is full and the conduction band is empty, so the material is insulating. While thermal fluctuations or charged impurities can promote some electrons into the conduction band, their concentration is too small to detect at low electric fields. However, once the field passes a critical strength, the material suddenly becomes conductive—the dielectric breaks down. Dielectric breakdown is an important concern in high voltage electronics, but the physical mechanisms behind the process can be murky. Early theory posited two distinct classes of mechanism by which dielectric breakdown could occur. [80] The first is analogous to the breakdown of gases: a small population of conduction band electrons is raised to higher energies by the electric field, then when de-exciting, that energy is used to raise electrons from the valence band into the conduction band, and the process repeats. The second class of mechanism is more similar to autoionization, whereby an electric field is sufficiently strong to directly rip an electron free from an atom (valence band) to vacuum (conduction band). In solids, reasonably weak electric fields can still directly excite electrons from the valence to conduction band (as can be seen in any semiconducting device), suggesting this latter mechanism is the primary one.

Given the high crystallinity and purity of our BN, [81] it is difficult to imagine that there are any significant mechanical changes caused by temperature. Instead, we will focus on four canonical processes by which electrons can cross a metal-insulator-metal heterostructure: (1) direct

tunneling, (2) Fowler-Nordheim tunneling, (3) thermionic emission, and (4) Frenkel-Poole emission. [79] Direct tunneling is the most familiar and simplest. In this case, electrons are able to directly tunnel through a sufficiently thin, approximately rectangular energy barrier in a process that is independent of temperature. If the field is sufficiently large, the nearly rectangular energy barrier can distort into a triangle, enhancing tunneling current in a regime referred to as Fowler-Nordheim tunneling. [82]

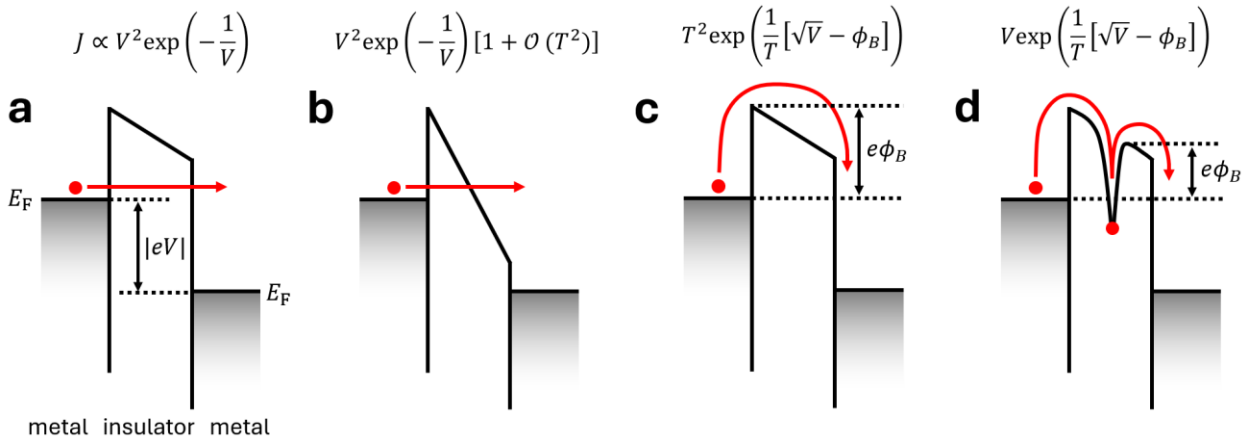

Figure 3.5: Band alignment diagrams (i.e. plots of electron energy vs. position) showing a metal-insulator-metal stack with a voltage V between metals. (a) Direct tunneling, (b) Fowler-Nordheim tunneling, (c) thermionic emission, and (d) Frenkel-Poole emission are shown. The dependence on voltage, temperature, and barrier height ϕ_B of the transmitted current density J are indicated, omitting all other constants for brevity and clarity.

Although Fowler-Nordheim tunneling describes a tunneling process, it exhibits weak temperature dependence as electrons gain thermal energy. Since the insulator's energy barrier is distorted, growing thinner with increased energy, thermal fluctuations can more readily increase tunneling current. This contrasts with direct tunneling where the energy barrier has a constant width. If an electron gains sufficient thermal energy to hop over the energy barrier entirely ($k_B T > \phi_B$), the process is referred to as thermionic emission. This process obviously has a strong

temperature dependence, becoming increasingly relevant at higher temperatures. The final process, Frenkel-Poole emission, considers the role of charge traps within the insulator. The model Frenkel presents in [83] is as follows: imagine a lattice of neutral atoms, then ionize one of them. This charge imbalance forms an electric potential well for any free electrons, trapping them. However, in the presence of an external electric field, the well is tilted (Figure 3.5d), effectively lowering the barrier height on one side of the well. Thus thermally excited electrons are able to successively hop from trap to trap across an insulator with a lower activation energy than thermionic emission.

Of the four processes described, the tunneling processes have no significant temperature dependence. Thermionic emission, both as its own mechanism and its effect in Fowler-Nordheim tunneling, serves to increase the conductivity of an insulator with increasing temperature. However, Frenkel-Poole emission has the opposite effect. Frenkel himself comments on this in his seminal 1938 paper: "It is interesting that on the above theory the effect of the field is *reduced* by the elevation of the temperature, just as is observed experimentally." [83] (Though he does not cite any relevant experimental results for this claim.) Indeed, we see that the current density scales as $J \propto e^{1/T}$, decreasing with increasing temperature. However, we are still far from definitively declaring any single reason for BN's inverted temperature dependence. Charge traps change their emission with temperature, defects change their mobilities, and different mechanisms dominate in different temperature and sample thickness ranges. All of these complications remain to be contended with to say nothing of the exceedingly high purity of our BN source. [81]

It is also difficult to find precedent in the literature for insulators with the same inverted temperature dependence for breakdown as BN. Ref. [84] reports the same apparent trend (higher breakdown field at higher temperatures) in crystalline strontium titanate ($SrTiO_3$), however the data show broad spreads and a substantially weaker temperature dependence than what is seen in

our BN measurements. Moreover, $SrTiO_3$ is a ferroelectric with a large dielectric constant that is sensitive to temperature, further muddying the comparison. In summary, the inverted temperature dependence of dielectric breakdown in BN makes it reasonable to assume that charge traps and Frenkel-Poole emission play a significant role. Further research is needed to be more prescriptive about the microscopic mechanisms that make BN so apparently unique in this regard.

Finally, let us consider the effect of thickness on BN breakdown. As seen in Figure 3.3 and Ref. [76], thinner BN supports higher breakdown fields than thicker BN. However, extremely thin BN becomes increasingly susceptible to direct tunneling, making it unsuitable for use in gates. To understand why thicker BN has lower breakdown fields, we must return our attention to avalanche breakdown. It stands to reason that thicker BN is more susceptible to avalanche events than thinner BN, as thinner flakes have less distance to accelerate electrons. 5-7 nm BN seems to be ideal in its performance as a gate dielectric as a result. It is sufficiently thick that tunneling is not a major issue while still being thin enough to be less susceptible to runaway conduction. This may also explain why this thickness of BN has weaker temperature dependence than thicker flakes.

3.2 Bismuth Selenium Oxide Bi_2SeO_5

BN has endured as the first and only exfoliative vdW dielectric used in 2D transport devices from the early days of graphene to present. However, recent publications from Peking University have demonstrated the synthesis of another crystalline vdW dielectric: Bi_2SeO_5. [85][86] Bi_2SeO_5 possesses many of the same characteristics that make BN useful, and it has potential to greatly increase the maximum doping achievable through electrostatic gating. Unfortunately, incorporating it into devices has proven challenging due to its poor vdW interfaces with many 2D materials. Further testing in 2D devices is also warranted before broader adoption.

3.2.1 *The Potential of Bi_2SeO_5*

In Section 3.1.1, we saw that the doping of a sample is proportional to the ratio $\frac{\varepsilon_r}{d}$ where ε_r is the relative permittivity of the gate dielectric and d is the dielectric thickness. Ref. [85] reports values of $\varepsilon_r \approx 4$ for BN and $\varepsilon_r \approx 12$ for Bi_2SeO_5 nanosheets. This would mean a threefold increase in doping assuming a similar breakdown field to BN! The utility of such a material hardly needs explanation; such a large increase in doping range would dramatically increase the accessible parameter space for transport measurements. For example, we saw in Figure 2.15 that the valence band edge of WTe_2 the graphene-WTe_2 hybrid is barely accessible with BN gates. A comparable Bi_2SeO_5 gate could easily reach this point and beyond, opening the door for transport studies of physics far from the Fermi energy.

On closer inspection, Bi_2SeO_5 seems like a promising material for use in 2D devices. While it can be synthesized from the precursor semiconductor Bi_2SeO_3 with the addition of oxygen, [85] centimeter scale crystals can be grown by chemical vapor transport (CVT). [86] CVT is a familiar growth method in the world of 2D materials that is much more accessible than the high-pressure growths of BN. [81] Bi_2SeO_5 has a large bandgap of approximately 3.9 eV. [85] While this is considerably smaller than the gap of BN, it does not necessarily follow that Bi_2SeO_5's performance in devices (i.e. breakdown field) will be proportionally lower than that of BN. Preliminary studies report that Bi_2SeO_5 is stable and chemically inert, also demonstrating enhanced mobility in the semiconductor Bi_2SeO when encapsulated with Bi_2SeO_5 compared to BN and SiO_2. [86] This is a promising result, as charge inhomogeneity is a major concern for dielectrics in 2D devices.

3.2.2 *Characterizing Bi_2SeO_5*

While BN is functionally the most similar 2D material to Bi_2SeO_5, the two behave very differently. For example, the exfoliation procedure is quite different. Following extensive experimentation, we settled on the following: copy a master tape with regular adhesive tape (like BN), transfer that tape to a PDMS gel, press the PDMS onto a SiO_2 substrate and heat at 80° C, let cool for fifteen minutes, then slowly peel the PDMS off. This is a more involved procedure than BN exfoliation, and the resulting Bi_2SeO_5 flakes are more sparse and thicker (≥20 nm thick) than a comparable BN exfoliation. Nevertheless, Bi_2SeO_5 flakes are sufficiently large and flat for use as substrates. They can be transferred with PC films like BN at a similar temperature range (90-100° C). While Bi_2SeO_5 can be used to pick up TMDs like WTe_2, it does not seem to form a vdW interface with BN or graphite. As shown in Figure 3.6, Bi_2SeO_5 flakes cannot be used for transfers of these materials, complicating device fabrication for gates.

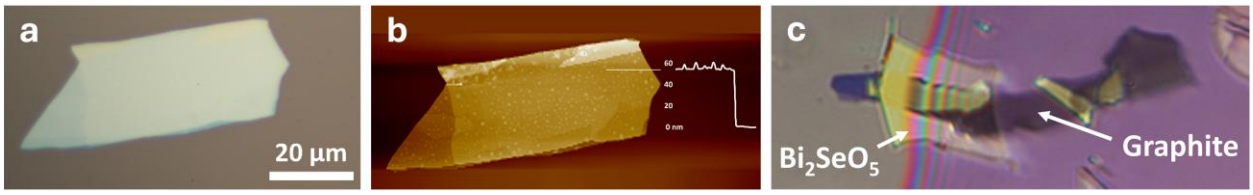

Figure 3.6: Bi_2SeO_5 exfoliation and device fabrication. (a) An optical image of a Bi_2SeO_5 flake. (b) An AFM height map of the same 55 nm flake. The bubbles are trapped under the flake and disappear after transferring. This is a common feature of Bi_2SeO_5 exfoliations. (c) An attempted transfer of graphite with Bi_2SeO_5. As indicated by the darker colored region of overlap, the flakes do not form a vdW interface, potentially due to their large lattice mismatch.

In order to test the dielectric performance of Bi_2SeO_5, I elected to build a simple device consisting of a doubly encapsulated graphene monolayer with Bi_2SeO_5 as one gate dielectric and BN as the other. This allowed for a direct comparison of their performances within the same device on a well understood system. Since Bi_2SeO_5 cannot pick up graphite or graphene, it had to be used

for the bottom gate dielectric. A Bi_2SeO_5 flake was directly deposited onto a graphite flake and platinum contacts were evaporated on top using e-beam lithography. I forwent the typical oxygen plasma surface roughening before evaporation out of caution for damaging the Bi_2SeO_5, an oxide.

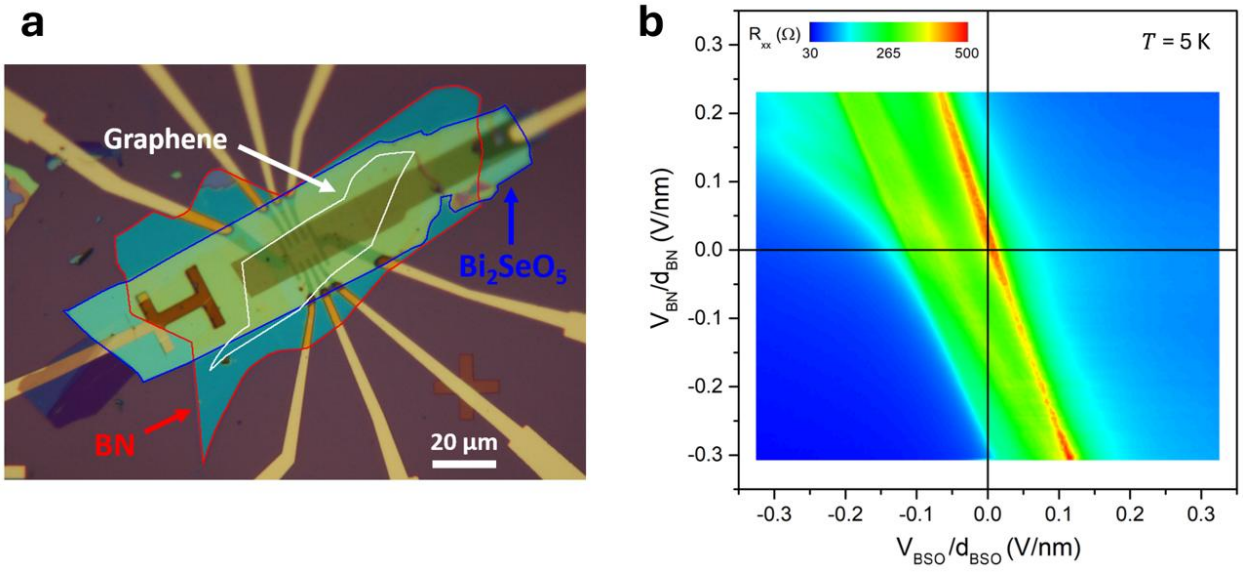

Figure 3.7: Bi_2SeO_5 as a gate dielectric. (a) Optical micrograph of the BN-graphene-Bi_2SeO_5 device. The Bi_2SeO_5 flake for the bottom gate is outlined in blue. The BN top gate (red) was used to pick up the monolayer graphene (white). (b) A 2D gate map showing R_{xx} for the graphene. Axes are normalized by dielectric thickness. A clear Dirac point is present with a slope of -3.0. The graphene is slightly p-doped by $n_0 = 3.7 \times 10^{11}$ cm^{-2}, seen in the rightward shift from the origin.

There is a well-defined and sharp Dirac point that linearly tracks both gates. However, there is also a broader resistive region with the same slope that suggests inhomogeneity in the sample. Other contact pairs in the device showed similar broadening, though it remains unclear from this device alone if this is a result of intrinsic charge inhomogeneity in our Bi_2SeO_5 or an effect specific to this particular device. We will therefore only focus on characterizing the Dirac point. Recall that the Dirac point is the only resistive feature in graphene's spectrum, $n_g = 0$, where $n_g = \frac{\varepsilon_0}{e}\left(\varepsilon_{BN}\frac{V_{BN}}{d_{BN}} + \varepsilon_{BSO}\frac{V_{BSO}}{d_{BSO}}\right)$. Therefore, along the Dirac point we have:

$$\frac{\varepsilon_{BSO}}{\varepsilon_{BN}} = -\frac{V_{BN}/d_{BN}}{V_{BSO}/d_{BSO}}$$

Or in other words, the negative slope of the Dirac point in transport gives the ratio of the two dielectrics' relative permittivities. The slope of the Dirac point is almost exactly -3, implying that $\varepsilon_{BSO} = 3\varepsilon_{BN}$. This is a substantial increase and consistent with the ratio reported in [85]. Importantly, the breakdown range of the Bi_2SeO_5 gate is consistent with that of the BN gate, allowing for a threefold increase in doping from the Bi_2SeO_5 gate over the BN gate.

To further probe the breakdown characteristics of Bi_2SeO_5, I also performed the same breakdown measurements described in Section 3.1.2 on this device (though now with all contacts shorted together by the graphene). These measurements were carried out from 5 K to room temperature on both the Bi_2SeO_5 and BN gates.

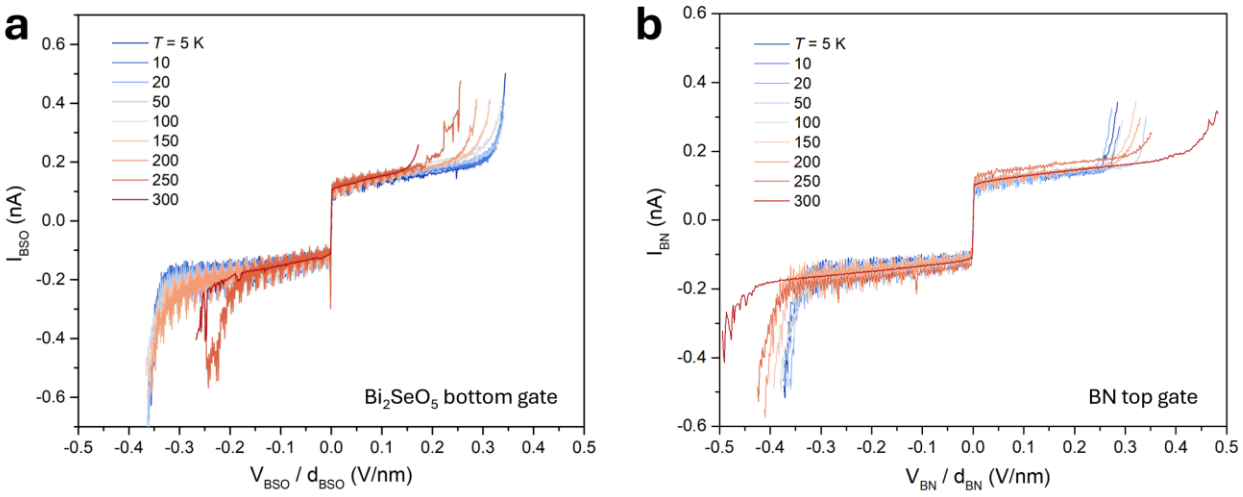

Figure 3.8: Breakdown curves for the (a) Bi_2SeO_5 bottom gate and (b) BN top gate from 5 K to room temperature. Both gates show similar breakdown fields at 5 K (~0.35 V/nm), but they have opposite temperature dependences. BN becomes more robust with temperature while Bi_2SeO_5 breaks down more readily at higher temperatures.

Interestingly, we see the exact opposite temperature dependences between the Bi_2SeO_5 and BN gates. The breakdown field of the Bi_2SeO_5 gate decreases monotonically with temperature,

while the opposite is true for the BN gate. The effect of temperature is quite pronounced for both materials. For example, on the positive side, the Bi_2SeO_5 gate's breakdown field gets roughly cut in half from 0.35 V/nm to 0.15 V/nm when warming from 5 K to room temperature while the BN gate's breakdown field nearly doubles from 0.25 V/nm to 0.45 V/nm. The temperature dependence of Bi_2SeO_5 is consistent with other dielectrics, making the behavior of BN all the stranger.

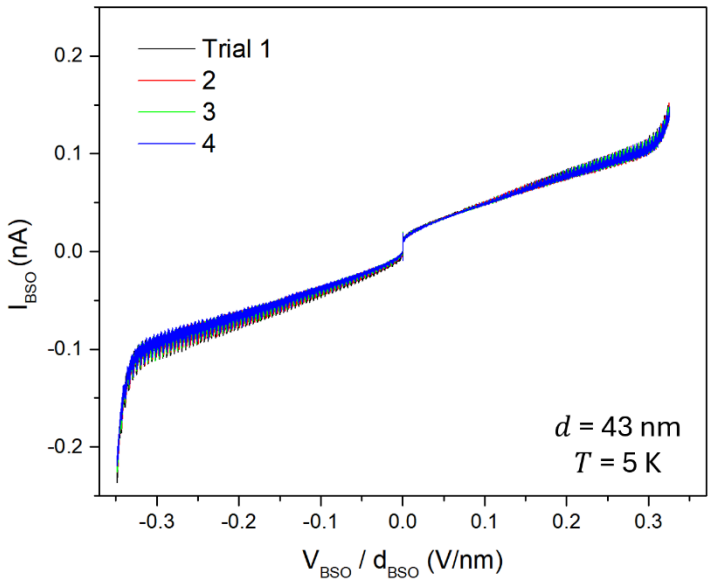

Figure 3.9: Demonstration of the repeatability of Bi_2SeO_5 breakdown at cryogenic temperature. Data are remarkably consistent, suggesting a high quality, robust insulator. The breakdown field of 0.35 V/nm is consistent with that of BN of a similar thickness at the same temperature.

The performance of the Bi_2SeO_5 gate was largely comparable to the BN gate. The magnitude of the breakdown field was similar between gates (Figure 3.8), the breakdown field was consistent between sweeps (Figure 3.9), and there were no effects from thermal cycling. Bi_2SeO_5 is therefore a promising material with the potential to dramatically expand the accessible doping range of 2D transport measurements. The main limitations of Bi_2SeO_5 appear to be lingering questions about charge inhomogeneity and poor vdW interfaces with graphite. The former point is more critical, and it will require further characterization and refinement in the future to assess.

Chapter 4. Two-Axis Rotator

We have seen that magnetic field is another powerful tuning knob in 2D transport measurements. In most cryostats, a single superconducting solenoid generates a magnetic field perpendicular to the sample plane. In this chapter, I present ongoing work in the development of a two-axis rotator for use in a dilution system, allowing for any orientation between the sample and magnetic field.

4.1 The Problem of Sample Rotation

2D systems are, by definition, highly anisotropic. As a result, they are often sensitive to the direction of magnetic field relative to the crystal plane. For example, in graphene, the out of plane magnetic field couples to both orbital and valley magnetic moments, resulting in Landau quantization and various valley effects, while the in plane magnetic field couples only to the electron spin. [87] Other systems like WTe_2 have responses aligned to axes that are neither in nor out of plane. The electrons in the quantum spin Hall edges in monolayer WTe_2 have a well-defined spin axis due to spin-momentum locking. That axis lies at an angle of $(40 \pm 2)^\circ$ to the normal, within the mirror plane. [88] Finding this angle requires complete control over the orientation of magnetic field, both the azimuthal angle (to find the WTe_2 mirror plane) and polar angle (to find the spin axis). Data reproduced from Ref. [88] show this process in Figure 4.1.

For brevity, let us define $B_\perp$ as the out of plane magnetic field and $B_\parallel$ as the in plane magnetic field. Most cryostats use a single superconducting solenoid that generates $B_\perp$ only, but by adding extra solenoids, $B_\parallel$ can be generated too. Such magnets are known as vector magnets and can generate magnetic fields along three axes independently, typically with a bias towards the $B_\perp$ field. For example, the University of Washington has a 9-1-1 T magnet housed inside a Bluefors LD-250 dilution refrigerator, meaning that $B_\perp = 9$ T and $B_\parallel \approx 1$ T.

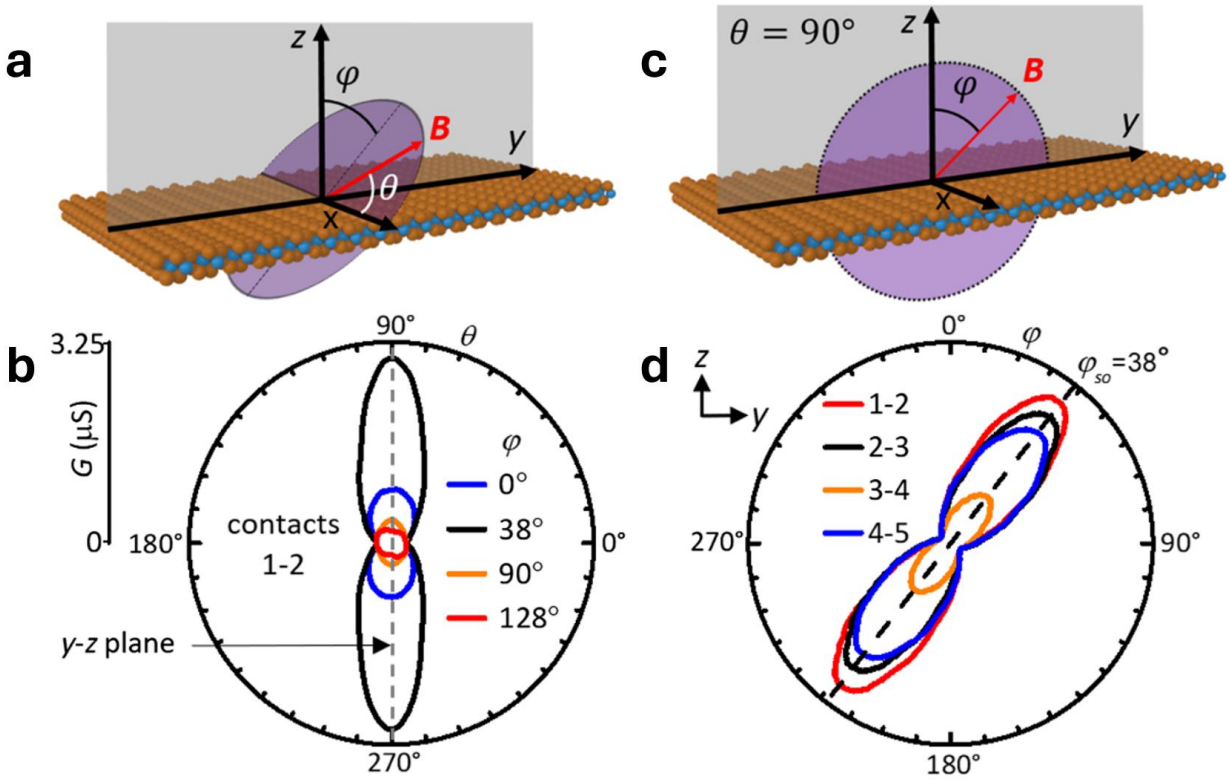

Figure 4.1: Reproduced section of Fig. 2 of [88] showing the determination of the spin axis in monolayer WTe_2. (a) Schematic of the WTe_2 monolayer. The mirror plane (y-z) is indicated in gray. (b) Polar plot of conductance G of a quantum spin Hall edge as a function of polar angle θ at various azimuthal angles φ. The magnetic field strength is 3 T and $T = 4$ K. (c) Schematic showing the plane traced out by varying φ within the mirror plane. (d) Polar plot of normalized conductance for various contact pairs. The most pronounced responses occur at $\varphi = 38°$.

While vector magnets are incredibly useful tools for characterizing 2D materials, the bias towards $B_\perp$ means that they are not ideal for all systems. For example, as we saw with graphene, electron spin couples to $B_\parallel$, but 1 T is too small of a field for substantial Zeeman splitting. In other measurements, a strong field at arbitrary angle may be a necessity rather than a perk. For instance, fermiology measurements utilize strong magnetic fields to create quantum oscillations that can be used to map a material's Fermi surface. [89] If a material has an anisotropic Fermi surface (e.g. $TaSb_2$ [90]), a strong, rotatable magnetic field is needed to map it.

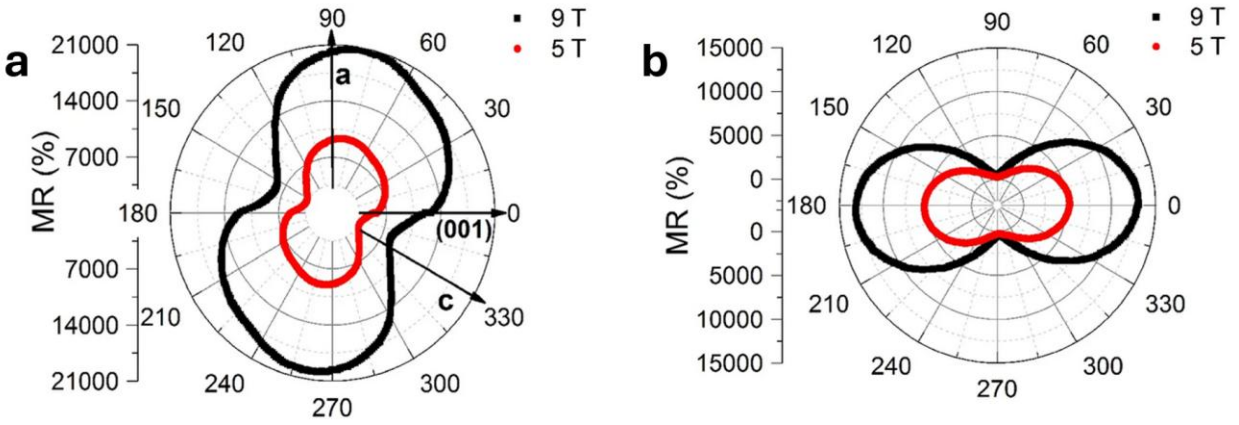

Figure 4.2: Reproduced section of Fig. 4 of [90] showing the magnetoresistance of $TaSb_2$. Data were taken at $T = 2$ K. (a) Magnetic field direction changes from (001) to the a-axis. The behavior is highly anisotropic and not mirror symmetric. (b) Magnetic field direction changes from $B_\perp$ to $B_\parallel$. The angle shown is the angle between the magnetic field and current.

4.2 Existing Designs

Rather than adjusting the direction of the magnetic field, the same effect can be achieved by rotating the sample within a static magnetic field. This immediately addresses the problem of weak in-plane fields from vector magnets, but it adds substantial complexity to the mechanical design of the sample mount. It must be able to accommodate the motion of the rotator while maintaining electrical and thermal connection to the sample. Additionally, since the sample will be rotating in a cryogenic environment, heat generated by friction becomes a major concern. This problem is exacerbated in dilution refrigerators since cooling power decreases rapidly with temperature, reaching only a few hundred microwatts at 100 mK. Rotating about two axes becomes even more complex. This section will discuss some existing sample rotation schemes and their individual strengths and weaknesses. The knowledge gained will then be used to inform the design and fabrication of our own two-axis rotator for use in a dilution system.

4.2.1 *Existing One-Axis Rotators*

Rotation about one axis is much simpler than two axes, and there are many commercially available one-axis rotators for use in various cryostats. The principle is straightforward: mount the sample to a component that is able to rotate freely. This component can be rotated in any number of ways. An early progenitor of modern one-axis rotator designs was developed in the late 1990s at the National High Magnetic Field Laboratory (MagLab). The design is simple, consisting of a cylindrical drum that is free to spin within a rigid yoke. The rotator is turned by pulling a string (Kevlar fishing line) wrapped around the drum. The string is pulled via a shaft connected to a micrometer head outside the cryostat, giving 0.02° precision with errors below 0.5%. [91]

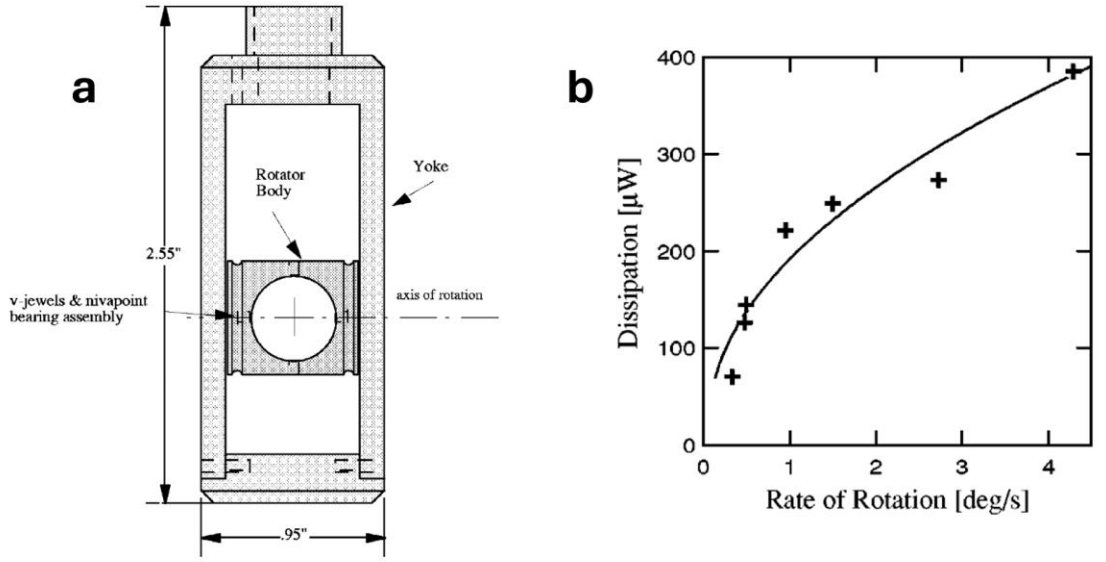

Figure 4.3: Reproduced Figs. 1 and 2 of [91]. (a) Technical drawing of the rotator. String is wrapped around the rotator body and threaded up through the holes indicated by dashed lines at the top of the yoke. (b) Heat dissipation for 20 s rotations.

This design has many strengths, chief of which is its low heating. By utilizing vee jewel bearings with matched Nivapoint pivots (a hard non-magnetic alloy [92]), the contact area between the rotator body and yoke is minimized. The use of jewel bearings is particularly noteworthy. Jewel bearings are made from sapphire and have historically been used in clock and watchmaking owing

to their high polish, low friction, and resistance to wear. [92] Sapphire is also entirely non-magnetic, a critical property for use in a strong magnetic field. From Figure 4.3, we see that the power dissipation of this rotator is approximately 220 μW when rotating at 1°/s. The maximum cooling power of the Bluefors LD-250 is 250 μW at 100 mK, so such a design should be able to rotate very quickly (180° range in three minutes) without substantially warming the sample space. The use of strings is also beneficial, as it allows the rotator's actuator to be placed far outside the sample space, saving space in the narrow bore (approximately 2.4 cm across for our system). The main drawback of the design lies in its control mechanism, as more modern systems would likely employ remotely controlled piezo actuators. While strings save space within the sample space, they also introduce uncertainty into the positioning of the rotator as they contract during cooling, necessitating the use of thermally rigid connecting rods to the top of the cryostat. [91]

This rotator design has proven successful, and many commercially available sample rotators follow in spirit. [93][94] These rotators typically employ gears instead of string, bypassing the problem of the drum rotating during cooling at the cost of mechanical backlash. Nevertheless, commercial rotators from Cryogenic Limited and ICEoxford report positional accuracies of 0.05° and 0.1° respectively. It is also possible to forego the mechanical complexity of remote drive and instead directly mount the sample to a rotating piezo motor. This technique allows for extremely accurate microdegree-scale positioning and is conceptually and mechanically simpler than any of the aforementioned designs. [95] However, it is also the least refined method, generating a large amount of heat and vibration in the sample space itself. Electrical noise is a concern as well, as piezo motors are driven by high voltages. This is certainly not ideal for transport measurements—it may be infeasible to measure transport while actively rotating the sample for instance. Moreover, space is at a premium in a cryostat, placing strict requirements on the piezo motor's dimensions.

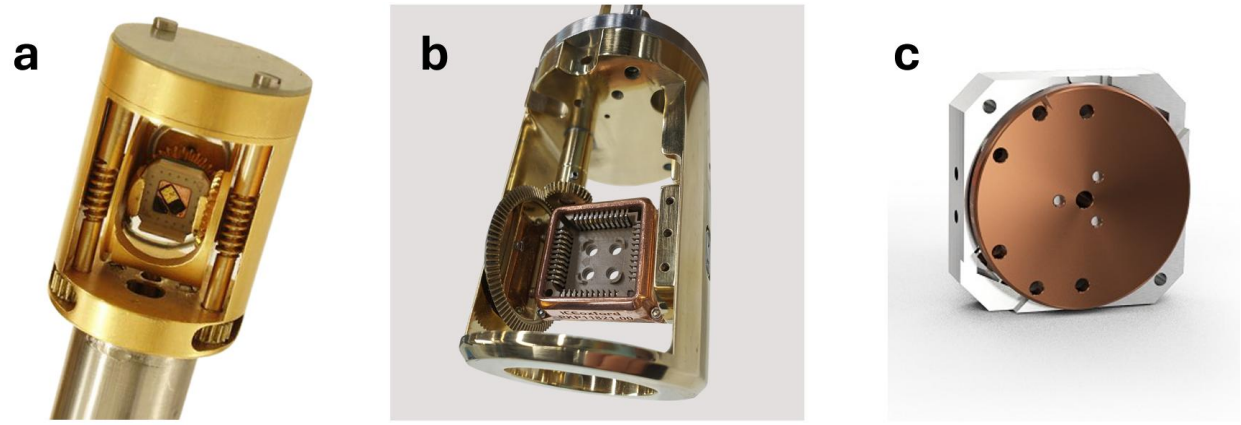

Figure 4.4: Images of commercially available one-axis sample rotators from (a) Cryogenic Limited, [93] (b) ICEoxford, [94] and (c) attocube systems (piezo motor only). [95] Mechanical systems employ gears to step down motion and achieve positional accuracy.

4.2.2 *Existing Two-Axis Rotators*

While one-axis rotators are fairly abundant, two-axis rotators are far less common, likely due to their more niche utility and increased complexity. Nevertheless, they do exist as commercial products and research systems. Some designs are shown below.

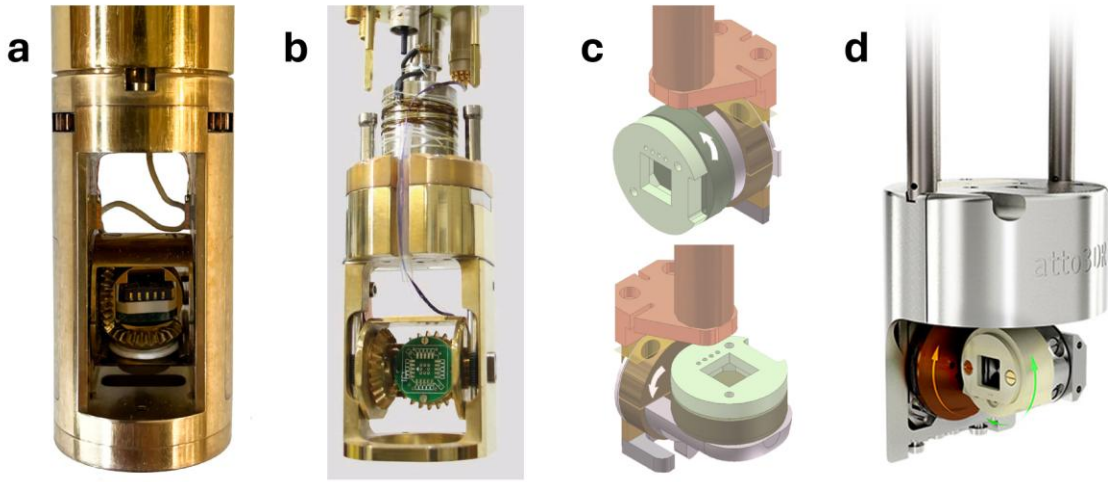

Figure 4.5: Various two-axis rotator designs. Mechanical designs from (a) Cryogenic Limited [93] and (b) ICEoxford [94] are not rated for use below 1 K. (c) Adjustable piezo scheme reproduced from Fig. 1 of [96]. (d) atto3DR, a dual piezo two-axis rotator from attocube systems designed to work at mK temperatures. [95]

The two mechanical designs shown in Figure 4.5 function similarly. Within the yoke, a set of counter-rotating gears turns the sample in plane. Both of these designs are targeted for use at a temperature of 1.5 K in variable temperature insert (VTI) cryostats, not dilution systems. The heat generated by these gear trains would likely prove problematic if used below 1 K. The remaining two schemes attach the sample to a rotating piezo motor. One axis is used to rotate the sample in plane and the other axis is used to rotate the sample out of plane. In the case of the atto3DR, both of these axes have piezo motors, so in-situ two-axis rotation is possible even at dilution refrigerator temperatures. [95] However, the system is reportedly unreliable, and the issues of piezo performance at millikelvin temperatures in the sample space cannot be avoided.

4.3 New On-Probe Two-Axis Rotator

Our rotator utilizes some of the same elements as existing designs but does so in a new way. Rather than gears or rotating piezo motors, our design uses linear piezo motors mounted on the probe far from the sample space. [91] These motors pull strings that rotate the individual axes on jewel bearings. The rotator was designed for use in a Bluefors-LD250 dilution refrigerator with a rapid sample exchange top-loading layout. [97] The cryostat's design allows it to maintain a cryogenic environment in the sample space while loading the probe. The probe is approximately 2 meters long with a maximum diameter of 5.8 cm. Most of the space within the probe body is empty, allowing us to mount linear-drive piezo motors near the top of the probe. We use Cryo Linear Drive piezo motors from JPE as they are cryogenically rated and have a small form factor, high lift force, and closed loop control. [98] The latter point is especially critical: the motors use a resistive strip for micron-scale position encoding. We have also written a custom software control loop that interfaces with the piezo controller and can be integrated into our existing measurement framework, allowing for seamless control of the sample orientation.

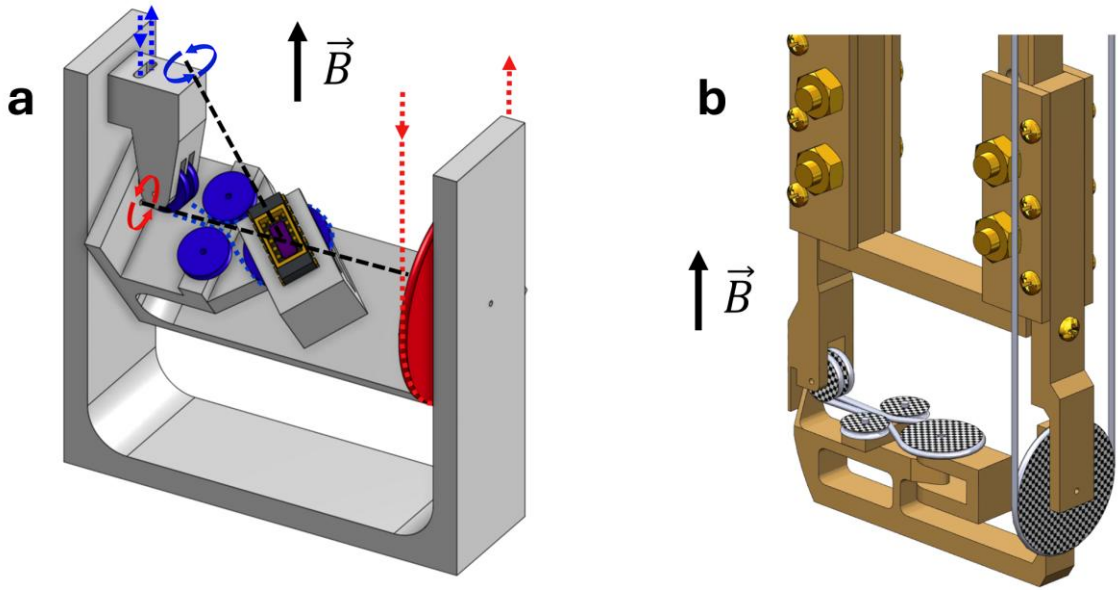

Figure 4.6: Two-axis rotator design. (a) A computer-aided design (CAD) rendering of an early prototype of the two-axis rotator. The primary rotation axis shown in red changes $B_{\perp}$ while the secondary axis shown in blue changes the direction of $B_{\parallel}$. (b) CAD rendering of a refined version of the rotator. The top of the image shows the cryostat cold fingers onto which the rotator attaches. The sample is then mounted on the center pulley and connected to measurement circuitry.

Motors mounted near the top of the probe pull strings that actuate small pulleys on the rotator itself. Rotating about the axis that is perpendicular to the axis of the probe serves to change the angle of the sample relative to the magnetic field, tuning $B_{\perp}$. We will denote this as the primary rotation axis. The design of the primary axis follows in the spirit of the MagLab one-axis rotator, [91] using vee jewel bearings retained in the outer yoke and sharp pivots on the rotation axis. The secondary axis rotates the sample perpendicular to the primary axis (aligned with the probe and magnetic field axes when the primary axis is at its starting position), changing the direction of $B_{\parallel}$. In order to be able to control both axes simultaneously, the strings for the secondary axis must run along the primary axis so that they do not get twisted. This is accomplished with a small pulley block that redirects the strings along the primary axis. Idler pulleys then wrap the string around a central pulley that the sample plate screws onto, rotating the sample in plane.

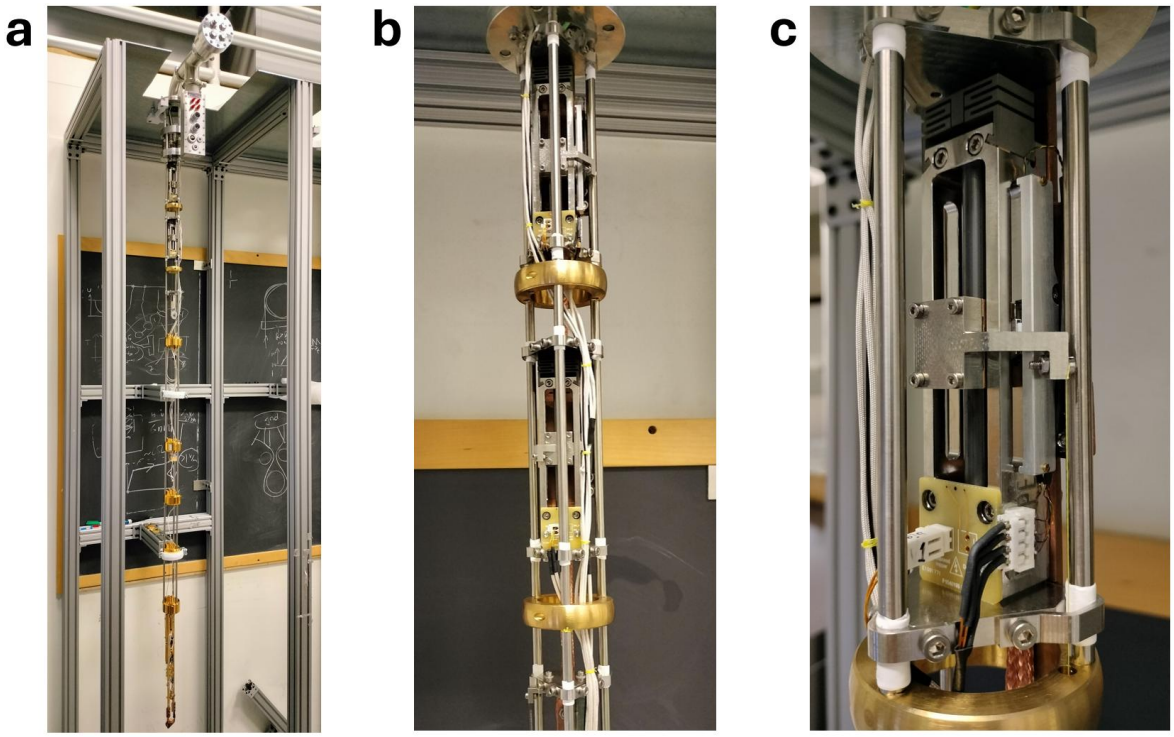

Figure 4.7: Rotator probe and piezo motors. (a) The LD-250 probe held in a custom mount. The rotator is visible at the bottom of the image. (b) Top of the probe showing the mounted piezo motors. Each motor controls one rotation axis. (c) Closeup image of the piezo motor that controls the secondary axis. The steel arm mounted to the motor holds a faintly visible yellow string (Kevlar fishing line) that extends through holes down the probe. The resistive linear sensor (RLS) module is visible on the right, allowing for closed loop positioning control of the arm.

Since the rotator will be operating in a high magnetic field, steel components are unsuitable. As such, the rotator body is machined from oxygen-free high thermal conductivity (OFHC) copper and uses sapphire jewel bearings with brass screws and pivots. Induced eddy currents in the rotator's copper body are a concern, but the sample itself is only weakly coupled to the rotator body. Instead, cooling will be delivered to the sample directly by attaching a flexible thermal strap to the sample plate itself. We have not yet quantitatively assessed the thermal performance of the rotator. While the internal thermometry of the cryostat can tell us the lattice temperature, we will also need to measure the electron temperature as these become decoupled

near absolute zero. We will do so by using the Coulomb blockade thermometry method, [99] though these measurements will have to be performed after finalizing the secondary axis.

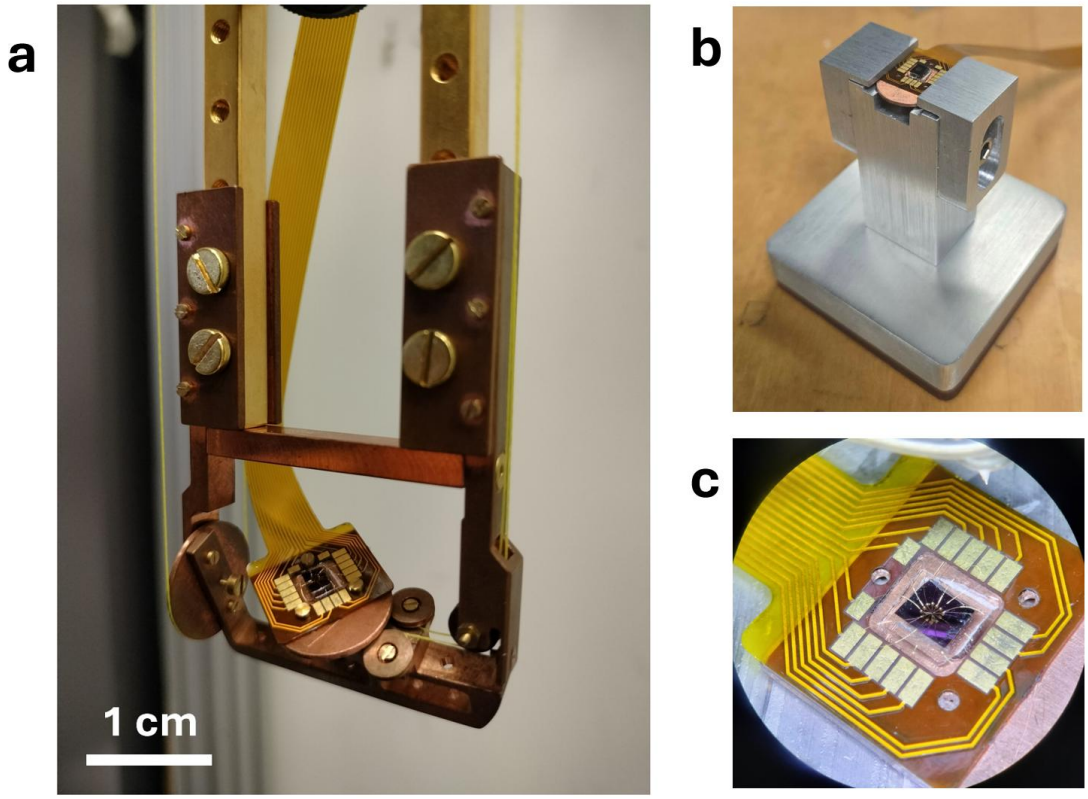

Figure 4.8: Two-axis rotator with a sample mounted. (a) Closeup image of the two-axis rotator. Rotation about the primary axis is achieved via the large pulley on the left of the image. Rotation about the secondary axis is achieved via a pulley under the sample plate. The string for the second axis is routed through the pulley block on the right side of the image to keep it aligned with the primary rotation axis and prevent twisting. Electrical connection to the sample is made via a flexible ribbon cable. (b) The sample plate and ribbon cable in a custom mount used for wirebonding. (c) Stereo microscope image of a bonded sample. The sample is glued to a sapphire spacer on the sample plate with silver epoxy. Bonded wires then connect it to the ribbon cable.

Preliminary testing of the rotator has largely taken place at room temperature and has mostly focused on positional accuracy and repeatability. These tests have shown reliable micron-scale positioning of the piezo motors which converts to $\sim 0.01°$ angular resolution. The performance of the motors should further improve at cryogenic temperatures, as their nominal

positional accuracy increases with decreasing temperature. [98] (The motors themselves are thermally anchored to the 50 K stage of the probe.) The strings that turn the pulleys have one fixed end attached to a metal arm on the piezo motor and another end tied off to a spring on a fixed platform. This keeps tension in the line at all times, preventing the strings from slipping against or off of the pulleys. This design has a major drawback however, as the string contracts while cooling, stretching the spring and turning the rotator. As such, we will need to quantify this contraction and account for it while cooling. This could be accomplished by slowly moving the motor down as the probe cools to keep the rotator body approximately steady. Since the sample itself is mounted on sapphire and the sample plate, a leveling procedure will still need to be undertaken for each device to find the exact alignment of the sample plane to the field. Future revisions may replace large sections of the string with dimensionally stable rods, as was done in Ref. [91].

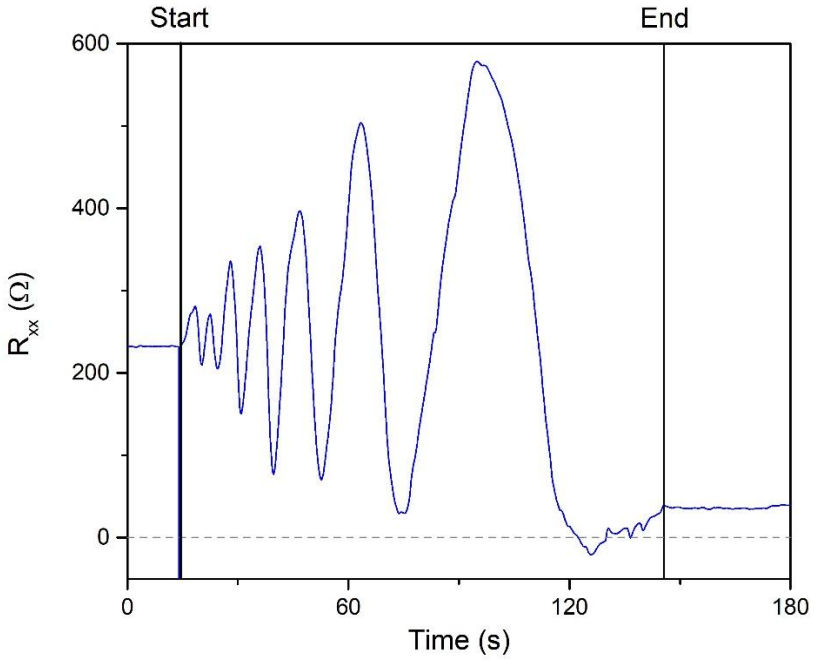

Figure 4.9: Transport data for a monolayer graphene device rotating about the primary axis in a 1 T magnetic field. Shubnikov-de Haas oscillations are visible as $B_{\perp}$ is tuned, consistent with the known behavior of monolayer graphene. [100] The piezo motor was driven at 10 Hz for 130 seconds, corresponding to 20 mm of linear motion (67° rotation).

A transport measurement of a monolayer graphene sample mounted on the rotator is shown in Figure 4.9. For this measurement, only the primary axis was rotated. The motor was driven at 10 Hz, covering 20 mm of travel (67° of rotation) in just 130 seconds. This gives a rotation speed of approximately 0.5°/s. While it is impossible to quantify the heating associated with this move, assuming similar friction to the MagLab design of [91], this would correspond to only ~130 μW of heating. It is also heartening to see clear Shubnikov-de Haas (SdH) oscillations with little in the way of noise. This suggests that having the piezo motors far from the sample space has effectively isolated them as a noise source for the measurement, an ideal outcome. SdH oscillations are quantum oscillations of R_{xx} vs. $B_{\perp}$ that arise from Landau quantization. [100] Conventionally, they are measured by varying the out of plane magnetic field strength, but the same effect can be achieved by changing the angle between the sample and a fixed magnetic field. These oscillations therefore serve as evidence of smooth, continuous rotation about the primary axis. Further refinements and characterizations are certainly in the near future for the two-axis rotator with a particular focus on the secondary axis. Based on early tests though, the design appears robust and promises unrivalled performance for in-situ sample rotation below 1 K.

BIBLIOGRAPHY

[1] Griffiths, D., Introduction to quantum mechanics. *Prentice Hall, Inc.* (1995).

[2] Bruch, L., Diehl, R., Venables, J. Progress in the measurement and modeling of physisorbed layers. *Rev. Mod. Phys.* **79**, 1381 (2007).

[3] Thomy, A., Duval, X., Regnier, J. Two-dimensional phase transitions as displayed by adsorption isotherms on graphite and other lamellar solids. *Surf. Sci. Rep.* **1** *1*, 1-38 (1981).

[4] Girvin, S. M., Yang, K. Modern condensed matter physics. *Cambridge Univ. Press* (2019).

[5] Kim, D., Yun, N., Jang, S. Y., *et al*. An inclusive structural analysis on the design of 1.2kV 4H-SiC planar MOSFETs. *IEEE J. Electron Devices Soc.* **9**, 804-812 (2021).

[6] Dingle, R., Störmer H. L., Gossard A. C., Wiegmann W. Electron mobilities in modulation-doped semiconductor heterojunction superlattices. *Appl. Phys. Lett.* **33**, 665-667 (1978).

[7] Wigner, E. On the interaction of electrons in metals. *Phys. Rev.* **46**, 1002-1011 (1934).

[8] Goldman, V. J., Santos, M., Shayegan, M., Cunningham, J. E. Evidence for two-dimensional quantum Wigner crystal. *Phys. Rev. Lett.* **65** *17*, 2189-2192 (1990).

[9] Landau, L., Diamagnetismus der metalle. *Z. Phys*. **64** 629-637 (1930).

[10] v. Klitzing, K., Dorda, G., Pepper, M. New method for high-accuracy determination of the fine-structure constant based on quantized Hall resistance. *Phys. Rev. Lett.* **45** *6*, 494-497 (1980).

[11] Tsui, D. C., Störmer H. L., Gossard A. C. Two-dimensional magnetotransport in the extreme quantum limit. *Phys. Rev. Lett.* **48** *22*, 1559-1562 (1982).

[12] Laughlin, R. B. Anomalous quantum Hall effect: an incompressible quantum fluid with fractionally charged excitations. *Phys. Rev. Lett.* **50** *18*, 1395-1398 (1983).

[13] Jain, J. K. Composite-fermion approach for the fractional quantum Hall effect. *Phys. Rev. Lett.* **63** *2*, 199-202 (1989).

[14] Novoselov, K.S., Jiang, D., *et al.* Two-dimensional atomic crystals. *Proc. Natl. Acad. Sci. U.S.A.* **102** (30) 10451-10453 (2005).

[15] Geim, A. K., Grigorieva, I., Van der Waals heterostructures. *Nature* **499**, 419-425 (2013).

[16] Novoselov, K. S., Geim, A. K., *et al.* Electric field effect in atomically thin carbon films. *Science* **306** *5696*, 666-669 (2004).

[17] Ajayan, P., Kim, P., Banerjee, K. Two-dimensional van der Waals materials. *Phys. Today* **69** *9* 38-44, (2016).

[18] Li, H., Li, S., *et al*. Imaging two-dimensional generalized Wigner crystals. *Nature* **597**, 650-654 (2021).

[19] Tsui, Y. C., He, M., *et al*. Direct observation of a magnetic-field-induced Wigner crystal. *Nature* **628**, 287-292 (2024).

[20] Li, H., Xiang, Z., *et al*. Wigner molecular crystals from multielectron moiré artificial atoms. *Science* **385** *6704*, 86-91 (2024).

[21] Feynman, R. There's plenty of room at the bottom. *[Speech at California Institute of Technology]* (1959).

[22] Wang, L. Meric, I., *et al*. One-dimensional electrical contact to a two-dimensional material. *Science* **342** *6158*, 614-617 (2013).

[23] Pizzocchero, F., Gammelgaard, L., *et al*. The hot pick-up technique for batch assembly of van der Waals heterostructures. *Nat. Commun.* **7** *11894* (2016).

[24] van der Pauw, L. J. A method of measuring the resistivity and Hall coefficient on lamellae of arbitrary shape. *Philips Tech. Rev.* **20**, 220-224 (1958).

[25] Schroder, D. K. Semiconductor material and device characterization (3rd ed.). *Wiley-IEEE Press*. (2015).
[26] McCann, E., Koshino, M. The electronic properties of bilayer graphene. *Rep. Prog. Phys.* **76** 056503 (2013).
[27] Zhang, Y., Tang, T., *et al*. Direct observation of a widely tunable bandgap in bilayer graphene. *Nature* **459**, 820-823 (2009).
[28] Wallace, P. R., The band theory of graphite. *Phys. Rev.* **71**, 622 (1947).
[29] Neto, A. H. C., Guinea, F., *et al*. The electronic properties of graphene. *Rev. Mod. Phys.* **81**, 109 (2009).
[30] Katsnelson, M. I., The physics of graphene. (2nd ed.). *Cambridge Univ. Press* (2020).
[31] Sun, B., Zhao, W., et al. Evidence for equilibrium exciton condensation in monolayer WTe2. Nat. Phys. 18, 94-99 (2022).
[32] Jia, Y., Wang, P., *et al*. Evidence for a monolayer excitonic insulator. *Nat. Phys.* **18**, 87-93 (2022).
[33] Sajadi, E., Palomaki, T., *et al*. Gate-induced superconductivity in a monolayer topological insulator. *Science* **362** *6417*, 922-925 (2018).
[34] Fatemi, V., Wu, S., *et al*. Electrically tunable low-density superconductivity in a monolayer topological insulator. *Science* **362** *6417*, 926-929 (2018).
[35] Song, T., Jia, Y., *et al*. Unconventional superconducting quantum criticality in monolayer WTe_2. *Nat. Phys.* **20**, 269-274 (2024).
[36] Song, T., Jia, Y., *et al.* Unconventional superconducting phase diagram of monolayer WTe_2. *Phys. Rev. Research* **7**, 013224 (2025).
[37] Delgado, L., Hu, C., *et al*. Record magnetoresistance, superconductivity, and fermiology in the topological semimetal WTe_2. (In preparation).
[38] Qian, X., Liu, J., Fu, L., Li, J. Quantum spin Hall effect in two-dimensional transition metal dichalcogenides. *Science* **346** *6215*, 1344-1347 (2014).
[39] Fei, Z., Palomaki, T., *et al*. Edge conduction in monolayer WTe_2. *Nat. Phys.* **13**, 677-682 (2017).
[40] Tang, S., Zhang, C., *et al*. Quantum spin Hall state in monolayer 1T'-WTe_2. *Nat. Phys.* **13**, 683-687 (2017).
[41] Shi, Y., Kahn, J., *et al*. Imaging quantum spin Hall edges in monolayer WTe_2. *Sci. Adv.* **5** *2* (2019).
[42] Ma, J., Deng, K., *et al*. Experimental progress on layered topological semimetals. *2D Mater.* **6** *3* (2019).
[43] Yin, L. J., Bai, K. K., *et al*. Landau quantization of Dirac fermions in graphene and its multilayers. *Front. Phys.* **12** *4*, 127208 (2017).
[44] Zhang, Y., Tan, Y. W., Stormer, H., Kim, P. Experimental observation of the quantum Hall effect and Berry's phase in graphene. *Nature* **438**, 201-204 (2005).
[45] Bolotin, K., Ghahari, F., *et al*. Observation of the fractional quantum Hall effect in graphene. *Nature* **462**, 196-199 (2009).
[46] Miseikis, V., Xiang, S., *et al*. Perfecting the growth and transfer of large single-crystal CVD graphene: a platform material for optoelectronic applications. In: Morandi, V., Ottaviano, L. (eds.) GraphITA: Carbon Nanostructures. *Springer* (2017).
[47] Soluyanov, A. A., Gresch, D., *et al*. Type-II Weyl semimetals. *Nature* **527**, 495-498 (2015).
[48] Wu, Y., Mou, D., *et al*. Observation of Fermi arcs in the type-II Weyl semimetal candidate WTe_2. *Phys. Rev. B* **94**, 12113(R) (2016).

[49] Wilson, J. A., Yoffe, A. D. The transition metal dichalcogenide discussion and interpretation of the observed optical, electrical and structural properties. *Adv. Phys.* **18**, 193-335 (1969).
[50] Keldysh, L. V., Kopaev, Y. V., Possible instability of the semimetallic state toward Coulomb interaction. *Fizika Tverdogo Tela* **6** *9* (1964).
[51] Que, Y., Chan, Y. H., *et al*. A gate-tunable ambipolar quantum phase transition in a topological excitonic insulator. *Adv. Mater.* **36** *7*, 2309356 (2023).
[52] Zhu, T. C., *et al*. Local spectroscopy of a gate-tunable energy gap in monolayer 1T′-WTe_2. (In preparation).
[53] Damascelli, A., Hussain, Z., Shen, Z. X. Angle-resolved photoemission studies of the cuprate superconductors. *Rev. Mod. Phys.* **75**, 473-541 (2003).
[54] Cucchi, I., Gutiérrez-Lezama, I., *et al*. Microfocus laser-angle-resolved photoemission on encapsulated mono-, bi-, and few-layer 1T'-WTe_2. *Nano Lett.* **19** *1*, 554-560 (2018).
[55] Nguyen, P., Micro-focus ARPES of operating 2D devices. (Ph.D. thesis, University of Washington, 2021).
[56] Binnig, G., Rohrer, H., Gerber, Ch., Weibel, E. Surface studies by scanning tunneling microscopy. *Phys. Rev. Lett.* **49**, 57-61 (1982).
[57] Hoffman, J. E., McElroy, K, *et al*. Imaging quasiparticle interference in $Bi_2Sr_2CaCu_2O_{8+\delta}$. *Science* **294** *5584*, 1148-1151 (2002).
[58] Wei, T., Hauke, F., Hirsch, A. Evolution of graphene patterning: from dimension regulation to molecular engineering. *Adv. Mater.* **33** *45* (2021).
[59] Wang, L., Meric, I., *et al*. One-dimensional electrical contact to a two-dimensional material. *Science* **342** *6158*, 614-617 (2013).
[60] Weng, L., Zhang, L., Chen, Y. P., Rokhinson, L. P. Atomic force microscope local oxidation nanolithography of graphene. *Appl. Phys. Lett.* **93**, 093107 (2008).
[61] Giesbers, A. J. M., Zeitler, U., *et al*. Nanolithography and manipulation of graphene using an atomic force microscope. *Solid State Commun.* **147** *9-10*, 366-369 (2008).
[62] Kim, B., Sternbach, A., *et al*. Ambipolar charge-transfer graphene plasmonic cavities. *Nat. Mater.* **22**, 838-843 (2023).
[63] Kim, B., Ngo, T. D., *et al*. Advances and applications of oxidized van der Waals transition metal dichalcogenides. *Adv. Sci.* **11** *43*, 2407175 (2024).
[64] Domaretskiy, D., Wu, Z., *et al*. Proximity screening greatly enhances electronic quality of graphene. *Nature* **644**, 646-651 (2025).
[65] Ataei, S. S., Varsano, D., Molinari, E., Rontani, M., Evidence of ideal excitonic insulator in bulk MoS_2 under pressure. *Proc. Natl. Acad. Sci.* **118** e2010110118 (2021).
[66] Laturia, A., Van de Put, M. L., Vandenberghe, W. G., Dielectric properties of hexagonal boron nitride and transition metal dichalcogenides: from monolayer to bulk. *NPJ 2D Mat. and App.* **2** *6* (2018).a
[67] Kim, S., Jo, I., *et al*. Direct measurement of the Fermi energy in graphene using a double-layer heterostructure. *Phys. Rev. Lett.* **108**, 116404 (2012).
[68] Yang, F., Zibrov, A. A., *et al*. Experimental determination of the energy per particle in partially filled Landau levels. *Phys. Rev. Lett.* **126**, 156802 (2021).
[69] Eisenstein, J. P., Pfeiffer, L. N., West, K. W. Negative compressibility of interacting two-dimensional electron and quasiparticle gases. *Phys. Rev. Lett.* **68** *5* (1992).
[70] Riley, J. M., Meevasana, *et al*. Negative electronic compressibility and tunable spin splitting in WSe_2. *Nat. Nanotechnol.* **10**, 1043-1047 (2015).

[71] Dean, C., Young, A. *et al*. Boron nitride substrates for high-quality graphene electronics. *Nat. Nanotechnol.* **5**, 722-726 (2010).
[72] Cassabois, G., Valvin, P. & Gil, B. Hexagonal boron nitride is an indirect bandgap semiconductor. *Nature Photonics* **10**, 262-266 (2016).
[73] Zhao, L., Liang Liu, C. Review and mechanism of the thickness effect of solid dielectrics. *Nanomaterials* **10** *12*, 2473-2495 (2020).
[74] Hattori, Y., Taniguchi, T., Watanabe, K., Nagashio, K. Layer-by-layer dielectric breakdown of hexagonal boron nitride. *ACS Nano* **9** *1*, 91-921 (2014).
[75] Ranjan, A., Raghavan, N., Holwill M., *et al*. Dielectric breakdown in single-crystal hexagonal boron nitride. *ACS Appl. Electron. Mater.* **3** *8*, 3547-3554 (2021).
[76] Pierret, A., Mele, D., Graef, H. *et al*. Dielectric permittivity, conductivity, and breakdown field of hexagonal boron nitride. *Mater. Res. Express* **9** 065901 (2022).
[77] Martinez-Vega, J. (ed.) Dielectric materials for electrical engineering. *Wiley/ISTE* (2010).
[78] Hattori, Y., Taniguchi, T., Watanabe, K., Nagashio, K. Anisotropic dielectric breakdown strength of single crystal hexagonal boron nitride. *ACS Appl. Mater. Interfaces* **8** *41* (2016).
[79] Sze, S., Ng, K. Physics of semiconductor devices (3rd ed.). *Wiley* (2007).
[80] Zener, C. A theory of the electrical breakdown of solid dielectrics. *Proc. R. Soc. A* **145** *855*, 523-529 (1934).
[81] Taniguchi, T., Watanabe, K. Synthesis of high-purity boron nitride single crystals under high pressure by using Ba-BN solvent. *J. Cryst. Growth*. **303** *2*, 525-529 (2007).
[82] Fowler, R. H., F. R. S., Nordheim, L. Electron emission in intense electric fields. *Proc. R. Soc. A.* **119** *781*, 173-181 (1928).
[83] Frenkel, J. On pre-breakdown phenomena in insulators and electronic semi-conductors. *Phys. Rev.* **54**, 647-648 (1938).
[84] Barrett, H. Dielectric breakdown of single-crystal strontium titanate. *J. Appl. Phys.* **35** *5*, 1420-1425 (1964).
[85] Li, T., Tu, T., Sun, Y. *et al*. A native oxide high-κ gate dielectric for two-dimensional electronics. *Nat. Electron.* **3**, 473–478 (2020).
[86] Zhang, C., Tu, T., Wang, J. *et al*. Single-crystalline van der Waals layered dielectric with high dielectric constant. *Nat. Mater.* **22**, 832–837 (2023).
[87] Xiao, D., Yao, W., Niu, Q. Valley-contrasting physics in graphene: magnetic moment and topological transport. *Phys. Rev. Lett.* **99**, 236809 (2007).
[88] Zhao, W., Runburg, E., Fei, Z. *et al*. Determination of the spin axis in quantum spin Hall insulator candidate monolayer WTe_2. *Phys. Rev. X* **11**, 041034 (2021).
[89] Uji, S. Fermiology: quantum oscillations and angle dependent magnetoresistance oscillations. *Springer* (2025).
[90] Pariari, A., Singha, R., Roy, S. *et al*. Anisotropic transverse magnetoresistance and Fermi surface in $TaSb_2$. *Sci. Rep.* **8**, 10527 (2018).
[91] Palm, E. C., Murphy, T. P., Very low friction rotator for use at low temperatures and high magnetic fields. *Rev. Sci. Instrum.* **70**, 237-239 (1999).
[92] Swiss Jewel Company, Jewel bearing applications. *Swiss Jewel Company*. (Accessed Feb. 2026). https://www.swissjewel.com/applications/jewel-bearing-applications/
[93] Cryogenic Limited, Rotating sample probes. *Cryogenic Limited*. (Accessed Feb. 2026). https://www.cryogenic.co.uk/products/rotating-sample-probes https://www.cryogenic.co.uk/sites/default/files/product_files/new_rotating_probe_brochure_v6.pdf
[94] ICEoxford, Rotating chip carrier. *Oxford Instruments*. (Accessed Feb. 2026). https://www.iceoxford.com/Rotating-Chip-Carrier.htm

https://www.iceoxford.com/Dual-Axis-Rotator.htm
[95] Attocube, Nanopositioners. *Wittenstein Group*. (Accessed Feb. 2026). https://www.attocube.com/en/products/nanopositioners/low-temperature-nanopositioners https://www.attocube.com/en/products/measurement-tools/atto3dr
[96] Yeoh, L. A., Srinivasan A., Martin T. P., *et al*. Piezoelectric rotator for studying quantum effects in semiconductor nanostructures at high magnetic fields and low temperatures. *Rev. Sci. Instrum.* **81** *11*, 113905 (2010).
[97] Bluefors, LD dilution refrigerator measurement system. *Bluefors*. (Accessed Feb. 2026). https://bluefors.com/products/dilution-refrigerator-measurement-systems/ld-dilution-refrigerator-measurement-system/
[98] JPE, Cryo linear drive. *JPE*. (Accessed Feb. 2026). https://www.jpe-innovations.com/cryo-uhv-products/cryo-linear-drive/
[99] Pekola, J. P., Hirvi, K. P., Kauppinen, J. P., Paalanen, M. A. Thermometry by arrays of tunnel junctions. *Phys. Rev. Lett.* **73**, 2903 (1994).
[100] Novoselov, K. S., Geim, A. K., *et al*. Two-dimensional gas of massless Dirac fermions in graphene. *Nature* **438**, 197-200 (2005).

VITA

Eric was born and raised in Raleigh, North Carolina. He took an interest in physics while attending Raleigh Charter High School before matriculating to Carnegie Mellon University. He graduated in 2020 with a Bachelor of Science degree with a major in physics and minor in computer science. In Fall 2020, he moved to Seattle and began his physics Ph.D. program at the University of Washington. He would join Prof. David Cobden's Nanodevice Physics group where he would remain for his six year graduate school tenure. He leaves the University of Washington to become a cryogenics engineer at Bluefors, where he hopes to develop a career in scientific instrumentation.